

Belly Landing of the LocalHawk UAV

Low-Velocity Impact Simulation Using an Explicit Finite Element Solver

Master's thesis in Product Development

HANS MAGNUS THORSEN

Department of Product and Production Development

Division of Product Development

CHALMERS UNIVERSITY OF TECHNOLOGY

Gothenburg, Sweden 2013

Master's thesis

MASTER'S THESIS IN PRODUCT DEVELOPMENT

Belly Landing of the LocalHawk UAV

Low-Velocity Impact Simulation Using an Explicit Finite Element Solver

HANS MAGNUS THORSEN

Department of Product and Production Development

Division of Product Development

CHALMERS UNIVERSITY OF TECHNOLOGY

Gothenburg, Sweden 2013

Belly Landing of the LocalHawk UAV
Low-Velocity Impact Simulation Using an Explicit Finite Element Solver
HANS MAGNUS THORSEN

© HANS MAGNUS THORSEN, 2013

Department of Product and Production Development
Division of Product Development
Chalmers University of Technology
SE-412 96 Gothenburg
Sweden
Telephone: +46 (0)31-772 1000

Cover:

Gradual failure for ply #9 in a [90, 0, 90, 0, 90, 0, 90, 0, 90] stacking sequence with a descend velocity of 2.5 [m/s] and pitch angle of $\theta = 0$ deg

Chalmers Reproservice
Gothenburg, Sweden 2013

Belly Landing of the LocalHawk UAV
Low-Velocity Impact Simulation Using an Explicit Finite Element Solver
Master's thesis in Product Development
HANS MAGNUS THORSEN
Department of Product and Production Development
Division of Product Development
Chalmers University of Technology

ABSTRACT

During the summer of 2012, a total of three UAV airframe concepts were developed in the LocalHawk summer student project at Kongsberg Defence Systems (KDS) in Kongsberg, Norway. All of the airframe concepts had belly landing as the preferred conceptual solution for landing the UAV. Out of those three concepts, the third was selected for further development, however, before the students of 2013 could start working on it, the feasibility of belly landing as a conceptual solution for that particular concept would have to be investigated.

Four concepts for the skin and internal stiffening structure of the fuselage was developed using product development methodology. Out of those four, two were selected for detailed scrutiny. The Multiframe concept had in total nine inner frames, consisting of rigid foam, that supported the payload and batteries, and a composite skin built up by nine plies of an unbalanced woven fiberglass prepreg. Relying on a sandwich structure, five plies of the aforementioned composite material on each side of an 8 [mm] thick foam core, the Sandwich Skin concept's structure had two larger frames supporting the payload and the batteries.

An explicit Finite Element (FE) solver, Ansys AUTODYN, was applied to simulate the low-velocity impact between the 12.5 [kg] UAV's fuselage and a rigid, smooth surface representing the ground. Several different stacking sequences were tested at a descend velocity of 2.5 [m/s] and pitch angle of 0 deg. From the stacking sequence tests, a preferred stacking sequence was selected based on its maximum stress and resistance to failure. Using this selected stacking sequence, both skin and internal stiffening structure concepts were tested at descend velocities of 1 [m/s] and 2.5 [m/s], with the pitch angle, θ , either set to 0 deg or 6 deg.

For the third UAV airframe concept, all tested cases end in severe failure in every ply. Generally, the narrow bulge on the belly of the fuselage is forced inwards towards the payload, resulting in failure initiation on the inner skin surface. From this area, the material failure propagates through plies along the center-line of the belly. As the bulge continues to be forced inwards, tensional stresses on the outside of the skin, on either side of the now more-or-less flattened bulge, result in material failure. At $\theta = 6$ deg, the bulge does not come into contact with the ground in the short duration of the analysis, however, the total weight and the narrow rear body of the UAV, i.e. little surface area in contact with the ground which results in an increased contact force, is enough to ensure material failure.

These results dictate either a redesign of the UAV to include a landing gear, or a fresh start, designing a new UAV. An optional possibility is to scale down the UAV, and increase surface landing area, so that the UAV can utilize the advantages of the simplistic solution of landing on its belly. Regardless of the chosen path, a UAV weighing in total 12.5 [kg], with such a small surface area in contact with the ground during landing, is deemed unfit for belly landing.

Keywords: Explicit, FEM, UAV, Belly Landing, Composite, Low-Velocity Impact

PREFACE

This 30 ECTS thesis was submitted to the Department of Production and Product Development in partial fulfillment of the requirements for the degree of Master of Science (M.Sc.) in Mechanical Engineering, with a specialization in Product Development, at Chalmers University of Technology.

ACKNOWLEDGEMENTS

First of all I would like to state my sincere appreciation to my external supervisor at KDS, Heming Melvold Andersen, for his guidance, patience, and support, which without, I would not have been able to complete my thesis. Also deserving gratitude at KDS, is Per Olav Kristiansen for his helpful guidance throughout the project, as well as specific advice in uncertain matters.

I would also like to thank EDR&Medeso for providing me with free training in Ansys Explicit STR, specifically Mikael Lauth for his very open, pedagogical, and straight-forward approach to teaching the course. He has also provided me with valuable, free, support after the completion of the course, even taking the time to go through my model to offer advice on improvement, for which I am extremely grateful. Gurit deserves recognition for them providing me with composite material data and specific advice for my case.

And of course, I would like to thank my internal supervisor at Chalmers, associate professor Dr. Lars Lindkvist, for his efficient and valuable help in both the planning and writing of the thesis, as well as administrative and software issues. Lastly, Assistant Professor Dr. Martin Fagerström at Chalmers also deserves appreciation for his help in providing me with software for composite pre-processing and guidance in the application of this.

NOMENCLATURE AND ABBREVIATIONS

t	Time	$[s]$
Δt	Time step	$[s]$
n	Vertical loading factor	$[-]$
V_{eq}	Equivalent airspeed	$[m/s]$
V	Velocity	$[m/s]$
a	Acceleration	$[m/s^2]$
s	Distance or stretch	$[m]$
g	Gravitational constant acceleration	$[m/s^2]$
ε	Failure strain	$[m/m]$
C	Speed of sound	$[m/s]$
P	Contact force	$[N]$
k	Contact stiffness	$[Nm^{-3/2}]$
α	Indentation	$[m]$
R	Radius of curvature	$[m]$
E	Young's modulus	$[N/m^2]$
ν	Poisson's ratio	$[-]$
T_0	Stagnation temperature	$[K]$
T	Ambient temperature	$[K]$
M	Mach number	$[-]$
\mathbf{K}	Global stiffness matrix	$[N/m]$
\mathbf{u}	Global nodal displacement vector	$[m]$
\mathbf{f}	Nodal force vector	$[N]$
\mathbf{M}	Mass matrix	$[kg]$
$\ddot{\mathbf{u}}$	Nodal acceleration vector	$[m/s^2]$
\mathbf{C}	Matrix of damping coefficients	$[kg/s]$
$\dot{\mathbf{u}}$	Nodal velocity vector	$[m/s]$
$\tau_{\Delta t}$	Duration of time step	$[s]$
θ_w	Weighting parameter	$[-]$
ω_{max}	Maximum eigenvalue of an element	$[Hz]$
L_e	Characteristic element dimension	$[m]$
c_d	Dilatational wave speed	$[m/s]$
ε	Strain vector	$[m/m]$
\mathbf{S}	Compliance matrix of a laminate	$[m^2/N]$
σ	Stress	$[N/m^2]$
G	Shear modulus	$[N/m^2]$
\mathbf{C}	Material stiffness matrix	$[N/m^2]$
τ	Shear stress	$[N/m^2]$
θ	Pitch angle	$[deg]$
f	Time step safety factor	$[-]$
h	Characteristic length of element	$[m]$
ρ	Density	$[kg/m^3]$
m	Mass	$[kg]$

FEM	Finite Element Method
FEA	Finite Element Analysis
FE	Finite Element
UAV	Unmanned Aerial Vehicle
UAS	Unmanned Aircraft System
RPAS	Remotely Piloted Aircraft System
RPV	Remotely Piloted Vehicle
DDD	Dull Dirty Dangerous
SI	Spark Ignition
CFD	Computational Fluid Dynamics
GPU	Graphics Processing Unit
GFRP	Glass-Fiber-Reinforced Polymers
CFRP	Carbon-Fiber-Reinforced Polymers
1D, 2D, 3D	One, Two, Three-Dimensional
CPU	Central Processing Unit
CG	Center of Gravity
CAD	Computer Aided Design
CAE	Computer Aided Engineering
CAM	Computer Aided Manufacturing
KDS	Kongsberg Defence Systems
FPF	First-Ply Failure
LPF	Last-Ply Failure
HVI	High Velocity Impact
LVI	Low Velocity Impact
STEP	STandard for the Exchange of Product model data
BC	Boundary Condition
PC	Patch Conforming
PI	Patch Independent
CFL	Courant-Friedrichs-Lewy

CONTENTS

Abstract	i
Preface	iii
Acknowledgements	iii
Nomenclature and Abbreviations	v
Contents	vii
1 Introduction	1
1.1 Background	1
1.2 Aim	1
1.3 Limitations	1
1.4 Unmanned Aerial Vehicles	2
1.5 Existing LocalHawk UAV Design	3
2 Literature Review	5
2.1 Fuselage Structures	5
2.1.1 Introduction	5
2.1.2 Loading of Fuselages	5
2.1.3 Fuselage Structural Components	6
2.1.4 Belly Landing of an Aircraft	7
2.2 Low-Velocity Impact Theory	7
2.2.1 Introduction	7
2.2.2 Low-Velocity Impact Failure Modes for Composites	8
2.2.3 Contact Mechanics	8
2.3 Material Selection	9
2.3.1 Introduction	9
2.3.2 Fiber-Reinforced Composites	10
2.3.3 Structural Composites - Laminates and Sandwich Constructions	11
2.3.4 Designing with Composites	11
2.4 Finite Element Analysis	12
2.4.1 Introduction	12
2.4.2 Explicit/Implicit Transient Dynamic Analysis	13
2.4.3 Selecting Software Package	15
3 Method	17
3.1 Landing Parameter Study	17
3.2 Design of Skin and Internal Structure	18
3.2.1 Concept Development	18
3.2.2 Computer Aided Design	18
3.3 Material Selection and Parameters	19
3.3.1 Composite Skin	19
3.3.2 Internal Stiffening Structure	22
3.4 Finite Element Analysis	23
3.4.1 Material Definition and Geometry Preparation	23
3.4.2 Meshing	26
3.4.3 Composite Modeling using ANSYS ACP Composite PrepPost	27
3.4.4 Common Boundary Conditions and Analysis Settings	27
3.4.5 Density Modification and CG Positioning	28
3.4.6 Test Setup	29
3.4.7 Post-Processing	31

4 Results	33
4.1 Landing Parameters Study	33
4.1.1 Pitch (θ)	33
4.1.2 Descend Velocity	34
4.2 Design of Skin and Internal Structure	35
4.2.1 Concept Development	35
4.2.2 Computer Aided Design	40
4.3 Orthotropic Constants Study	41
4.4 Finite Element Analysis	42
4.4.1 Stacking Sequence Testing	43
4.4.2 Pitch Angle (θ) and Descend Velocity Testing	48
5 Discussion	53
5.1 Concept Development	53
5.2 Finite Element Analysis	53
5.3 Future Recommendations	54
6 Conclusion	55
Appendices	61
A Explicit Analyses	63
A.1 Introduction	63
A.2 Pre-Processing	63
A.2.1 Materials Definition	63
A.2.2 Geometry Preparation	63
A.2.3 Contacts and Body Interactions	63
A.2.4 Meshing	64
A.2.5 Boundary Conditions	65
A.2.6 Analysis Settings	65
A.3 Post-Processing	67
A.3.1 Results	67
A.3.2 Evaluating Accuracy	68
B Sample Case - Explicit Analysis Walk-through	69
B.1 Preparation	69
B.2 Pre-Processing	71
B.2.1 Material Definition	71
B.2.2 Meshing	71
B.2.3 Boundary Conditions	75
B.2.4 Analysis Settings	76
B.3 Post-Processing	78
B.3.1 Low-Velocity Impact (LVI)	78
B.3.2 High-Velocity Impact (HVI)	81
C Defining Composites in ACP (pre)	85
C.1 Creating Fabrics and Verifying Imported Data	85
C.2 Importing CAD Geometry for Cutoff Rule	87
C.3 Rosettes and Oriented Element Sets	88
C.4 Modeling Ply Groups	89
D Orthotropic Constants Study	91
E Stacking Sequence Test Results	93
F Pitch (θ) and Descend Velocity Test Results	103

1 Introduction

This chapter aims to give the reader an introduction to the background, aim, and limitations of the thesis. In addition to this, it includes a short section about the history and modern-day application of UAVs, as well as a section summarizing the work done in the LocalHawk summer student project 2012.

1.1 Background

In 2008, Kongsberg Defence Systems (KDS), department of Missile Systems, started a summer student project called LocalHawk. Initially, the purpose was to let students apply their knowledge to practical problems: making a Unmanned Aerial Vehicle (UAV) operate autonomously and be able to recognize objects. Fast forward to 2012, and the scope of the project was extended to include development and building of a UAV which was supposed to fly autonomously and be used for civil purposes, such as sporting events. During the summer of 2012, the mechanics team of the LocalHawk project developed in total three concepts for the airframe of the UAV. Estimated at total weights of 12.5 [kg], all concepts had belly landing as a conceptual solution for landing the UAV. Being limited to a short period of time, no study was conducted to establish the feasibility of belly landing as a conceptual solution.

1.2 Aim

The aim of this thesis is to fulfill the need for a feasibility study of the belly landing solution, given the parameters and design developed during the summer of 2012 in Kongsberg. To achieve this, an explicit Finite Element (FE) solver will be applied to simulate the low-velocity impact of the UAV landing on a surface. A go/no-go decision to either continue with the design as it is, or to make alterations to the design to facilitate belly landing, possibly even scrapping the solution, will be the main output of this thesis. As a bi-product, the documented use of an explicit solver will provide knowledge about the process and how it differs from implicit methods. Existing design of the UAV includes only external surfaces, therefore, two concepts for skin and internal structure will be developed. Summarized, this thesis aims to answer the following questions:

- Is belly landing as a conceptual solution feasible for the LocalHawk UAV?
- If not, what changes could be performed to facilitate belly landing?
- How does the different skin and internal structure concepts perform during belly landing?
- How can an explicit solver successfully be applied to simulate the low-velocity impact of the UAV?

1.3 Limitations

This study has been limited to only one of the three concepts, concept number three (see section 1.5), and the fuselage of this concept. The main reasons for this limitation were that, firstly, airframe concept #1 (see section 1.5) was deemed too conventional, and secondly, airframe concept #2 had issues with too little generated lift. Adding to these reasons, was a perceived reduced complexity of the third concept relative to the second.

In addition to this limitation of one concept, development of concepts for skin and internal structure was in the end limited to not include any alterations of the basic shape of the UAV's external fuselage surface. Other limitations include the use of a simple, rigid, and flat surface without any modeled interaction between the fuselage and the ground except for the deformation of the fuselage, i.e. no friction, and no deformation of the ground. For the composite components, perfect draping was assumed.

1.4 Unmanned Aerial Vehicles

Unmanned Aerial Vehicle (UAV), Unmanned Aircraft System (UAS), Remotely Piloted Aircraft System (RPAS), Remotely Piloted Vehicle (RPV), and drone are all names that can be, and are being, used to describe an aircraft that operates without any on-board personnel. Choosing a simplistic path that conforms with general knowledge of these types of systems, the term Unmanned Aerial Vehicle, or rather the shortening UAV, will be used in this report.

The history of UAVs goes back to the mid 19th century, two years into the American civil war, when Charles Perley registered a patent for a UAV bomber (PBS Nova 2002). Perley's bomber consisted of a hot-air balloon that carried a basket filled with explosives attached to a timing mechanism. During the second World War, Nazi Germany's V-1 (Vergeltungswaffe-1 English: "Revenge weapon"-1) spread terror among the Allies with its purpose; to target non-military targets among the population of Hitler's enemies. Though being a horrible testimony of the cruelty of man, it proved how effective UAVs could be used in combat.

From the American civil war, UAVs have evolved to become highly complex systems with a wide array of application areas. Although many associate modern UAVs with headlines such as "Pakistan Says U.S. Drone Kills 13", (Shah 2009), and "Precisely Wrong: Gaza Civilians Killed by Israeli Drone-Launched Missiles", (HRW 2009), UAVs are currently being used in a wide variety of civil applications such as:

- Oil, gas, and mineral exploration activities (Barnard 2010)
- Climate research (NASA Dryden Flight Research Center 2013)
- Art/Construction (Guizzo 2011)
- Search and rescue (Austin 2010)
- Wildlife conservation (BBC News 2012)
- Fire detection (Austin 2010)
- Road traffic control (Austin 2010)

From the list above, it is possible to conclude that civil applications plays a major role in the presence, and future, of UAVs. An interesting notion was brought forth by The Economist, a weekly news and international affairs publication (Wikipedia 2013), in the article published November 2012 which presented the possibility of unmanned civilian passenger flights being commercialized before autonomous cars (The Economist 2012).

The purpose of producing and operating UAVs as opposed to manned aircraft have been discussed for a long time (Austin 2010). Generally, UAVs have been developed for roles which are dull, dirty, and dangerous (DDD), but Austin (2010) argues that covert, diplomatic, research, and environmentally critical roles should be added to the list. Some examples of DDD applications (Austin 2010):

- Surveillance, either civilian (e.g. livestock) or military, over a long time can be dull, handing the task over to UAVs could allow personnel to focus on other tasks.
- Operating manned aircraft in dirty environments, for instance areas contaminated by radioactive spillage/waste, places the operating personnel in harms way. By possibly increasing safety for humans, the application of UAVs in dirty environments have obvious advantages over manned flights.
- Dangerous: could refer to either defense operations in areas where the aircraft might be attacked by hostile forces, or inspection of power lines and forest fires. As for applications in dirty environments, UAVs represents an increase in safety for personnel which have obvious advantages over manned flight.

1.5 Existing LocalHawk UAV Design

This section summarizes the work done by the Mechanics team the summer of 2012 in the LocalHawk student project at KDS. The aim of this section is to provide insight into the development process and understanding of why concept three looks the way it does. Most of the information presented in this section is based on the author's own experience during the 2012 LocalHawk student project.

The major requirements, put forth by the project owner, which affected the Mechanics team were the minimum payload carrying capacity, desired flight time, operating conditions, and the decision that the UAV should be able to fit in a 0.7x0.7x1.5m crate when disassembled. A minimum payload carrying capacity of 2.5kg, excluding fuel/batteries and motor, meant that the resulting UAV design would be of a considerable size (relative to small hand-launched concepts carrying a payload of less than 0.5kg). One of the earliest decisions made, was to focus on developing a UAV propelled by an electric engine instead of a spark-ignition (SI) engine running on liquid fuel. This decision highly simplified design work as the designers would not have to worry about reduction in mass during flight, or designing fuel tanks that corresponded with safety regulations for highly flammable liquids.

The concept development work consisted of applying Product Development methodology. Starting with a requirement specification for the UAV airframe, the requirements stated by the project owner were developed further and supplemented with requirements from other LocalHawk-internal teams (Cybernetics, Electronics, etc.), legal restrictions, other stakeholders at KDS, and tips given by experienced radio controlled aircraft builders. Based on the requirements specification, a Morphological matrix was used for both idea generation (with the focus on each function individually) and concept synthesis (with the focus being on the overall value of the concept when combining function solutions) as proposed by Almefelt (2011).

Several ideas were proposed, resulting in seven concepts. A coarse selection process was completed using a Systematic selection chart as proposed by Pahl, Beitz, Feldhusen & Grote (2007). The coarse selection shortened the total number of concepts to four. These remaining concepts were put through a finer selection, specifically, the evaluation matrix proposed by Pugh (1990), which resulted in two remaining concepts. Work then proceeded to sizing of the concepts by using the conceptual design methodology for aircraft proposed by Raymer (2012). When the sizing process was completed, focus shifted to designing the concepts in Catia V5. The CAD work comprised the bulk of the effort done during the summer of 2012. With two remaining concepts after the concept selection, each designer worked on his/her own concept. Aiding the CAD work, Computational Fluid Dynamics (CFD) analyses, performed by the supervisor of the mechanics team, helped in refining the shape of the airframes.

Nearing completion of the 2012 part-project, the two concepts were presented to the stakeholders. A desire of more radical designs was put forth. Heeding this desire, as well as a need for more lift (wing area), the designers developed concept three using the second concept as a reference. In Figure 1.1, the third concept can be seen, while in Figure 1.2 a side cut-view of the fuselage can be seen with the placement of the internal components.

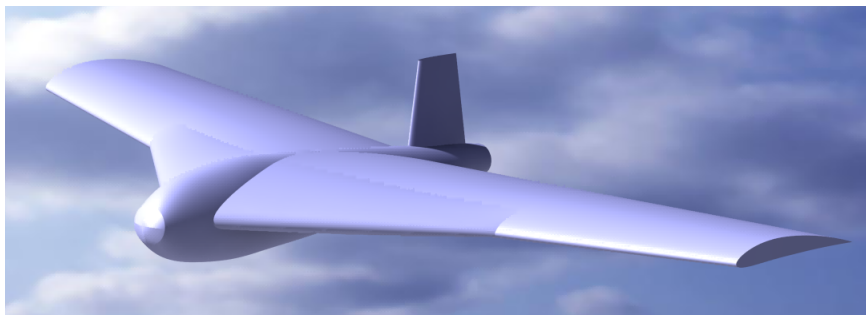


Figure 1.1: *Rendering of the third LocalHawk airframe concept*

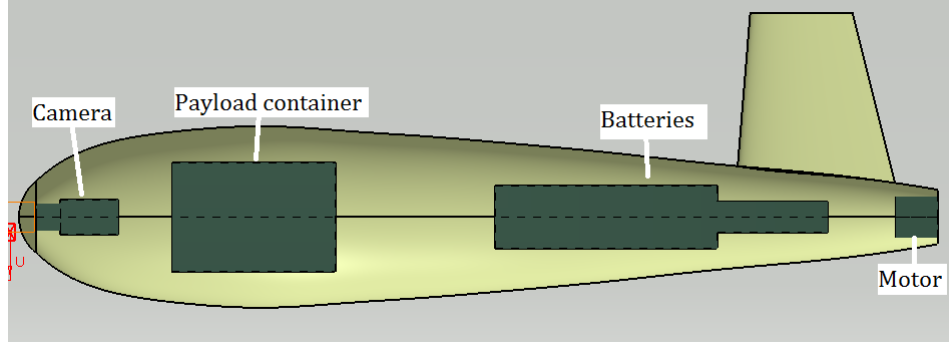


Figure 1.2: *Cut-view of the third LocalHawk airframe concept showing the position of the internal components*

A major cause of uncertainty during the entire design process was the size of the payload components. The Image-processing team responsible for the choice of on-board camera and Graphics Processing Unit (GPU) board, had a hard time specifying the dimensions of the GPU board as it had not yet been released to the market. An overly-pessimistic estimation was performed, which resulted in the fuselage designs being bulky and taking up much of the reference area for the wings. In turn, this meant that, with the size restrictions of the carrying crate, the UAV design concepts would not fly with an estimated total weight of 12.5kg. Modifications were performed, and late information from the GPU board manufacturer considerably reduced the size estimate, so that the fuselage designs could be narrowed and more stream-lined.

2 Literature Review

This chapter contains the theoretic background that will provide a foundation for the rest of the thesis work. The aim is to give the reader an introduction to necessary theory in such a way that he/she is able to understand and interpret the selected methods, and obtained results.

2.1 Fuselage Structures

In this section, an introduction to some of the important characteristics of aircraft fuselages is presented. General loading of fuselages is included to provide the reader with a picture of what a fuselage is subjected to during its flight cycle. Continuing, section 2.1.3 contains standard solutions of fuselage structural components designed to accommodate the previously described loads.

2.1.1 Introduction

Firstly, a distinction between the term "airframe" and the term "fuselage" needs to be done: According to the Merriam-Webster online dictionary, an airframe is defined as: "the structure of an aircraft, rocket vehicle, or missile without the power plant" (Merriam-Webster 2013*a*). While fuselage is defined as: "the central body portion of an aircraft designed to accommodate the crew and the passengers or cargo" (Merriam-Webster 2013*b*). In other words, the fuselage is part of the airframe and refers only to the central body of the aircraft.

As stated by the Merriam-Webster dictionary definition of fuselages, the main task of the fuselage is to carry the payload of the aircraft. Megson (2010) adds that the basic functions of an airframe are to transmit and resist the applied loads, to provide an aerodynamic shape, and to protect onboard passengers, systems, as well as other payload against environmental conditions.

2.1.2 Loading of Fuselages

Franklin (2010) divides the loads experienced by aircraft into two categories; *external loads* and *internal loads*. External loads include aerodynamic and inertia loads, while internal loads refer to loads distributed within the airframe, carried by the structural components.

While the wing sections of the airframe are subjected to elevated aerodynamic forces from the pressure distribution generating lift, the aerodynamic loading on the fuselage is relatively low (Megson 2010). The dominating internal loading of the fuselage is the concentrated loads originating from the supports of wings, tail, and undercarriage. Adding to these loads is the external inertia loads stemming from the mass of the airframe, power plant, and payload.

The general aerodynamic and inertial loading of an airframe during flight can be presented using a V - n diagram, describing the flight envelope of the aircraft. A V - n diagram gives the maximum design, positive and negative, vertical load factor, commonly referred to as g-forces, as well as the maximum velocity and stall lines of the aircraft (Franklin 2010). An example V - n diagram is shown in Figure 2.1.

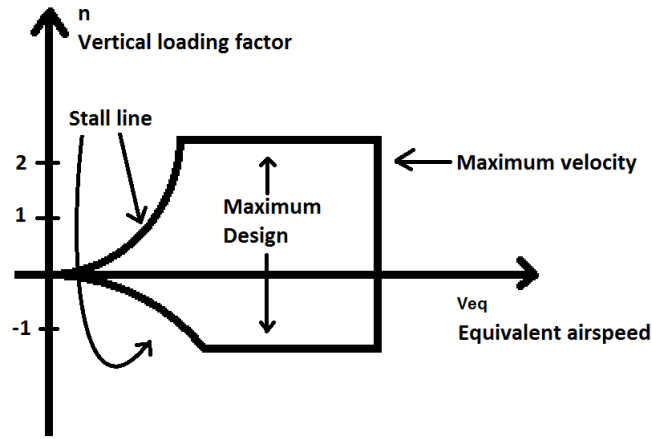


Figure 2.1: *Example V-n diagram*

Inertial loads are described using Newton's second law ($F = ma$), and originates from various maneuvers and external accelerations such as gusts (Raymer 2012). According to Raymer (2012), the critical loads for the fuselage of a L1011 transport aircraft is maneuvering (positive, negative, yaw, and lateral) as well as braking and gusts (positive dynamic and lateral). These loads are all by definition inertial loads (originating due to an acceleration), and the load severity is assumed to be transferable to a subsonic UAV. Most likely, without a landing gear, whose objective it is to reduce the landing load to an acceptable level (Raymer 2012), the landing-impact load could be added to this list. Impact theory is treated in detail in section 2.2.

2.1.3 Fuselage Structural Components

The overall purpose of the structural components of a fuselage is to provide load paths which connect opposing forces (Raymer 2012). Although they all aim to meet the same end goal, several different solutions have been developed to best resist the applied loads, and are now standard structural components. The loads presented above result in bending, torsion, and shear, all of which the structural components must be designed for. Presented in Figure 2.2 are the most common solutions for providing resistance towards bending (Raymer 2012).

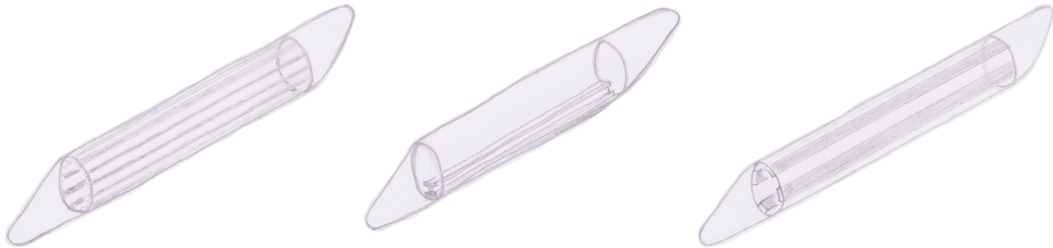


Figure 2.2: *Common structural components. Left: Stringers, mid: Keelson, right: Longerons. Inspired by Raymer (2012).*

Being a relatively large, solid beam, the keelson provides a great deal of longitudinal stiffness and prevents bending in the lower part of the fuselage (Raymer 2012). Longerons fulfil the same purpose as the keelson, providing bending resistance, but are used either in combination with a keelson (Raymer 2012), or without any supplementary elements (Franklin 2010). According to Raymer (2012), longerons are used in fuselages that are subjected to highly concentrated loads and which have relatively many cutouts (ex: fighter jets). Stringers on the other hand, are used in fuselages that have relatively few cutouts and concentrated loads (ex: transport aircraft). By applying stringers instead of longerons, it is possible to increase the spacing between the frames (Franklin 2010). The stringers and longerons are placed around the circumference of the fuselage as can be seen from Figure 2.2. Common for all of the longitudinal stiffening elements are the design goal of keeping them as straight as possible to reduce weight (Raymer 2012).

An alternative solution to the longerons, keelson, and stringers, is the sandwich-skin approach (Franklin 2010). Compared to the stringers and longerons approaches, a sandwich skin increases the necessary spacing between frames, ultimately reducing the total number of frames. A sketch of the sandwich-skin approach can be seen in Figure 2.3.

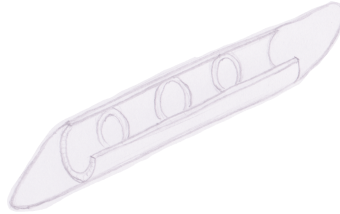


Figure 2.3: *The sandwich-skin fuselage with frames included in the sketch. Inspired by Franklin (2010).*

2.1.4 Belly Landing of an Aircraft

Loading experienced by the fuselage during a belly landing generally varies with the flight-approach parameters such as descent velocity (vertical velocity), approach velocity (horizontal velocity), and pitch angle (θ). A study of the effects these parameters have on the impact loading will be performed using a simplified model in an explicit Finite Element (FE) solver.

Landing surface also play a major role, it is easy to imagine the difference between landing, and skidding, on soft grass as opposed to hard tarmac or coarse gravel. For more information on impact loading see section 2.2.

2.2 Low-Velocity Impact Theory

This section aims to give the reader an introduction to the basic theory of Low-Velocity Impacts. It is included here to provide an insight into what the UAV will experience during landing.

2.2.1 Introduction

The term *impact* describes the collision between two bodies identified by a generation of relatively high forces over a short period of time (Meriam & Kraige 2008). According to Meriam & Kraige (2008), impacts are complex processes involving material deformation and transformation of mechanical energy to sound and heat. Impact processes are generally classified by the degree of kinetic energy that is conserved after the impact (Lien & Løvholden 2001):

- Elastic - Total conservation of kinetic energy
- Inelastic - A part of the kinetic energy is conserved, the rest is transformed into other states of energy
- Totally Inelastic - Maximum transformation of kinetic energy, the two objects stick together and move with a common velocity

Another method of classifying impact processes is by using impact velocity, i.e. low and high velocity impacts (Richardson & Wisheart 1996). The transition between low and high velocity depends on the target stiffness, material properties, and the impactor's stiffness and mass. A high-velocity impact is dominated by the propagation of an impact stress wave, resulting in localized damage. This process is independent of boundary conditions as the material does not have time to react.

Richardson & Wisheart (1996) presents several views on how to define low-velocity impacts:

- Sjöblom, Hartness & Cordell (1988) argues that for low-velocity impacts, it is possible to model the impact process using a quasi-static approach. For a stiff, light-weight structure this "may be on the order of tens of m/s ".

- Cantwell & Morton (1991) describes several impact testing procedures for composites. Charpy pendulum, the Izod impact test, Drop-weight impact tests, and hydraulic test machines are all methods for testing low-velocity impacts, which Cantwell & Morton (1991) defines as being up to 10 m/s .
- Robinson & Davies (1992) presents a relation between the failure strain ϵ , impact velocity V_0 , and the speed of sound in the material C :

$$\epsilon = \frac{V_0}{C} \quad (2.1)$$

For failure strains in composites on the order of 0.5–1.0%, the resulting transition from low to high-velocity impacts occurs between 10 – 20 m/s (Robinson & Davies 1992).

The LocalHawk UAV has an assumed descend-velocity of much less than 10 m/s , which according to the above-presented views, classifies it as a low-velocity impact event.

2.2.2 Low-Velocity Impact Failure Modes for Composites

Richardson & Wisheart (1996) argue that the dynamic response of the structure is important in low-velocity impacts since the impact duration is long enough for the entire structure to react. Since the impact spreads energy throughout the entire structure, it is not only the surface in direct contact with the impactor/target that is susceptible to damage. For a composite structure, there are four main modes of failure (Richardson & Wisheart 1996):

- Matrix cracking
- Delamination
- Fibre breakage
- Penetration

Matrix cracking is normally the first failure mode to occur in a composite subjected to transverse low-velocity impacts (Richardson & Wisheart 1996). The cracks appear due to mismatched properties of the fibers and the matrix, and they grow parallel to the fiber orientation.

Delamination between fibers occurs due to off-axial loading, i.e. loading not parallel to the fiber orientation (see section 2.3.2) (Zenkert & Battley 2011). In a laminate structure, the crack will grow in the interface between the matrix and the fiber. Richardson & Wisheart (1996) adds that the crack grows between plies of different fiber orientation, and not between lamina in the same ply group.

Fiber failure occurs only in the late stages of the total failure, after the matrix has cracked and delamination has taken place, and is the last failure mode before total penetration (Richardson & Wisheart 1996). The fibers fail beneath the impactor due to localized high stresses and indentation, but also on the opposite side of the structure due to bending.

Penetration is the last stage of failure and occurs when the extent of fiber failure in the impact zone is great enough for the impactor to fully penetrate the material (Richardson & Wisheart 1996). At this point, the structure is ruined and efforts must be made to prevent the extent of the damage ever reaching this stage.

2.2.3 Contact Mechanics

According to Abrate (2001), local indentation has a major influence on the contact force. He argues that the contact phenomenon is generally assumed to be rate independent so that statically determined contact laws can be used. The impact can be divided into two phases; loading and unloading. Contact force during the loading phase is calculated using the formula (Abbate 2001):

$$P = k\alpha^{\frac{3}{2}} \quad (2.2)$$

Where α is the indentation and k , the contact stiffness, is given by:

$$k = \frac{4}{3}ER^{\frac{1}{2}} \quad (2.3)$$

Where the R and E parameters are defined as:

$$\frac{1}{R} = \frac{1}{R_1} + \frac{1}{R_2} \quad (2.4)$$

$$\frac{1}{E} = \frac{1 - \nu_1^2}{E_1} + \frac{1 - \nu_2^2}{E_2} \quad (2.5)$$

Here, R is the radius of curvature, E is the Young's modulus, ν is the Poisson's ratio, and subscripts 1 & 2 denotes indenter and target respectively. Equation (2.2) is usually called the Hertzian law of contact (Abrate 2001).

Although ending this very short introduction to contact mechanics here, it is possible to identify some general trends from equations (2.2) through (2.5):

- The contact force is proportional to the radius of curvature for a given indentation. If equation (2.2) is turned around to return the indentation for a given contact force, it is inversely proportional to the radius of curvature for both indenter and target, highlighting the importance of a smooth impact area to reduce indentation.
- The contact force is proportional to the Young's modulus of the indenter & target materials, which means that the "stiffer" the material, the higher contact force the bodies will experience for a given indentation.

2.3 Material Selection

This section addresses the topic of choosing the material of the different sections of the LocalHawk UAV fuselage. If all possible materials were to be considered, this could be the topic for an independent thesis. Therefore, this section will be limited to evaluating glass-fiber-reinforced polymers (GFRP, fiberglass) and carbon-fiber-reinforced polymers (CFRP).

2.3.1 Introduction

Materials chosen for manufacturing of the LocalHawk UAV will have to facilitate the type of loading presented in sections 2.1.2 and 2.2.

Some of the more important design parameters for materials used in aircraft design is *specific strength* and *specific stiffness*, here, *specific* signifies the property in relation to the density of the material. Specific strength is defined as the ultimate tensile strength divided by the material density, and specific stiffness is defined as the Young's modulus of the material divided by density (Franklin 2010). This specification of properties relative to the mass of the material is in accordance with the all-important requirement when designing aircraft: keeping the weight at a minimum level.

Other factors that should be considered when choosing materials for an aircraft are temperature and corrosion. Galvanic corrosion could be a risk for electrically dissimilar materials such as aluminum and carbon-fiber composites (Raymer 2012).

Determining the actual skin temperature is difficult as one has to take into consideration airflow conditions, surface finish, and atmospheric conditions. However, the highest theoretical skin temperature is determined using the stagnation temperature (Raymer 2012):

$$T_0 = T (1 + 0.2M^2) \quad (2.6)$$

Where the ambient temperature, T , is specified in $[K]$, and M is the flight Mach number. Operating at low altitudes and with a relatively low flight Mach number, problems regarding skin temperature are assumed to be negligible for the LocalHawk UAV. However, the internal engine mounts could experience elevated temperatures, especially for maneuvers requiring maximum thrust. Material selection for the engine mounts should therefore be performed with this in mind.

2.3.2 Fiber-Reinforced Composites

The main purpose of the fiber phase of a fiber-reinforced composite is to provide strength (Callister 2007). There are two main types of fiber-reinforced composites; chopped-fiber reinforced (whisker) or filament reinforced (fiber) (Raymer 2012). Both types consist of fibers enveloped in a matrix, but for the whisker-reinforced composite, short fibers randomly oriented in the matrix are applied which results in an isotropic material. A fiber-reinforced composite on the other hand, utilizes fibers that are longer and oriented in a non-arbitrary direction. As opposed to whisker-reinforced composites, fiber-reinforced composites are anisotropic, meaning their physical properties (here: strength) are dependent on material direction (*Oxford Dictionary of Physics* 2005).

Fibers come in several forms ready for manufacturing, the most common are loose or batting (for whisker reinforcement), unidirectional tape, unidirectional fabric, and bidirectional fabric (Raymer 2012). The unidirectional tape consists of continuous fibers pre-impregnated with a polymer resin which is only partially cured; unidirectional tape is often called *prepreg* (Callister 2007). Fabrics can also be prepreg and comes either with a unidirectional (all fibers in the same direction) or in a bidirectional (0 deg, 90 deg) layup (Raymer 2012).

The matrix phase serves several purposes, firstly, it binds the fibers together and transfer loads to the fibers (Callister 2007). Secondly, it protects the fibers from surface damage and hinders the propagation of brittle cracks from fiber to fiber.

GFRP composites, or more commonly known as fiberglass, are the most produced type of composites (Callister 2007). Fiberglass consist of glass fibers either oriented continuous (fiber-reinforced) or discontinuous (whisker-reinforced) in a polymer matrix. According to Callister (2007) there are several reasons for why glass is used as a fiber-reinforcement material:

- Molten glass is easily drawn into fibers.
- Easily accessible and cheap to manufacture using various techniques.
- High strength, when used in a polymer matrix, the result is a composite with a high specific strength.
- GFRP composites are applicable in corrosive environments due to the glass and polymer composite being chemically inert.

According to Megson (2010), GFRP composites were used at the introduction of composite materials to the aircraft-manufacturing industry. However, GFRP composites do unfortunately possess a low level of stiffness, so that application areas in fixed-wing aircraft are limited (Megson 2010). However, many small or medium sized UAV designs are built using GFRP composites instead of CFRP composites due to their inherent damping capabilities (much lower Young's modulus) and low cost (Austin 2010).

CFRP composites consist of carbon fibers in a polymer matrix and are the most used advanced¹ composite material (Callister 2007). Several properties have made CFRP composites so popular (Callister 2007):

- Of all fiber-reinforcing materials, carbon fibers have the highest specific Young's modulus and specific strength.
- Even at elevated temperatures, carbon fibers keep their high strength.
- Carbon fibers does not react, at room temperature, with many solvents, acids, bases, and is unaffected by moisture.
- Many manufacturing methods have been developed, thereby reducing the cost of production.

However, Raymer (2012) reports that in 2012, the cost of CFRP composites was approximately twenty times that of aluminum (please note that the material waste is less for composites than for metals during manufacturing). Another possible drawback with using CFRP composites is their brittleness which results in a sudden failure instead of plastic yielding in zones of load concentrations (Megson 2010). Adding to this is the poor resistance to impacts which may result in internal damage not visible under normal inspections. According to Megson (2010), CFRP laminates have approximately a Young's modulus of three times that of GFRP laminates, but the strength does not differ that much.

¹According to Callister (2007), *advanced* here translates to *not fiberglass*

2.3.3 Structural Composites - Laminates and Sandwich Constructions

As mentioned in section 2.3.2, laminates are built up by first stacking plies of oriented fibers in a predetermined sequence and then cementing (curing) the plies together to form a laminate (Callister 2007). The stacking sequence determines the strength properties of the laminate and can be performed in infinitely different combinations (Raymer 2012). Ply orientation is up to the designer to decide, but some of the more common methods are (Raymer 2012):

- 0 deg, provides strength in the direction of the principal axis.
- 0 deg / 90 deg, provides strength in both the direction of the principal axis and the transverse direction.
- ± 45 deg: Two plies provides some strength in the direction of the principal axis and good shear strength in the principal axis direction. Also used for structures subjected to torque.
- 0 deg / ± 45 deg / 90 deg: The four ply orientations provide good strength in both the principal axis direction and the transverse direction, as well as good shear strength.

A preliminary-design rule-of-thumb, the Ten-Percent Rule proposed by Hart-Smith (1992), states that for 0 deg / ± 45 deg / 90 deg laminates, the 0 deg ply contributes 100% strength in the principal (0 deg) direction, while the other plies contribute with 10% strength in the principal direction each.

Sandwich panels consist of two sheets bonded, using an adhesive or welding, to a thicker core (Callister 2007). The sheets are usually made of a stiff and strong material, such as fiber-reinforced polymers, while the core could either be a honeycomb structure or a solid material such as foam or balsa wood. Having a much higher Young's modulus than the core, the purpose of the skin is to cope with stress due to tension and compression, as well as in-plane shear loads, while the core provides (out-of-plane) shear strength and resistance towards buckling (Franklin 2010). In addition, the core provides thickness between the faces, thereby increasing the second moment of area for resistance against bending. By binding the two sheets together, the core also provides shear continuity so that the sandwich acts as one structural entity. Joining the sheets to the core is of paramount importance for a sandwich structure (Franklin 2010). For composite sheets, an adhesive bond is normally applied. Franklin (2010) stresses the importance of taking into consideration the weight of the adhesive when deciding whether to apply sandwich structures instead of other alternative structures, as the total weight can be significant for a large area.

Raymer (2012) reports that for aircraft applications, the core normally is a honeycomb structure made of aluminum or a phenolic material, but that for home-built aircraft, rigid foam is often used instead. This is supported by the design-proposition made by Austin (2010) in section 2.3.4.

Although sandwich structures could provide good specific-strength properties, there are some possible drawbacks related to the application of sandwich structures (Franklin 2010):

- Moisture could become trapped between the core and the sheets. If subjected to below-freezing temperatures, this moisture could freeze, causing separation between the sheet and the core.
- If the sheets are very thin, damage from impacts could be severe.

However, Franklin (2010) stresses that these drawbacks could be mitigated by "proper design practices".

2.3.4 Designing with Composites

Designing with composites as opposed to metals can provide a weight saving for the structural parts of 25% (Raymer 2012). However, optimal weight-saving depends on the designer designing with composites in mind from the outset of the design process. Maximizing the potential of composites requires an understanding of how the material is manufactured and how it influences the design.

The most basic difference is, as presented in section 2.3.2, that the fiber-reinforced composite materials are anisotropic, as opposed to an isotropic metallic material. Fiber orientation determines the direction in which the material is strongest, and therefore also in which direction the material is weakest (Franklin 2010). Also important to remember, is that composites generally perform poorly when subjected to concentrated loads (Raymer 2012). Therefore, joints and fittings that evenly distribute the loads should be applied.

An example of a common fuselage design for small or medium UAV designs, presented by Austin (2010), is the application of fiberglass to produce the skin, which is then supported by stringers made up of a stiff plastic foam core wrapped with carbon-fiber tape. This reduces cost drastically as the fiberglass is much cheaper than carbon fiber, and the carbon-fiber tape is cheaper than carbon-fiber cloth. A sought-after property of this design is the inherent damping capabilities of fiberglass as opposed to the stiffer carbon fiber, making the structure less prone to shattering upon an impact.

2.4 Finite Element Analysis

This section contains an introduction to the basic theory of the Finite Element Method (FEM) and how this is applied when performing a Finite Element Analysis (FEA). The aim of this section is to give the reader an understanding of why the chosen software and solution method is selected, as well as a basic understanding of the theory which is the foundation for the Finite Element Method.

2.4.1 Introduction

FEM is used in a wide variety of applications such as structural engineering, thermodynamic, bio-medical engineering, mechanical design, hydrodynamics, electromagnetic analyses, as well as other areas (Rao 2011).

The basic idea of FEM is to simplify a physical problem by dividing the problem geometry/area into several smaller sub-elements which are connected to each other (Rao 2011). This process is in FEM called *meshing*, and consists of building a representation of the geometry (for non-field problems, for example: structural analysis) using a variety of elements. The elements can either be 1D (beam, truss elements), 2D (quadrilateral, triangular elements), or 3D (tetrahedron, cubic elements), see Figure 2.4 for a sketch showing the most basic 1D, 2D, and 3D elements.

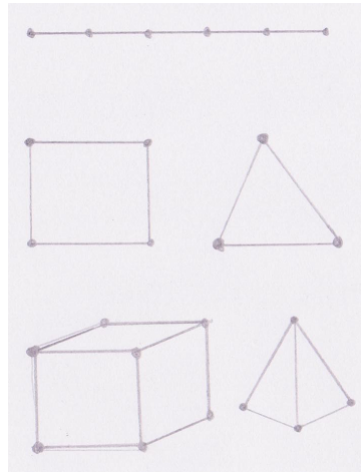


Figure 2.4: *Basic FEM elements. Top: five two-noded 1D elements, mid left: quadrilateral 2D element with four nodes, mid right: triangular 2D element with three nodes, bottom left: cubic eight-noded 3D element, bottom right: tetrahedral 3D element with four nodes.*

By applying this simplification it is possible to obtain an approximate solution to the physical problem, and often it is possible to increase the accuracy by increasing the number of elements. As an example of accuracy when it comes to geometry representation, the effect of a mesh refinement, when using elements with straight edges only, is shown in Figure 2.5.

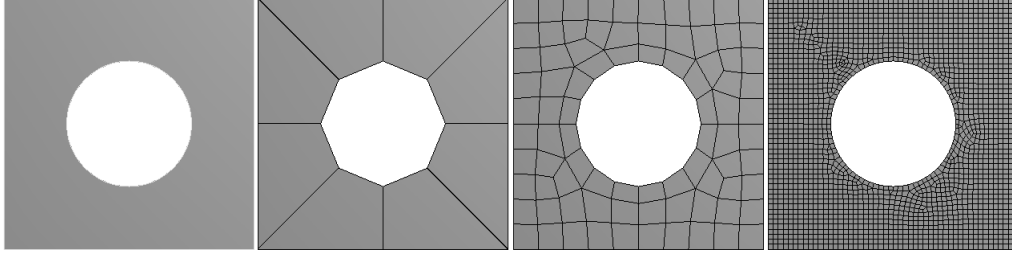


Figure 2.5: *Mesh refinement; left: original geometry, second from left: coarse FE mesh, second from right: medium-coarse FE mesh, right: very fine FE mesh. Mesh produced using Ansys 14.5 Academic Research License.*

Although very important and directly linked to CPU solve time, the size of the mesh generally does not solely dictate the possible scope of an analysis anymore. Modern computers and their computational capabilities have allowed the main focus to shift to whether or not the problem is modeled correctly. Modeling is the process where the physical problem is reproduced in a modeling environment, for instance FEA software. Correct definitions of contacts, boundary conditions (forces, supports, temperature etc.), and simplifications are essential to obtain a realistic approximation.

For a static structural analysis the global equation to be solved is (Rao 2011):

$$\mathbf{K}\mathbf{u} = \mathbf{f} \quad (2.7)$$

Where \mathbf{K} is the global stiffness matrix, \mathbf{u} is the global nodal displacement vector, and \mathbf{f} is the nodal force vector. By inverting the stiffness matrix and multiplying each side of equation (2.7) with it, the nodal displacement can be found:

$$\mathbf{u} = \mathbf{K}^{-1}\mathbf{f} \quad (2.8)$$

For a linear structural analysis these displacements could then be used to calculate the element strains and stresses (Rao 2011).

For a more in-depth explanation of the Finite Element Method, please see a textbook devoted to FEM such as Liu & Quek (2003), Rao (2011), or Taylor, Nithiarasu & Zhu (2005).

During this thesis project, a commercial pre-/post-processing software and solver will be applied to conduct the FEA. Utilizing commercial software eliminates the need to write a solver script from scratch, and greatly increases the possible scope of the project. Numerous different software solutions are available, and most of them fulfill the requirements of this project, but they are not necessarily readily available with a student/academic license without constraining limitations. These limitations could be a maximum number of nodes, availability of specific solvers, and/or period of license validity. The choice of software package is addressed in section 2.4.3.

2.4.2 Explicit/Implicit Transient Dynamic Analysis

Transient problems are characterized by dynamic, time-dependent loads exerted on the structure. Often, a method called *direct integration* is used to solve these types of problems due to its intuitiveness (Liu & Quek 2003). The basic ordinary differential equation this method aims to solve is (Taylor et al. 2005):

$$\mathbf{M}\ddot{\mathbf{u}} + \mathbf{C}\dot{\mathbf{u}} + \mathbf{K}\mathbf{u} + \mathbf{f} = 0 \quad (2.9)$$

Where \mathbf{M} is the mass matrix, \mathbf{C} is the matrix of damping coefficients, \mathbf{K} is the stiffness matrix, \mathbf{f} is the nodal force vector, $\ddot{\mathbf{u}}$ is the nodal acceleration vector, $\dot{\mathbf{u}}$ is the nodal velocity vector, and \mathbf{u} is the vector containing the displacement of all the nodes.

Direct integration can be divided into two different main categories: *implicit* and *explicit* (Liu & Quek 2003). According to Liu & Quek (2003), implicit methods are generally preferable for application in slow problems, while explicit methods are preferable for rapid phenomena such as impacts. To explain the difference between implicit and explicit methods, a derivation of a first-order transient equation to obtain an approximation of \mathbf{u}_{n+1} , where the subscript $n + 1$ indicates the displacement for the next time step, is performed (Taylor et al. 2005):

$$\mathbf{C}\dot{\mathbf{u}} + \mathbf{K}\mathbf{u} + \mathbf{f} = 0 \quad (2.10)$$

Assuming that \mathbf{u} follows a polynomial, the lowest, linear, expansion gives:

$$\mathbf{u} \approx \hat{\mathbf{u}}(t) = \mathbf{u}_n + \frac{\tau_{\Delta t}}{\Delta t} (\mathbf{u}_{n+1} - \mathbf{u}_n) \quad (2.11)$$

Where $\tau_{\Delta t}$ is the current duration of the time step in question; $\tau_{\Delta t} = t - t_n$ (see Figure 2.6).

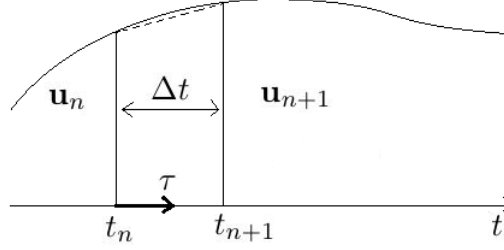


Figure 2.6: *Time step in a transient FEM analysis. Inspired by Taylor et al. (2005).*

It can be shown that the weighted equation to be solved is (Taylor et al. 2005):

$$\int_0^{\Delta t} W(\tau_{\Delta t}) [\mathbf{C}\dot{\mathbf{u}} + \mathbf{K}\hat{\mathbf{u}} + \mathbf{f}] d\tau_{\Delta t} = \mathbf{0} \quad (2.12)$$

Introducing a weighting parameter θ_w :

$$\theta_w = \frac{1}{\Delta t} \frac{\int_0^{\Delta t} W(\tau_{\Delta t}) \tau_{\Delta t} d\tau_{\Delta t}}{\int_0^{\Delta t} W(\tau_{\Delta t}) d\tau_{\Delta t}} \quad (2.13)$$

we get:

$$\frac{1}{\Delta t} \mathbf{C} (\mathbf{u}_{n+1} - \mathbf{u}_n) + \mathbf{K} [\mathbf{u}_n + \theta_w (\mathbf{u}_{n+1} - \mathbf{u}_n)] + \bar{\mathbf{f}} = \mathbf{0} \quad (2.14)$$

where $\bar{\mathbf{f}}$ is an average value of \mathbf{f} :

$$\bar{\mathbf{f}} = \frac{\int_0^{\Delta t} W \mathbf{f} d\tau_{\Delta t}}{\int_0^{\Delta t} W d\tau_{\Delta t}} \quad (2.15)$$

$$\bar{\mathbf{f}} = \mathbf{f}_n + \theta_w (\mathbf{f}_{n+1} - \mathbf{f}_n) \quad (2.16)$$

Solving equation (2.14) for \mathbf{u}_{n+1} gives:

$$\mathbf{u}_{n+1} = (\mathbf{C} + \theta_w \Delta t \mathbf{K})^{-1} [(\mathbf{C} - (1 - \theta_w) \Delta t \mathbf{K}) \mathbf{u}_n - \Delta t \bar{\mathbf{f}}] \quad (2.17)$$

From equation (2.17) it is possible to conclude that for values of $\theta_w > 0$, a matrix inversion needs to be performed, such methods are called implicit. When $\theta_w = 0$, and \mathbf{C} is replaced by a lumped equivalent matrix, no matrix inversion is needed and this is called explicit methods (Taylor et al. 2005). A "lumped" matrix is the opposite of a "consistent" matrix which consists of off-diagonal elements (Taylor et al. 2005). For a mass matrix one assumes that the material on the mean locations on either side of the nodal displacement in question, behaves like a rigid body, and the rest of the element does not participate in the motion, thereby excluding the dynamic coupling that exists between the element displacements (Rao 2011). This assumption "removes" the off-diagonal terms in the mass matrix, making it "lumped".

According to Imaoka (2001), the most CPU demanding operation is matrix inversion, and Rao (2011) argues that a diagonal matrix requires less storage space than a matrix with off-diagonal terms, thus underlining the

numerical benefit of replacing matrix inversion with matrix multiplication.

The difference between explicit and implicit methods could be summarized to the following; implicit methods involve unknown parameters for time-step $n + 1$ in the calculation of \mathbf{u}_{n+1} while explicit methods rely solely on known parameters. This could be exemplified by inserting eq. (2.16) into eq. (2.17):

$$\mathbf{u}_{n+1} = (\mathbf{C} + \theta_w \Delta t \mathbf{K})^{-1} [(\mathbf{C} - (1 - \theta_w) \Delta t \mathbf{K}) \mathbf{u}_n - \Delta t (\mathbf{f}_n + \theta_w (\mathbf{f}_{n+1} - \mathbf{f}_n))] \quad (2.18)$$

From eq. (2.18), it is possible to conclude that for values of $\theta_w \neq 0$, unknown values of $\bar{\mathbf{f}}(\mathbf{f}_{n+1})$ is included in the calculation. Inserting $\theta_w = 0$ into eq. (2.18) yields:

$$\mathbf{u}_{n+1} = \mathbf{C}^{-1} [(\mathbf{C} - \Delta t \mathbf{K}) \mathbf{u}_n - \Delta t \mathbf{f}_n] \quad (2.19)$$

By inspecting eq. (2.19), and assuming that \mathbf{C} is calculated using only known values, it is possible to conclude that an explicit method does not require any iteration since all elements of the equations are known.

One advantage of implicit methods is that they are *unconditionally stable*, which in practice means that the size of the time steps can be relatively large (Taylor et al. 2005). This makes the implicit method good for long lasting, smooth transient problems. The explicit methods are on the other hand *conditionally stable*, meaning that they have a maximum limit for the size of the time step. According to Sun, Lee & Lee (2000), the maximum Δt must be less than the shortest time it takes a dilatational wave to cross any element in the mesh:

$$\Delta t \leq \frac{2}{\omega_{max}} \quad (2.20)$$

Where ω_{max} is the maximum eigenvalue of the element. A conservative estimate of the time increment is the minimum value for all elements (Sun et al. 2000):

$$\Delta t = \min \left(\frac{L_e}{c_d} \right) \quad (2.21)$$

Where L_e is the characteristic element dimension and c_d the dilatational wave speed in the material.

According to Ansys (2012), the time increment for an explicit analysis, which is constrained to facilitate stability in a commercial solver, is proportional to the smallest element dimension, and inversely proportional to the speed of sound in the material used.

Simulia (2012) states that an implicit analysis including complex contact and/or material definitions could require many iterations which would increase solve time. In such a situation, they argue that an explicit solver would be preferable as it does not iterate but advances explicitly through the time steps. Sun et al. (2000) reported in their comparison of explicit and implicit finite element methods for dynamic problems, that for fast contact problems (here: 0.002s as opposed to 1s which was considered slow), the computational cost for explicit methods were about one tenth that of implicit methods. However, Sun et al. (2000) continues with reporting that for a given slow problem, explicit methods resulted in a CPU time of 1 h and 17 min while application of implicit methods took 10 min.

Deciding whether to apply an implicit or explicit solver depends on the problem at hand. For an impact analysis of a short duration, the choice falls on an explicit method. This is due to the advantages an explicit solver has when it comes to dealing with large deformations, highly dynamic events, and the reduced cost relative to an implicit solver for a short, highly dynamic event. The decision to utilize an explicit solver for an impact analysis of a UAV during belly landing, match the decisions of Yüksel (2009) and Akhilesh, Sathyamoorthy, Bharath & Laxminarayan (2012).

2.4.3 Selecting Software Package

A commercial pre-/post-processor as well as solver will be used to perform the analyses. Important factors for choosing software are accessibility, performance capabilities, student/academic license limitations, and ease-of-use. The FE software packages Abaqus/CAE, MSC Patran/Nastran, and Ansys Workbench have been examined.

"Accessibility" refers to whether or not a license is available, either through Chalmers, Kongsberg Defence Systems, or a general student license. Depending on the license, limitations of model size (total number of

nodes), analysis types available, and available support may exist. As discussed in section 2.4.2, the software should include an explicit solver.

MSC Patran/Nastran is available for students with a general student license applying limitations to the total number of nodes to 5000, as well as excluding the SOL 700 explicit analysis. MSC's on-line student center offers an extensive set of tutorials. However, considering the limitations included in the student license, MSC Patran/Nastran is found unfit for this project.

Dassault Systèmes, Simulia, offers Abaqus/CAE with Abaqus/Explicit and a maximum node limitation of 1000 nodes. As reported by Yüksel (2009), 1000 nodes could result in inaccurate results for a problem of this nature. Taking the node limitation into consideration, Abaqus is also found unfit for this project.

Chalmers has an Academic Research license available for Ansys which includes the explicit dynamics toolbox Autodyn. Combining the explicit capabilities with unlimited nodes and available tutorials through their on-line support center, Ansys Workbench is found to be the preferred software solution.

3 Method

This chapter contains a step-wise description of the methods utilized in this thesis. Starting out with a study of how different landing parameters influence the UAV during landing, critical parameters and design cases for the FEA were identified. Basic concept development methodology was applied in the design of the internal structure before the concepts were modeled and made ready for FEA using CAD software. Manufacturers of composite materials were contacted to obtain parameters for eligible prepreg materials, based on input from a manufacturer, both in the form of parameters and qualitative recommendations, a material for the UAV's skin was chosen.

Laminate definition was performed using the ACP Composite PrepPost tool for Ansys 14.0. Different stacking sequences were examined, scrutinizing the strength of each test sequence lead to a preferred stacking sequence tailored for the belly-landing of the LocalHawk UAV. Using this preferred laminate, tests with varied descend velocity and pitch angle created a set of results used to evaluate concept viability.

3.1 Landing Parameter Study

A landing-parameter study was conducted with the aim of identifying conditions under which the UAV would experience desirable or undesirable loading conditions. Approaching the problem conservatively dictates that the most undesirable loading conditions, within the UAV's operational range, should be modelled in the FEA. Benefits of approaching the problem conservatively include that a fuselage designed for the worst case scenario is inherently capable of dealing with more preferable loading conditions. However, an overly-conservative approach may result in unnecessary structural reinforcement which increases weight and could render the UAV unfit for flight.

A hollow model of the basic UAV fuselage, without any cutouts, was imported into an explicit analysis environment in Ansys 14.5 and appointed an isotropic material. The fuselage had a thickness of 3 [mm], and the geometry also included a thin, rigid section representing the ground. Being a simplistic analysis with the intent of solely investigating the influence of landing parameters on the loading experienced by the UAV during landing, no absolute values of stress or strain were noted. Normalizing all results enabled a straight-forward presentation which was easily interpreted.

Pitch angle θ , and descend velocity V_z were the parameters of main concern. Thus, two independent test cases were defined. For the first, the pitch angle was varied between zero and ten degrees while descend velocity and approach velocity were kept constant at 5 [m/s] and 11.11 [m/s] (40 [km/h]) respectively. As the UAV fuselage has its largest cross section relatively close to the nose with a steadily decreasing cross-sectional area from there until the aft section, it was assumed that the most favorable loading conditions would occur for a pitch angle greater than zero. This assumption was made due to the increase in area of contact between the fuselage and the ground, thereby decreasing the surface load, for pitch angles larger than zero. In Figure 3.1, a comparison of $\theta = 0$ deg and $\theta = 5$ deg is depicted.

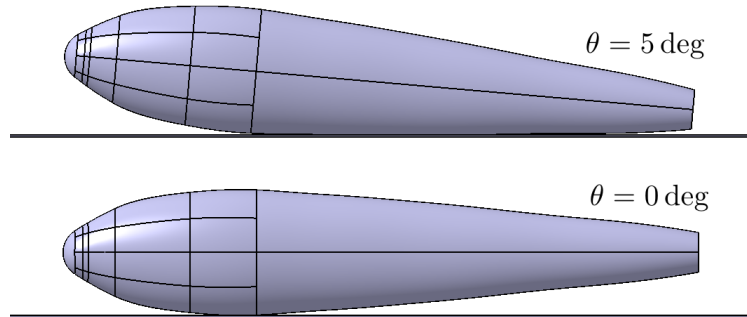


Figure 3.1: *Difference in landing surface area for pitch values of $\theta = 0$ deg (bottom) and $\theta = 5$ deg (top).*

For the descend velocity tests, the pitch angle and approach velocity were held constant at $\theta = 0$ deg and

$V_x = 11.11 [m/s]$ respectively while the descend velocity varied between $V_z = 2.5 [m/s]$ and $V_z = 10 [m/s]$. From the UAV's point of view, a low descend velocity as possible is desirable to reduce the impact load. Experienced operators manually controlling the UAV during landing should be able to facilitate a smooth landing. However, unfavorable landing conditions such as wind, gusts, turbulence, difficult approach path, and a short landing strip are all factors which could result in a hard landing.

3.2 Design of Skin and Internal Structure

Using product development methodology, a proposed skin and internal structure were developed. Concept development was followed by designing of the chosen concepts using the Computer Aided Design (CAD) software Catia V5R20.

3.2.1 Concept Development

Functional Analysis

A functional analysis was performed to identify critical functions of the UAV's fuselage as well as their possible solutions. Specifically, a function tree model was utilized, which resembles but differs from the Concept Classification Tree proposed by Ulrich & Eppinger (2012) in the way that it addresses the main function, means to fulfill said function, functions related to said means and so on until a desired level of specification has been reached, instead of focusing on the main function followed by means only. As suggested by Almefelt (2011), all functions were defined using a *verb* and a *noun*, specifying *what* should be done to *which* part of the UAV.

Morphological Matrix

From the Functional Analysis, key functions, along with their related means, were transferred to a morphological matrix for concept synthesis. Concepts were built up by the partial solutions (means) identified in the Functional Analysis. Throughout the process, focus was placed on identifying possible synergy between partial solutions. The morphological matrix was of the form suggested by Almefelt (2011), with the main functions listed in the first column with the corresponding proposed solutions placed horizontally to the right in columns 2–?, depending on how many different solutions were proposed. The question mark is used to represent the varying number of partial solutions assigned to each function. Starting from the top, moving down, one partial solution was chosen for each function, resulting in a concept proposal. See Chapter 4 for the resulting Morphological matrix and the partial solutions related to each key function.

Concept Evaluation

Results from the concept synthesis were subjected to evaluation with the intent of focusing further development on promising concepts and removing potential dead-ends. Instead of applying well-known methods such as the evaluation matrix proposed by Pugh (1990), a review involving experienced professionals at KDS was conducted. This limitation to applied concept evaluation methodology was done partly due to geographical constraints (Gothenburg in Sweden, Kongsberg in Norway), and partly due to the author being the only student invested in this project. Organizing a group event with the time it would take to do so was deemed too costly, in terms of time, relative to the perceived gains. The experience of the KDS employees and their ability to unbiased evaluate feasibility, advantages, and disadvantages regarding the concepts was thought to be sufficient for this evaluation.

3.2.2 Computer Aided Design

Computer Aided Design (CAD) has become an irreplaceable tool for Product Developers, severely shortening development lead times and costs. An array of CAD tools are available for engineers, however, since the LocalHawk UAV was designed using Catia V5R20, and Chalmers Univ. of Technology has licenses for Catia available for students, it was the chosen CAD tool for this thesis work.

Being a spin-off concept of the original second concept (see Chapter 1), rapidly developed in the late stages of the LocalHawk 2012 summer project, concept three's CAD model was not as described as the other concepts. Specifically, all that was CAD-modelled were the surfaces, roughly describing the outer shape of the airframe. Roughly, because joints between wings, fuselage, and tail were not developed, neither were fillets between these

bodies.

Focus was directed towards the fuselage, with the fuselage's bulge being the first area, of two, immediately possible to identify as an area at risk of failure during belly landing. The other area being the joints between the wings and the fuselage which could break due to wing bending at the moment of impact (inertia effects).

One of the identified possible problem areas of the fuselage was the nose section which had a bulky geometry. Concerns about the producibility of the nose geometry were raised and lead to the decision to improve the design of the nose. Using Catia's Generative Surface Design module, the surface model was modified to produce a surface which had a smoother transition from the fuselage's main body to the nose.

After modifications to the existing fuselage model were performed, the design effort moved to modeling of the two proposed concepts for the skin and internal stiffening structure. For the Multiframe concept, a skin thickness of between 1 [mm] and 2 [mm] was recommended by Kristiansen (2013). Describing *outer* dimensions, the fuselage surface defined in Catia had an offset surface created in the inwards direction. The offset was set equal to the target skin thickness for the concept in question, so that thickness could be applied in the FE model in the outwards direction. By ensuring the skin surface was in contact with the frames, prior to applying thickness to the surfaces, mesh connectivity was possible during the FE modelling.

For the sandwich concept, the frames were a bit more complexly modelled. Instead of several transverse frames, the sandwich concept relied on only two, larger frames, separately supporting the batteries and the payload, see Chapter 4 for the resulting CAD models.

3.3 Material Selection and Parameters

This section covers the work done to select materials for the different structures. It is divided into two sections; section 3.3.1 Composite Skin, and section 3.3.2 Internal Stiffening Structure. Section 3.3.1 describes the process of selecting composite material for the fuselage skin, but also gives an introduction to orthotropic material parameters and how they are defined for the FEA (see section 3.4 for more info about FEA).

Section 3.3.2 briefly discusses limitations regarding the representation of internal components, and contains a brief discussion about the topic of designing internal stiffening structure.

3.3.1 Composite Skin

As described in the Literature Review (Chapter 2), laminates are built up by plies with specific fiber orientations. The result is an orthotropic material, meaning that the parameters of the material (strength, stiffness etc.) depends on the direction, and that the material consists of three orthogonal symmetry planes (Sundström 2007). As opposed to isotropic materials which only requires a general Young's modulus E and Poisson's ratio ν (alternatively Bulk modulus K , or Shear modulus G) to describe elastic behavior, orthotropic materials require Young modulus, Poisson's ratio, and Shear modulus defined in each principal direction or material plane. The constitutive equation for orthotropic materials is (Sundström 2007):

$$\boldsymbol{\varepsilon} = \mathbf{S}\boldsymbol{\sigma} \quad (3.1)$$

Where $\boldsymbol{\varepsilon}$ is the strain vector, \mathbf{S} is the laminate's compliance matrix, and $\boldsymbol{\sigma}$ is the stress vector. Equation (3.1) written out becomes:

$$\begin{Bmatrix} \varepsilon_{11} \\ \varepsilon_{22} \\ \varepsilon_{33} \\ 2\varepsilon_{23} \\ 2\varepsilon_{31} \\ 2\varepsilon_{12} \end{Bmatrix} = \begin{bmatrix} \frac{1}{E_{11}} & -\frac{\nu_{21}}{E_{22}} & -\frac{\nu_{31}}{E_{33}} & 0 & 0 & 0 \\ -\frac{\nu_{12}}{E_{11}} & \frac{1}{E_{22}} & -\frac{\nu_{32}}{E_{33}} & 0 & 0 & 0 \\ -\frac{\nu_{13}}{E_{11}} & -\frac{\nu_{23}}{E_{22}} & \frac{1}{E_{33}} & 0 & 0 & 0 \\ 0 & 0 & 0 & \frac{1}{G_{23}} & 0 & 0 \\ 0 & 0 & 0 & 0 & \frac{1}{G_{31}} & 0 \\ 0 & 0 & 0 & 0 & 0 & \frac{1}{G_{12}} \end{bmatrix} \begin{Bmatrix} \sigma_{11} \\ \sigma_{22} \\ \sigma_{33} \\ \sigma_{23} \\ \sigma_{31} \\ \sigma_{12} \end{Bmatrix} \quad (3.2)$$

From equation (3.2), it is possible to conclude that 12 constants are required to define an orthotropic material. However, a relationship between some of the constants exists (Sundström 2007):

$$\frac{\nu_{12}}{E_{11}} = \frac{\nu_{21}}{E_{22}} \quad (3.3)$$

$$\frac{\nu_{31}}{E_{33}} = \frac{\nu_{13}}{E_{11}} \quad (3.4)$$

$$\frac{\nu_{32}}{E_{33}} = \frac{\nu_{23}}{E_{22}} \quad (3.5)$$

Thereby reducing the total number of independent constants to 9 for an orthotropic material. Equation (3.1) can be written on a stiffness form by inverting the compliance matrix:

$$\boldsymbol{\sigma} = \mathbf{C}\boldsymbol{\varepsilon} \quad (3.6)$$

Where \mathbf{C} is the material stiffness matrix:

$$\mathbf{C} = \mathbf{S}^{-1} \quad (3.7)$$

The material constants are determined from various physical tests which requires different test fixtures/jigs, and several runs to establish values that can be trusted from a statistically point of view. Instead of manufacturing and testing a material, professional manufacturers were contacted and inquired about material data for applicable materials. In accordance with desires put forth by KDS, to facilitate the production process by simplifying composite production wherever possible, prepreg materials were the main focus (see the Literature Review, Chapter 2, for more info about prepreps). Prepreg materials were considered an effective solution because of not having to impregnate a matrix with fibers. To reduce costs, fiberglass prepreps were preferred over carbon-fiber prepreps.

Ideally, a material used in an explicit analysis is defined elastically, plastically, and with failure criteria. Generally, for composite materials, a linear material model with failure includes the parameters presented in equation (3.2), as well as strength parameters (stress/strain limits) accompanied by a failure criterion. For laminates (plate theory), the necessary elastic parameters are reduced to the Young's Modulus E and Poisson's ratio ν in the 11 and 22 directions, as well as the in-plane shear modulus G_{12} (Sundström 2007). The properties of the selected composite material is presented in Table 3.3, Section 3.4.1.

Tsai-Wu Failure Criterion

The failure criterion proposed by Tsai & Wu (1971), is commonly used to predict failure of composite materials. Their model assumes that there exists a failure surface in the stress-space on the following form:

$$f(\sigma_k) = F_i\sigma_i + F_{ij}\sigma_i\sigma_j = 1 \quad (3.8)$$

Where repeated indices indicate summation, and $i, j, k = 1, 2, \dots, 6$. Expanded, eq. (3.8) becomes:

$$\begin{aligned} & F_1\sigma_1 + F_2\sigma_2 + F_3\sigma_3 + F_4\sigma_4 + F_5\sigma_5 + F_6\sigma_6 \\ & + F_{11}\sigma_1^2 + 2F_{12}\sigma_1\sigma_2 + 2F_{13}\sigma_1\sigma_3 + 2F_{14}\sigma_1\sigma_4 + 2F_{15}\sigma_1\sigma_5 + 2F_{16}\sigma_1\sigma_6 \\ & + F_{22}\sigma_2^2 + 2F_{23}\sigma_2\sigma_3 + 2F_{24}\sigma_2\sigma_4 + 2F_{25}\sigma_2\sigma_5 + 2F_{26}\sigma_2\sigma_6 \\ & + F_{33}\sigma_3^2 + 2F_{34}\sigma_3\sigma_4 + 2F_{35}\sigma_3\sigma_5 + 2F_{36}\sigma_3\sigma_6 \\ & + F_{44}\sigma_4^2 + 2F_{45}\sigma_4\sigma_5 + 2F_{46}\sigma_4\sigma_6 \\ & + F_{55}\sigma_5^2 + 2F_{56}\sigma_5\sigma_6 \\ & + F_{66}\sigma_6^2 = 1 \end{aligned} \quad (3.9)$$

For a 3D shell element of a orthotropic material, plane stress, eq. (3.8) is reduced to (Liu & Tsai 1998) & (Ansys 2012):

$$F_{11}\sigma_1^2 + F_{22}\sigma_2^2 + F_{66}\tau_{12}^2 + F_1\sigma_1 + F_2\sigma_2 + 2F_{12}^*\sqrt{F_{11}F_{22}}\sigma_1\sigma_2 = 1 \quad (3.10)$$

Where:

$$F_{11} = \frac{1}{\sigma_{t1}\sigma_{c1}} \quad (3.11)$$

$$F_{22} = \frac{1}{\sigma_{t2}\sigma_{c2}} \quad (3.12)$$

$$F_{66} = \frac{1}{\tau_t^2} \quad (3.13)$$

$$F_1 = \frac{1}{\sigma_{t1}} - \frac{1}{\sigma_{c1}} \quad (3.14)$$

$$F_2 = \frac{1}{\sigma_{t2}} - \frac{1}{\sigma_{c2}} \quad (3.15)$$

In equations (3.11) through (3.15), σ_{ti} indicates the material's tensile strength in the i direction, σ_{ci} indicates the material's compressive strength in the i direction, and τ_t is the in-plane shear strength of the material. The coupling parameter F_{12}^* is often decided by the user to fit the failure surface to experimental results (biaxial stress tests), but to ensure a closed failure-surface envelope, the following requirement exists (Liu & Tsai 1998):

$$-1 \leq F_{12}^* \leq 1 \quad (3.16)$$

However, according to Liu & Tsai (1998), F_{12}^* could be set to an average value of $-1/2$, which they refer to as the generalized von-Mises model.

Ansys Workbench uses "Tsai-Wu Constants" in combination with "Orthotropic Stress Limit" to model this plane stress failure criterion (Ansys 2012). The coupling parameter is replaced with C_{xy} (or C_{12}) which is twice the F_{12}^* value (ANSYS.NET 2002). For Explicit Dynamics analyses in Ansys, the Tsai-Wu constant, C_{xy} , is automatically set to -1 , no matter what the user has defined (Ansys 2012). Since C_{xy} is set to -1 automatically by Ansys Workbench, any Explicit Dynamics analyses employ the generalized von-Mises model for F_{12}^* .

First-Ply Failure (FPF) is the easiest and most conservative approach to modeling the failure of laminate structures. As the name suggests, the composite is considered to be failed when the first ply of the laminate experiences failure. Tolson & Zabarar (1991) describes FPF as occurring when "initial failure of a single layer in a laminate fails in either the fiber direction or in the direction perpendicular to the fibers". On the other end of the scale, is Last-Ply Failure (LPF). Last-ply failure evaluates the failure of all plies and includes a material model for estimating stiffness based on the parameters and stackup of remaining plies. LPF is defined by Tolson & Zabarar (1991) to occur when the structure has degraded to a point where it no longer can support any additional load.

Orthotropic Constants Study

Unfortunately, none of the manufacturers contacted about material data offered the full set of nine elastic constants required to describe orthotropic elasticity in Ansys. Therefore, a short study was performed to investigate how the different unknown parameters affected the solution of a thin composite plate structure being hit by a spherical impactor.

The plate was modelled as a curved surface and meshed using shell elements, see Appendix D for more information about the test setup. Five plies of one of the woven prepreg materials supplied by a manufacturer with a stacking sequence of $[0, 45, 0, 45, 0]$ comprised the composite material, see Table 3.3, Section 3.4.1 for material parameters. The spherical impactor was modelled as a rigid body made up of structural steel, and assigned an impact velocity of $7.5 [m/s]$.

Elastic constants not supplied included the through-thickness Young's modulus, E_z or E_{33} , and out-of-plane Poisson's ratios ν_{yz} or ν_{23} and ν_{xz} or ν_{13} . Values were assigned to each of these constants, creating a reference result. Assigned values were relatively low "guesstimates", the Poisson's ratios were set to 0.001 and the through-thickness Young's modulus was set to $1 [MPa]$. Values of 0.001 were chosen for the Poisson's ratios instead of 0 because, according to Lauth (2013), an inserted value of 0 for Poisson's ratio will automatically be changed to 0.3 by Ansys. Several tests were performed, varying each constant independently as well as combined tests where all constants were given a high value. See Table 3.1 for test cases.

Table 3.1: Test settings for the Orthotropic Constants Study

Test	E_z [GPa]	ν_{yz}	ν_{xz}
1	0.001	0.001	0.001
2	10	0.001	0.001
3	10	0.1	0.001
4	10	0.1	0.1
5	20	0.1	0.1
6	20	0.499	0.1
7	20	0.499	0.499
8	0.001	0.499	0.499
9	0.001	0.001	0.499
10	10	0.122	0.122

3.3.2 Internal Stiffening Structure

The internal stiffening structure supports the payload, batteries, and engine. Being relatively small additions, mass wise, the camera and engine were not included in this project. This simplification was done to avoid spending time on designing detailed fixtures for these, more complex, installations. These are more complex because, it should be possible to install the camera in different angles with a free view of the ground, and the engine represents a source of elevated temperatures requiring cooling.

Since the main goal of this thesis was to investigate the belly-landing concept, resource spending (time) on design of internal stiffening structures was limited to the structure supporting the payload (electric cabinet) and the batteries. Therefore, only frames for those two components were modeled (except for the Multiframe concept which also had frames not connected to the internal components). The number of frames was a result of a discussion between the stakeholders at KDS and the author of this thesis. Operating with the mindset that internal access to the UAV's components should be available through cut-outs in the top of the UAV, all frames were designed so that internal components could be lowered into them, and not inserted from the front/side/rear/bottom.

3.4 Finite Element Analysis

CAD-files generated during the CAD phase were imported into the FEA software Ansys as STEP (.stp) files. STEP (Standard for the Exchange of Product Model Data, ISO 10303) is a neutral file format for transfer of CAD/CAM/CAE geometry and product data between different systems (SCRA 2006). For a more thorough explanation of functions and controllers used in Ansys, see Appendix A. In Appendix B, a sample case for an explicit analysis is solved step by step.

Since it being a significant contribution to the thesis text, the Pre-Processing work has been divided up into several sections. The term Pre-Processing encompasses all of the work done to enable the FE Analysis to run and achieve realistic, sound results. It is the most input demanding part of the FEA and involves defining material, body contacts, mesh, boundary conditions (BC) such as loads and supports, analysis settings, and any modifications to the geometry.

Last-minute access was granted to Ansys ACP Composite PrepPost v14.0. This module was used to model the composite laminates in Ansys. Unfortunately, since it was version 14.0 and not 14.5, post-processing of Explicit Dynamics' results using ACP was not available. The ACP pre-processing modeling environment consists of four components; Engineering Data (material definition), Geometry (import of CAD geometry or modeling geometry using Design Modeler), Model (meshing, boundary conditions, and analysis settings), and Setup (composite modeling). These are then linked to one or more analysis systems (here: Explicit Dynamics), and the composite information is automatically imported as a Layered Section, see Figure 3.2 for an overview from Ansys Workbench.

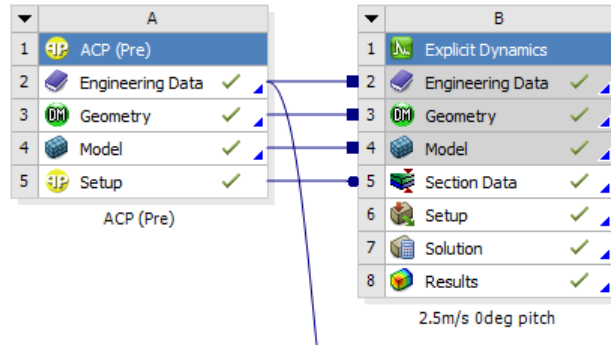


Figure 3.2: *ACP (pre) linked to Explicit Dynamics in Ansys Workbench*

Another limitation affiliated with version 14.0 is the restriction of not being able to do explicit analyses of models with meshes consisting of both shell elements and solid elements. Although possible for other types of analyses, the Explicit Analysis system in Ansys Workbench cannot have a combined model input from an ACP (pre) system (shell elements) and a Model system (solid elements). Due to this limitation, all bodies were simplified using surfaces which were then imported into ACP (pre) and applied thickness.

3.4.1 Material Definition and Geometry Preparation

Utilizing input received from Gurit, RE210 SE70 unbalanced, woven fiberglass prepreg was chosen as the skin material. SE 70 was chosen for its toughness and availability in light-weight reinforcements, suitable for UAV structures in the LocalHawk's size range (Armstrong 2013). Based on the input, orthotropic elasticity as well as orthotropic strength could be modeled for composite shell elements (that is, the elastic constants provided by Gurit were complemented by the parameters decided using the results of the Orthotropic Constants Study, section 3.3.1, results are in Chapter 4). As described in section 3.3.1, the Tsai-Wu failure criterion was used to determine whether or not a ply had failed. Upon failure, the AUTODYN solver (for explicit analyses) in Ansys removes the element's capability to sustain any shear stresses or negative pressures (Ansys 2011). In Ansys, the composite material definition was achieved by applying the material parameters specified in Table 3.2. Please note that the densities presented in Tables 3.2 through 3.4, were not the densities used in the final analyses, they are the actual densities, pre-modification. Densities had to be modified so that the total weight

of the wing-less models represented actual condition, section 3.4.5 explains this in more detail.

Table 3.2: Material parameters composite skin

RE210 SE70 Unbalanced Woven E-Glass Prepreg		
Property/Parameter	Value/Setting	Unit
Density	1867	$\left[\frac{kg}{m^3}\right]$
Ply Type	Woven	$[-]$
Orthotropic Elasticity		
Young's Modulus x -dir	27180	$[MPa]$
Young's Modulus y -dir	18120	$[MPa]$
Young's Modulus z -dir	10000	$[MPa]$
Poisson's Ratio xy	0.122	$[-]$
Poisson's Ratio yz	0.122	$[-]$
Poisson's Ratio xz	0.122	$[-]$
Shear Modulus xy	3806	$[MPa]$
Shear Modulus yz	3460	$[MPa]$
Shear Modulus xz	3460	$[MPa]$
Orthotropic Stress Limits		
Tensile Strength x -dir	407.7	$[MPa]$
Tensile Strength y -dir	271.8	$[MPa]$
Tensile Strength z -dir	0	$[MPa]$
Compressive Strength x -dir	366.9	$[MPa]$
Compressive Strength y -dir	244.6	$[MPa]$
Compressive Strength z -dir	0	$[MPa]$
Shear strength xy	41.5	$[MPa]$
Shear strength yz	0	$[MPa]$
Shear strength xz	0	$[MPa]$
Tsai-Wu Constants		
Coupling xy	-1	$[-]$
Coupling yz	-1	$[-]$
Coupling xz	-1	$[-]$

Non-Composite Material Definition

Table 3.3 contains the material parameters for the material selected to represent the internal stiffening components (frames). This material was selected due to its light weight and excellent damping capabilities (Rohacell 2013).

Table 3.3: Material parameters foam frames

Rohacell 110IG		
Property/Parameter	Value/Setting	Unit
Density	110	$\left[\frac{kg}{m^3}\right]$
Ply Type	Isotropic Homogenous Core	$[-]$
Isotropic Elasticity		
Young's Modulus	160	$[MPa]$
Poisson's Ratio (Calc)	0.33	$[-]$
Shear Modulus	60	$[MPa]$
Bulk Modulus (Calc)	160	$[MPa]$

For the rigid bodies, aluminum as described in Ansys' material library was used. Table 3.4 presents the material parameters for the rigid bodies (ground, payload, and batteries).

Table 3.4: Material parameters rigid bodies

Aluminum		
Property/Parameter	Value/Setting	Unit
Density	2770	$\frac{kg}{m^3}$
Ply Type	Isotropic	$[-]$
Isotropic Elasticity		
Young's Modulus	71000	$[MPa]$
Poisson's Ratio	0.33	$[-]$
Bulk Modulus (Calc)	69608	$[MPa]$
Shear Modulus (Calc)	26692	$[MPa]$

Please note that material definition for the frames, payload, batteries, and ground were rudimentary due to them not being scrutinized. Material data for the frames were collected from the website of Rohacell (2013), however, the shear modulus was modified to get a Poisson's ratio $\nu < 0.5$.

Geometry Preparation

Due to unsuccessful attempts to combine solid geometry (from a Mechanical Model system) and surface geometry (from the ACP (pre) system) in an Explicit Dynamics system, all bodies were simplified, and represented by surfaces. However, since no detailed representations of neither the payload nor the internal components were included in the original CAD import, it could be argued that this simplification did not affect the results in a significant manner. To accommodate meshing and solve issues related to relative-to-the-skin frame/payload movement, the skin, payload, batteries and the frames were combined into a multi-body part. Line/edge to surface contact definition is not supported for Ansys' Explicit Dynamics system, and surface to surface contact definitions between the frames and the skin were not enough for the frames to maintain their position relative to the skin.

As described in section 3.2.2, the frames for the Sandwich concept were more complex than the frames for the Multiframe concept. This complexity hindered accurate representation of the geometry of the frames. However, since the main focus was on the response of the skin to the impact with the ground, this reduced accuracy in frame representation was considered of little importance and thus an acceptable approximation. The resulting simplification using surfaces is compared to the original geometry in Figure 3.3.

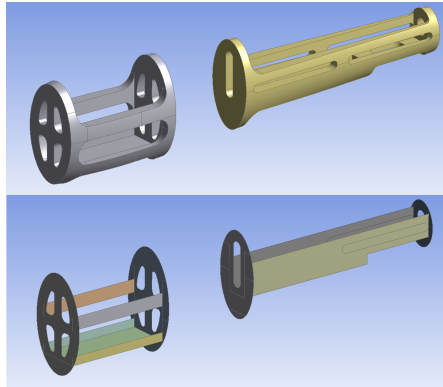


Figure 3.3: *The Sandwich Skin concept's frames. Top: Before simplification. Bottom: After being simplified using surfaces*

3.4.2 Meshing

To avoid non-physical results due to movement of frames/payload/batteries relative to the fuselage's skin, all moving bodies were combined into a multi-body part. This was combined with a *Joint* description between the frames and the skin, creating common boundary edges to fully ensure mesh connectivity. Figure 3.4 depicts the connected mesh between the aft closing section and the skin, although being surface bodies, thickness is displayed to visualize relative size and distance.

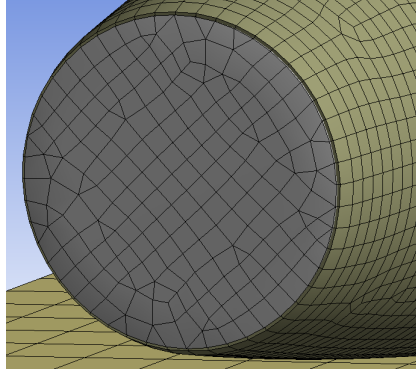


Figure 3.4: *Meshes for the aft section and skin connected*

It is also important to stress that since the meshing took place inside an ACP (pre) system, physics preference for the meshing algorithm was, manually, set to *Explicit* (since it was not set by default, as it would have been inside an Explicit Dynamics system). See Appendix A for a more in-depth explanation of what Explicit meshing preferences represent.

Sizing was globally controlled using the global sizing controller defined under *Mesh-Sizing-Min Size* and *Max Face Size*, these were set to 2.5 [mm] and 20 [mm] respectively. A result of trial and error, the part-specific method and sizing settings can be seen in Table 3.5 for both the Sandwich Skin concept and the Multiframe concept.

Table 3.5: Mesh method, sizing, and sequence for each part

Part	Method	Sizing [mm]	Sequence
Multiframe Concept			
Skin	Quadrilateral Dominant	5 hard	3
Frame 1-9	Uniform Quad/Tri	5	4
Aft Section	Uniform Quad/Tri	5	5
Payload	Mapped Face Meshing	10 soft	1
Batteries	Mapped Face Meshing	10 soft	2
Ground	Mapped Face Meshing	15 soft	6
Sandwich Skin Concept			
Skin	Quad. Dominant (All quad)	5 hard	1
Payload Frame	Uniform Quad/Tri	10	2
Batteries Frame	Uniform Quad/Tri	10	4
Payload	Mapped Face Meshing	10 soft	3
Batteries	Mapped Face Meshing	10 soft	5
Ground	Mapped Face Meshing	15 soft	7
Aft Section	Uniform Quad/Tri	5	6

Not directly a part of the meshing, creating named selections was the last step performed prior to opening the model in the ACP (pre) environment. When importing a mesh into the ACP (pre) environment, the mesh is imported as one entity, no matter if the meshed bodies are connected or not. Therefore, it is necessary to

define the elements and nodes which make out parts of the mesh that needs to be distinguished from the other elements and nodes. Named selections created in the Mechanical (meshing) environment are imported into ACP (pre) and allows the user to separate the bodies from each other. All bodies were assigned a named selection, and in addition, lines going from the nose of the fuselage to the aft section were also assigned a named selection each. These lines were used to define the principal direction for the plies in the ACP (pre) system.

3.4.3 Composite Modeling using ANSYS ACP Composite PrepPost

Using the ACP (pre) system instead of the Layered Section option which is native in Ansys Mechanical, allowed for much better control and easier definition of plies and their respective orientation. After importing the surface mesh and named selections described in section 3.4.2, fabrics were defined using the materials presented in section 3.4.1. Although consisting of isotropic materials, the frames, payload, batteries, and ground were modeled using plies defined in the same way as orthotropic laminates due to the aforementioned limitation associated with v14.0 of not being able to combine solid and shell elements. However, since these bodies consisted of isotropic materials, rosette (coordinate systems, rosettes are used to describe reference directions in ACP) definition was arbitrary for all of these bodies.

Orientation Direction, defined during creation of Oriented Element Sets, determines the stacking direction for a laminate/composite structure, and was in that way used to determine in which direction thickness was applied to a surface mesh. For surfaces that were a result of a mid-surface simplification, as opposed to surfaces created from a face or created in CAD to be an external face, two Oriented Element Sets were created, one for each direction to apply thickness. Reference fiber direction (0 deg direction) for the skin was defined using the imported Edge Sets (from named selections consisting of edges) to be along the skin, from front to aft. An example of the resulting reference direction and fiber directions are shown for two plies, $[45, -45]$, of the skin of the Multiframe concept in Figure 3.5.

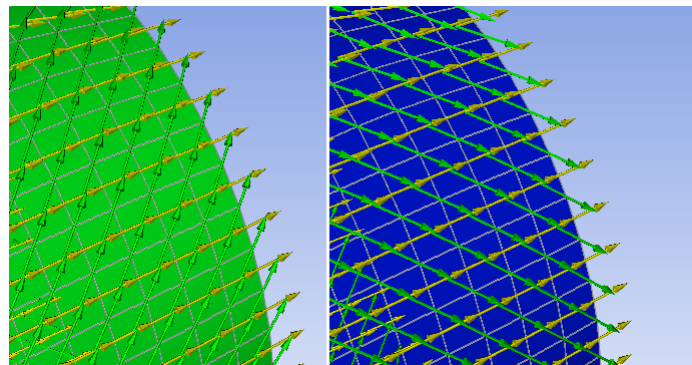


Figure 3.5: *Reference direction (yellow) and fiber direction (green) for the two plies $[45, -45]$ (left, right), rear of the skin*

The complete process is described in more detail in Appendix C, where a step-by-step guide is presented for the Sandwich Skin.

3.4.4 Common Boundary Conditions and Analysis Settings

In all cases, the ground was applied a fixed support, locking all degrees of freedom. Moving parts (skin, frames, payload, and batteries) were assigned the same velocity whose directional components were defined using a coordinate system which was normal to the ground. By defining the direction of the velocity vector using a relative-to-the ground coordinate system, it was assured that all tests had the same velocity relative to the ground (except for those where descend velocity varied). A standard earth gravity was applied to all bodies, this also being defined by the ground coordinate system.

Utilizing Ansys' advice on settings for low-velocity impact simulations, the analysis settings presented in Table 3.6 were used, see Ansys (2011). As will be described in section 3.4.7, mass scaling was applied to shorten the solution time by increasing the time step (Appendix A explains the theory behind mass scaling in more

detail). To facilitate the use of mass scaling, mass after meshing never exceeded 12.49 [kg], since mass scaling would add a fractional mass.

Table 3.6: Analysis Settings

Setting	Value
Mass Scaling	Yes
Precision	Double
Beam time step safety factor	0.1
Hex integration	1pt Gauss
Shell sublayers	3
Tet integration	Nodal Strain
Hourglass Damping	Flanagan Belytschko
Stiffness coefficient	0.1
Viscous coefficient	0.1
Save results on	100 equally spaced points
Save result tracked data per	10 cycles
Body self contact	No
Element self contact	No

By default, when applying Flanagan-Belytschko hourglass damping, which is based on the paper presented by Flanagan & Belytschko (1981), the viscous coefficient is set to 0. However, localized energy oscillations, see Figure 3.6, led to this being set to 0.1.

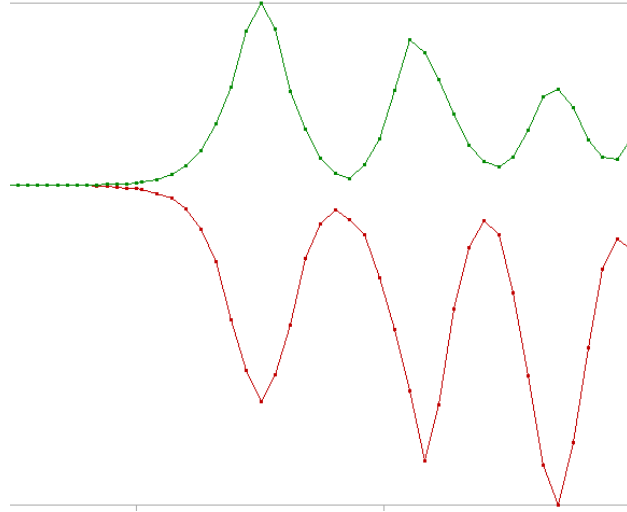


Figure 3.6: *Energy oscillations at late stages of an analysis*

3.4.5 Density Modification and CG Positioning

Tests were performed without any wing or tail geometry due to them not being modeled with internal structure, and to allow for shorter solve times due to the reduced model complexity. As mentioned in Appendix A, correct representation of the bodies' mass is very important due to the dynamic nature of explicit analyses. Therefore, since there were no wings nor a tail included in the model, modifications to the density of existing materials were performed. Had these modifications not been implemented, results would have been invalidated as the analyses had included an unrealistically light-weight structure, grossly underestimating actual loads. Except from the solver time step, see the Literature Review Ch. 2 or Appendix A for explanation why, and of course the mass of the bodies, this density modification was assumed to not affect the solution's accuracy in a noticeable manner. To reach the goal of 12.5 [kg], which was the estimated total weight of the LocalHawk UAV,

the density of all materials were modified with the same constant, thereby ensuring no major offsets in mass distribution. Being a UAV, the center of gravity (CG) is one of the most important parameters used to evaluate stability during flight. Positioning of internal components had been meticulously carried out during design of the three UAV concepts to ensure that the UAVs were stable. Simplifying the model to what was used in this thesis, and using thickness applied to a surface to individually replicate the mass of the payload and batteries, resulted in an offset in the position of the CG. Tuning the thickness values for both the payload surfaces and the surfaces representing the batteries, re-positioned the CG at its outset. The process of modifying density and re-positioning the CG can be visualized with a flow chart shown in Figure 3.7.

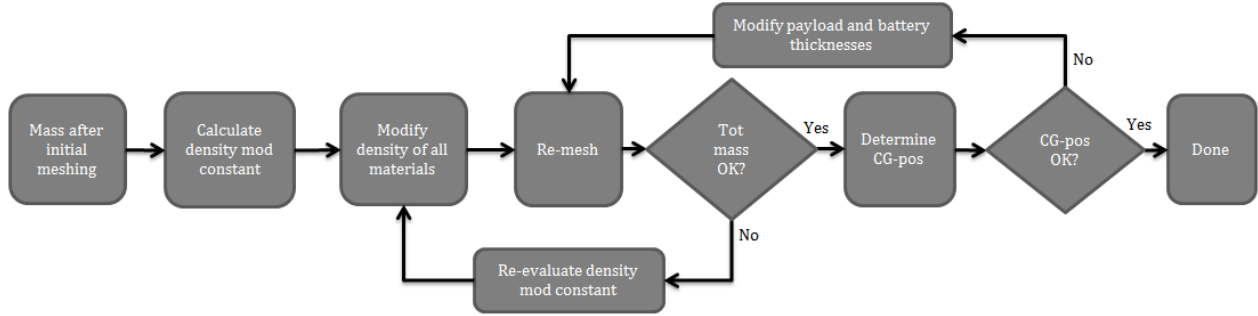


Figure 3.7: Flow chart for density modification and CG-positioning

Resulting density modification constants, CG-positions, and surface thickness can be seen in Table 3.7, for the third UAV concept, the X coordinate of the CG was estimated to 712 [mm].

Table 3.7: Payload/Batteries surface thickness and CG-position for each concept after meshing

Concept/Part	Thickness [mm]	CG-pos (X-dir) [mm]	Density mod. constant
Sandwich Skin		approx. 700 (Catia)	1.39
Payload	4.5	-	-
Batteries	11.7	-	-
Multiframe		711	1.48
Payload	4.5	-	-
Batteries	11.7	-	-

Although the CG position of the Sandwich Skin concept could only be estimated using Catia, due to the skin having a non-uniform density (mix of foam core and composite skin), an offset of 10 [mm] was not considered to invalidate any results. The same thickness for the surfaces representing the payload and batteries was applied to the Sandwich Skin concept as the Multiframe concept based on the assumption that the CG of the skin would not move that much relative to the CG for the Multiframe's skin, and therefore the same thicknesses would be applicable for the Sandwich Skin concept as well.

3.4.6 Test Setup

The tests were divided into three categories, each evaluating a specific variable. Firstly, different stacking sequences were tested to identify a sequence which facilitated the belly landing. This preferred stacking sequence was then used as a basis for the two other sets of tests; pitch angle and descend velocity.

Stacking Sequence

Five different sequences were tested to determine a suitable setting. Although the layers consisted of a woven material, properties in the x and y direction were not the same due to the material being an *unbalanced* woven prepreg. From Table 3.2, it is clear that stiffness and strength in the x direction greatly surpasses that of the stiffness and strength in the y direction. Therefore, a $[45, -45, 45]$ stacking sequence would not have the same

properties as a $[-45, 45, -45]$ stacking sequence, as it would have for a balanced woven material.

Based on the material parameters defined in Table 3.2 and equations (3.10) & (3.13) (Tsai-Wu failure criterion, section 3.3.1), a need for particular reinforcement against shear stresses was identified. An overview of all stacking sequence test settings can be seen in Table 3.8. Starting from the outer layer, each subsequent layer in the stacking sequence was applied inwards, replicating the process of stacking layers inside a mold. In other words, the ply numbers for the stacking sequence was $[1, 2, 3, 4, 5, 6, 7, 8, 9]$, with ply number 1 hitting the ground first. Please note that in Ansys, the surface normal of the skin pointed outwards, making layer #1 actually ply #9, this did not affect the stacking sequence or the results, it was only a matter of keeping the numbers separated and not getting confused. Put in terms of the plies this meant that ply $[1, 2, 3, 4, 5, 6, 7, 8, 9]$ corresponded to layer $[9, 8, 7, 6, 5, 4, 3, 2, 1]$. Besides the common boundary conditions and analysis settings specified in section 3.4.4, pitch angle and descend velocity were kept constant at 0 deg and $2.5 [m/s]$ respectively.

Table 3.8: Test settings; Stacking Sequence Testing

Test #	Stacking Sequence
1	$[0, 45, -45, 45, 0, -45, 45, -45, 0]$
2	$[0, 45, -45, 45, 90, 45, -45, 45, 0]$
3	$[90, 0, 90, 0, 90, 0, 90, 0, 90]$
4	$[45, -45, 45, -45, 45, -45, 45, -45, 45]$
5	$[90, 45, -45, 90, 0, 90, -45, 45, 90]$

Figure 3.8 depicts the project setup in Ansys Workbench.

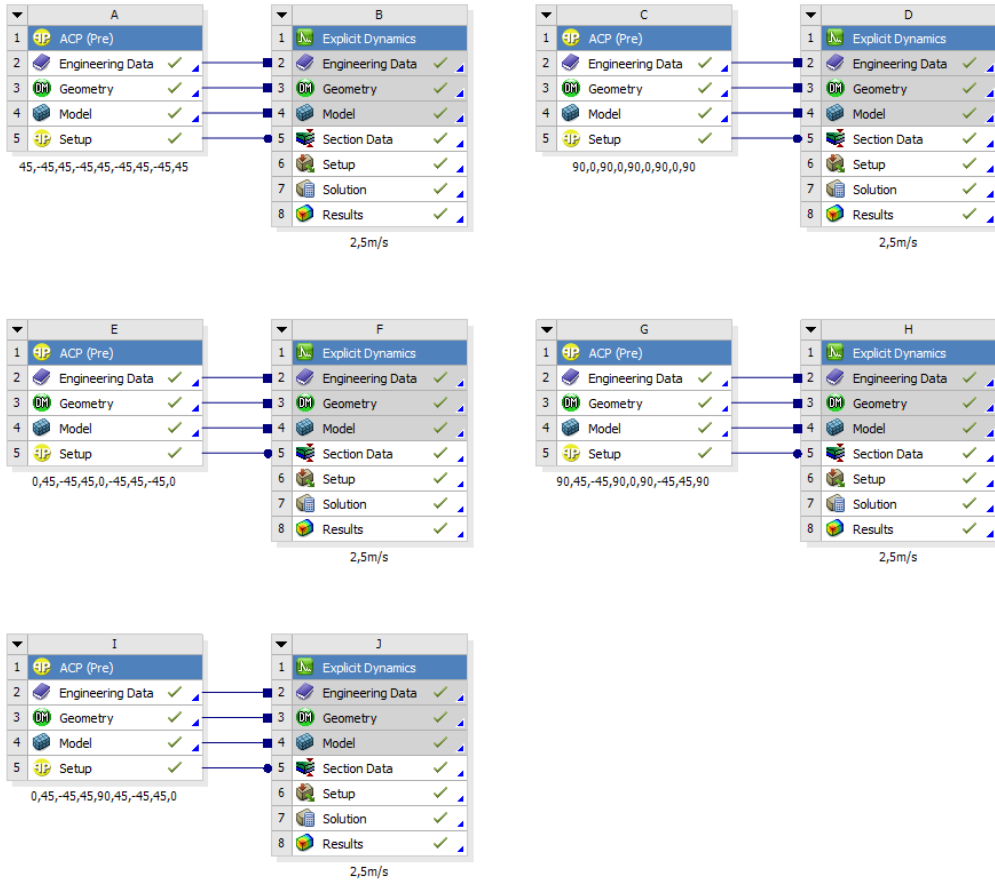


Figure 3.8: *Project setup for stacking sequence testing*

Pitch Angle (θ) and Descend Velocity

Using the results of the landing parameter testing, as well as results from the stacking sequence testing, tests of pitch angles were limited to 0 deg and 6 deg. The primary cause of this, was that the parameter testing showed that at around $\theta = 6$ deg, there was a saddle point with the lowest stresses and strains in the skin. If the UAV would fail at a pitch angle of 6 deg, it was therefore assumed that it would not be able to land at any other pitch values.

From the results of the different stacking sequence tests, it became clear that no higher velocities than 2.5 [m/s] were remotely feasible. Therefore, in addition to 2.5 [m/s], only one test at 1.0 [m/s] was performed. This limitation to only one other descend velocity test was motivated by the notion that if the UAV would not "survive" a landing at 1.0 [m/s], then it would not be operationally viable. Test settings regarding variations in pitch angle and descend velocity is summarized in Table 3.9.

Table 3.9: Pitch angle and descend velocity test settings

Sandwich Skin concept		Multiframe concept	
$\theta = 0$ deg	$\theta = 6$ deg	$\theta = 0$ deg	$\theta = 6$ deg
1 [m/s]	1 [m/s]	1 [m/s]	1 [m/s]
2.5 [m/s]	2.5 [m/s]	2.5 [m/s]	2.5 [m/s]

3.4.7 Post-Processing

Once again, since Ansys version 14.0 was used, post-processing of explicit results in ACP (post) was not available. Therefore, post-processing took place inside the Ansys Mechanical environment. Focusing mainly on the composite skin, most of the results collected gave information about stresses, deformation, or the failure status of the skin. By applying a user-defined result with the expression *STATUS*, failure as defined by a selected failure criterion, here: Tsai-Wu, could be evaluated separately for all plies. Please note that the visualization of this failure criterion was binary; either the material had not failed (blue), or failure according to the specified failure criterion was detected (red).

Before initializing time costly analyses, mass scaling was applied, by setting a desired minimum time step, and total mass added from it evaluated, see Appendix A for more information about mass scaling and its application in Explicit analyses. If an extensive amount of mass had been added to bodies which would be involved in severe negative accelerations, for instance the skin, mass scaling was re-evaluated and subsequently checked. On the other hand, if the body whose mass had been severely increased would not experience any acceleration forces, i.e. the ground, and mass scaling for other bodies were acceptable, then that mass scaling setting was accepted and used for the complete analysis. Please note that the solver was set to not update mass scaling during an analysis, thereby removing any risk of it increasing mass during the solve process.

Both the user-defined result *MASS_SCALE*, and the file **admodel.prt**, which is generated by the AUTODYN solver, were used to evaluate mass scaling. *MASS_SCALE* enables the user to part-wise, and element wise, evaluate the amount of mass added by the solver, from the set minimum time step. Summarizing key properties of materials, settings, energy, and mass scaling, the **admodel.prt** file gives an overview in [mg], as well as in [%], of mass added per part and total for the entire model. Combining these methods gave an insight into where the mass was added, and in some cases also raised awareness of mesh shortcomings in the form of (groups of) elements that kept the solver from operating with a higher time step. The process of applying mass scaling, controlling mass added, and re-evaluating the desired time step can be visualized with the flow chart in Figure 3.9. A "short analysis" was defined as setting the maximum number of cycles to 20, normally resulting in a solve time of approximately half a minute.

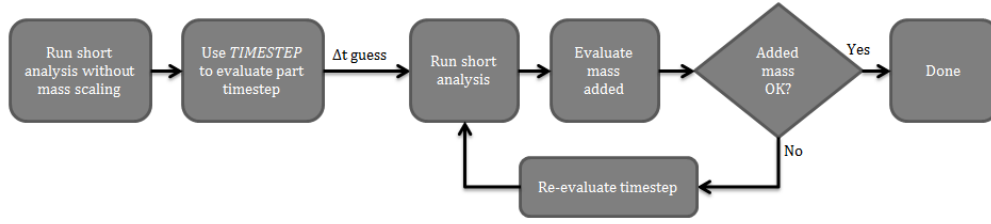


Figure 3.9: *Flow chart for adding and evaluating mass scaling*

After an analysis had completed, energy and momentum was controlled for irregularities. Particularly hourglass energy and the energy error were controlled to evaluate the validity of the solution, see Appendix A for general theory concerning hourglass energy, and how to control it, and Appendix B for a sample case where methods on how to evaluate and control hourglass energy and energy error is included. Means presented in said appendices were utilized to evaluate the model and perform necessary changes, for instance, a mesh refinement from 7.5 [mm] to 5 [mm] for the skin was performed to reduce hourglass energy, which also reduced asymmetry and gave a more uniform mesh (highly desirable when setting up explicit analyses).

Although the *STATUS* expression did not report the failure mode, studying results for principal and shear stresses around the time of failure aided in determining the major contributor to failure.

4 Results

4.1 Landing Parameters Study

Ansys was used to do a landing parameter study. To simplify the analyses, an isotropic material was used (Non-Linear Aluminium from Ansys' library) and all results were normalized relative to a reference case.

4.1.1 Pitch (θ)

The reference case for the *Pitch angle* study was an approach velocity (horizontal) of $V_x = 11.11$ [m/s] (40 [km/h]), pitch angle of $\theta = 0$ deg, and descend velocity of $V_z = 5$ [m/s]. For the rest of the cases, the approach and descend velocities were kept constant at the reference level. Pitch angles varying from zero to ten degrees were tested, thereby assuming the UAV performs a stable landing manoeuvre.

For most of the cases, an analysis time of $t = 1.5$ [ms] was sufficient to include the effects of the first, most severe impact. However, for increased pitch angles ($\theta \geq 7$ deg), the aft section of the fuselage came in contact with the landing surface before the remaining bulk of the fuselage, resulting in an angular acceleration of the fuselage. Initial aft-section contact was therefore followed by a relatively long period of time where the fuselage followed a rigid-body, rotational motion before the "bulge" of the fuselage hit the landing surface. See Figure 4.1 for an illustrative example for the case where the pitch angle is equal to ten degrees. In effect, this rigid-body motion increased the required solve time which limited the number of test cases for angles greater than $\theta = 6$ deg.

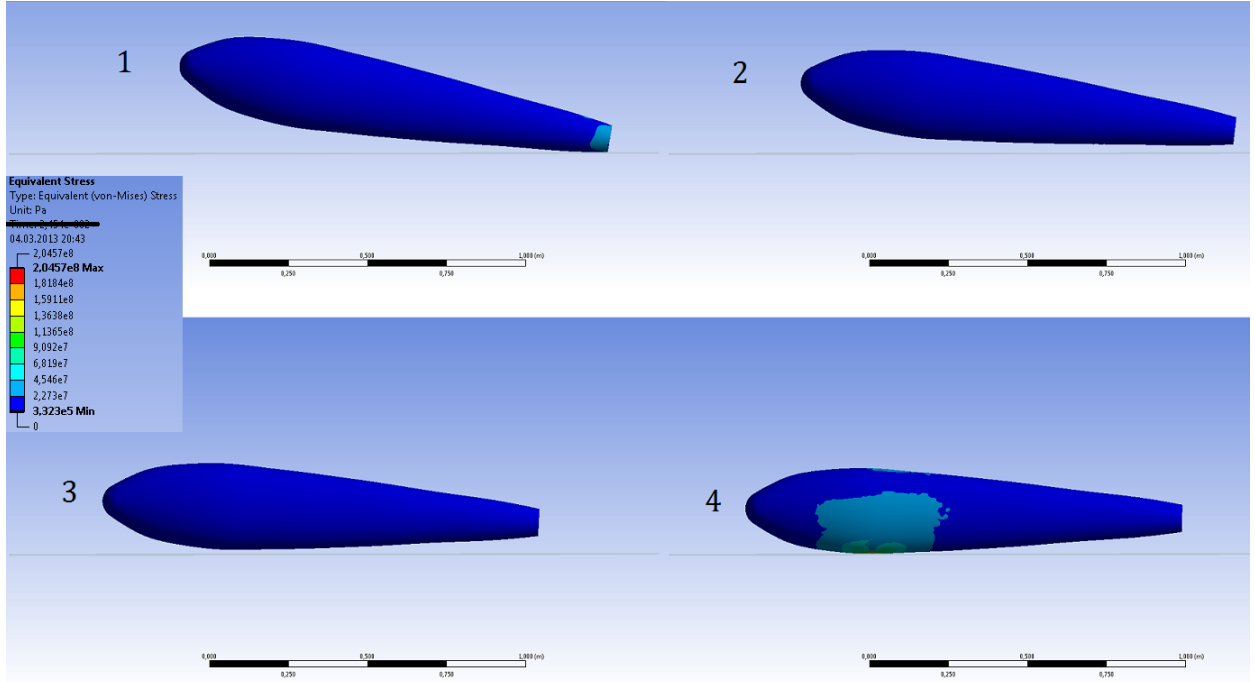


Figure 4.1: 1: Initial contact between the fuselage-aft section and the fuselage section. 2 and 3: The fuselage experiences, approximately, rigid-body rotation. 4: Time of maximum equivalent (von-Mises) stress.

Results for all pitch angle cases can be seen in Figure 4.2. Normalized results for maximum equivalent von-Mises stress is on the left vertical axis, while the normalized results for maximum equivalent plastic strain is on the right vertical axis.

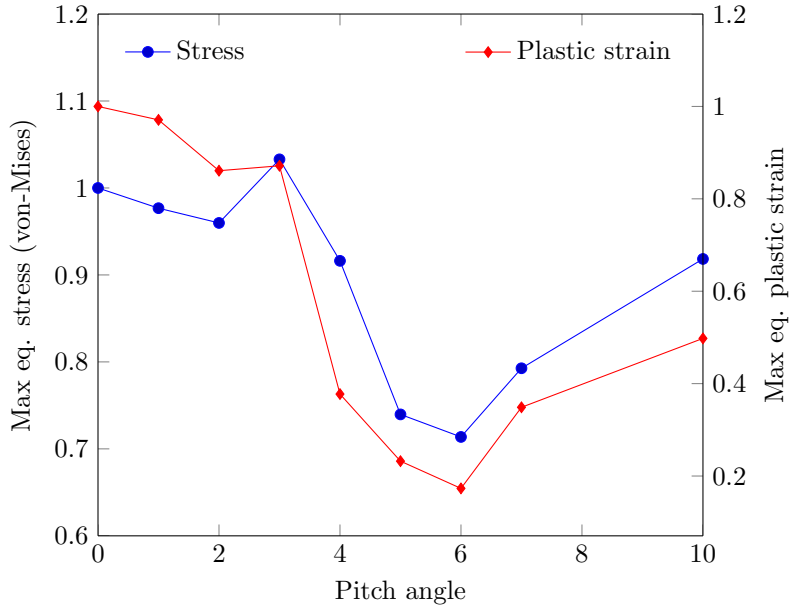


Figure 4.2: *Normalized results, varying pitch angle. Descend velocity: 5 [m/s], approach velocity: 40 [km/h].*

4.1.2 Descend Velocity

As could be expected, stress and strain had a, close to, positive proportional correlation with descend velocity, see Figure 4.3. Stresses increased with 22.6% at 10 [m/s] relative to a descend velocity of 2.5 [m/s]. Maximum plastic strain on the other hand increased almost eight times (7.86) relative to the plastic strain experienced at 2.5 [m/s]. After revising these results, and after discussions with the external supervisor at KDS, it was decided to keep a descend velocity of 2.5 [m/s] as a maximum goal. Later descend velocity tests would therefore be performed at lower velocities.

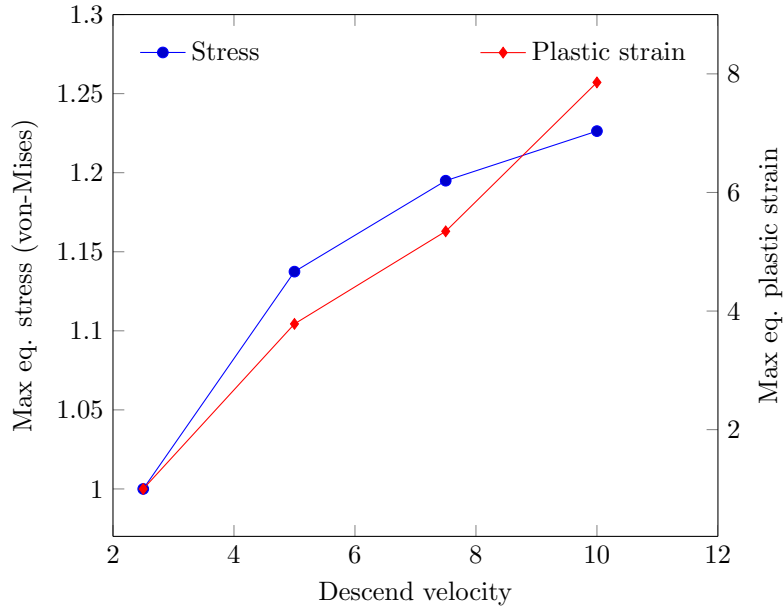


Figure 4.3: *Normalized results, varying descend velocity. Pitch angle 0 deg*

4.2 Design of Skin and Internal Structure

4.2.1 Concept Development

Using the methods described in Chapter 3, different concepts for the UAV fuselage were developed and evaluated. This section presents the results of this concept development and evaluation, starting with the functional analysis.

Functional Analysis

Figure 4.4 depicts the result of the Functional Analysis, visualized here using a mindmap structure.

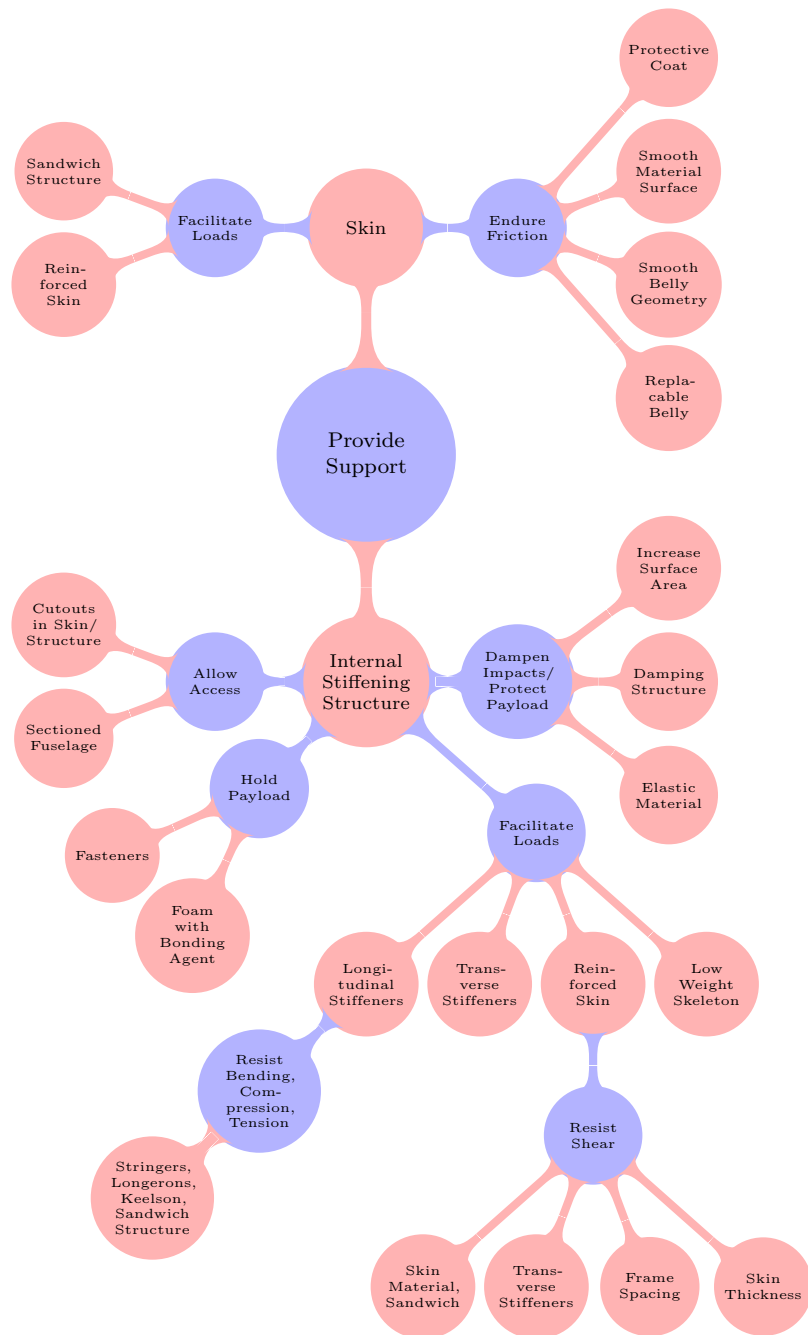


Figure 4.4: *Functional Analysis*

Morphological Matrix

Figure 4.5 depicts the Morphological Matrix used to create the concepts. Four main functions were chosen and can be seen in the left-most column; *Resist Bending*, *Resist Shear*, *Hold Payload*, and *Dampen Impacts/Protect Payload*. The differently colored lines, with symbols, represents concepts and their partial solutions.

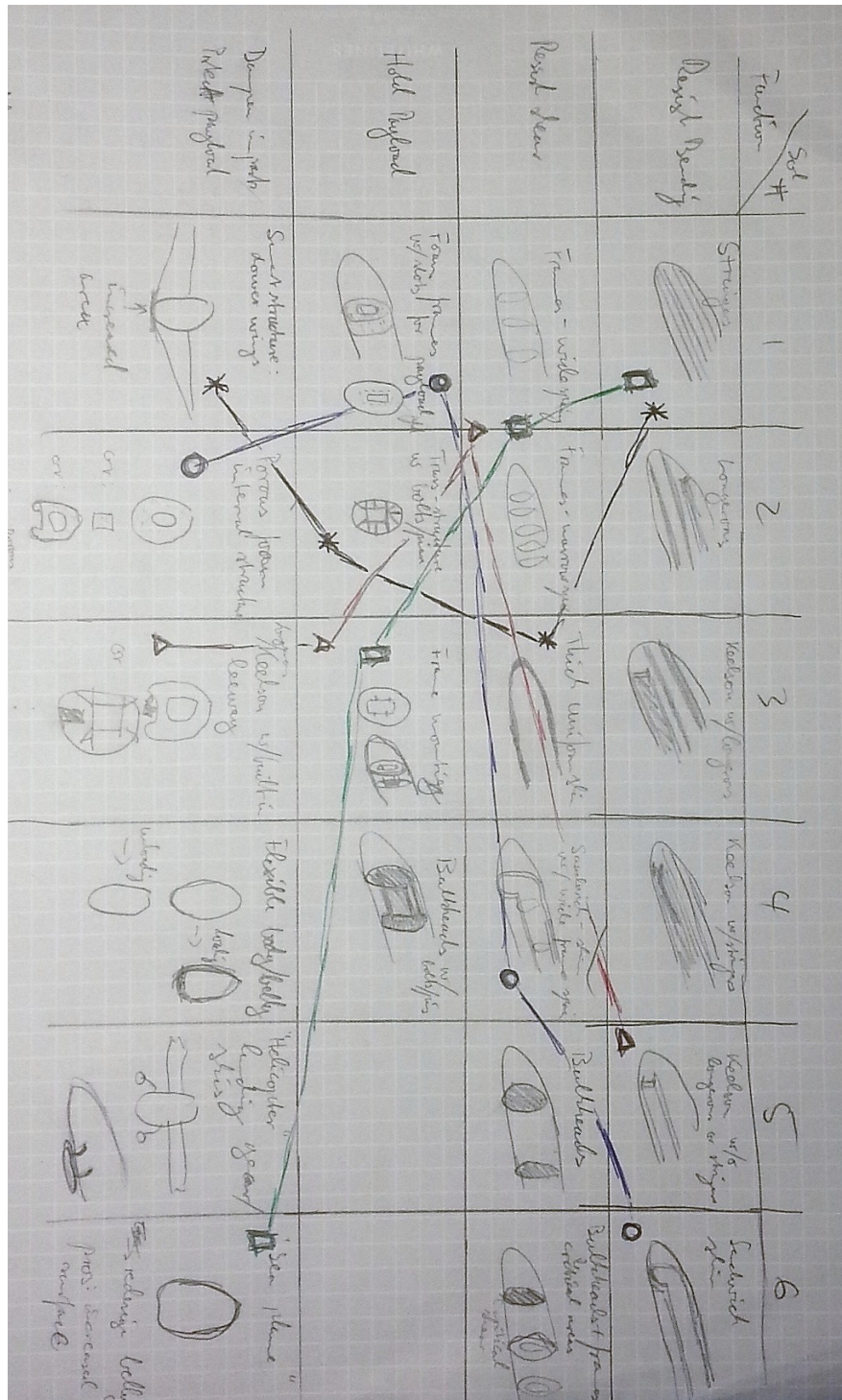


Figure 4.5: Morphological Matrix

Concept Evaluation

In total, four fuselage concepts were proposed which facilitated belly landing. These were the Truss-Stringer, the Sea Plane, the Keelson, and the Sandwich. Concept evaluation consisted of the author first summing up the concepts and their features, as well as a list of assumed pros and cons, before sending the concept proposals to be reviewed by experienced engineers at KDS. Their views were then communicated back over telephone during an evaluation meeting between the external supervisor of this thesis and the author. Discussing the results led to two concepts being chosen to proceed to the impact analyses. The following is a summary of the four fuselage concepts and the result of their evaluation, starting with the Truss-Stringer concept. Rough, hand-drawn sketches are included for each concept.

Longitudinal stringers in combination with trusses to support the payload and batteries were the elements the Truss-Stringer relied on for internal stiffening and support. Aiming for a lightweight, stiff structure, the stringers were imagined being manufactured using a porous foam core clad with prepreg tape to add stiffness. In addition to the internal structure, it was suggested that the Truss-Stringer concept could include lowering the wings to increase the area in contact with the landing surface, thus reducing impact loads. An optional design would involve blending the wings and fuselage to an even greater extent, resulting in a flying wing UAV concept. Assumed pros of the Truss-Stringer concept included a reduced landing contact force due to the increased landing surface area, a low empty-weight of the fuselage, and increased stability during skidding due to the lowered wings. However, the assumed cons were quite significant; added material for the transition between wings and the fuselage could result in a increase in weight for the airframe, the truss structure would introduce concentrated loads, which combines poorly with composite materials, the larger transition areas between the wings and the body could decrease lift, resulting in a need for increased wing surface, adding even more weight to the airframe. Adding to this was concerns raised about scope creep of this thesis, which was limited to the existing fuselage, and producability of the stringers. Summing up the pros and cons resulted in the scrapping of the Truss-Stringer concept. See Figure 4.6 for a sketch of the key details of the Truss-Stringer concept.

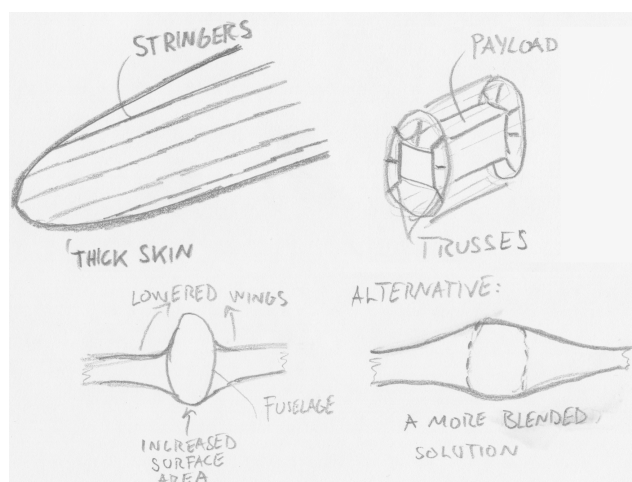


Figure 4.6: *Sketch of the Truss-Stringer concept*

As the name suggests, the Sea Plane concept was inspired by sea planes and their design features which enables them to land on water. The belly of the fuselage would be remodeled to increase surface area and have longitudinal grooves intended to give way for loose soil or grit, so that the fuselage could "dig" into the ground. A thicker layer of material for the belly would facilitate belly landing by adding stiffness. Stringers, similar to those suggested for the Truss-Stringer concept, would provide longitudinal stiffness, in addition to the skin itself. Transverse stiffness would be provided by multiple frames, which also would supply mounting for payload and batteries. Reduced landing contact force, increased stability during skidding (though not as much as for the Truss-Stringer concept), and simplified internal access for operators were the assumed pros of the Sea Plane concept. Engineers at KDS pointed out that the solution of frames providing mounting for payload as well as transverse stiffness was a common design which had proven its feasibility. They also added

that the longitudinal stringers would most likely be unnecessary, as the skin was assumed to provide enough stiffness. As for the Truss-Stringer concept, this concept involved redesigning the fuselage, and therefore, the same concerns about scope creep were raised. On top of this, the grooves in the reinforced belly was identified as a possible source of issues during manufacturing, and the reinforced belly itself could possibly add weight to an already weight-sensitive design. However, this concept was not scrapped, but rather modified so that the result was a fuselage consisting of a single laminate skin and multiple transverse frames. In other words, the sea plane aspect of the concept was removed so that the fuselage would not require a re-design. Due to this alteration, the name of the concept was changed to "Multiframe". Figure 4.7 depicts the main features of the Sea Plane concept, while Figure 4.8 depicts the alternative reinforced belly with or without grooves.

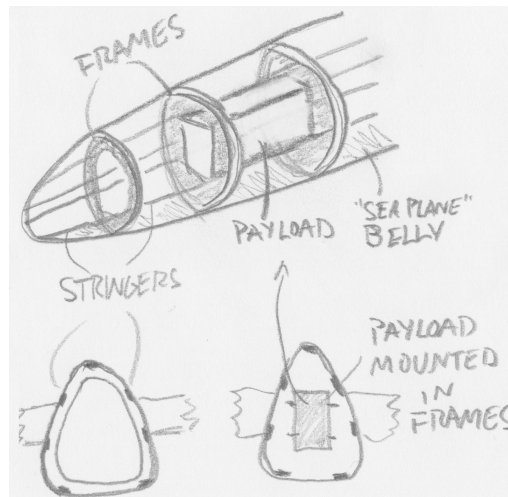


Figure 4.7: Sketch of the main features of the Sea Plane concept

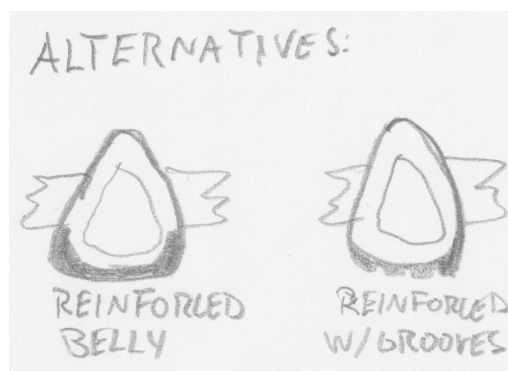


Figure 4.8: Sketch of the alternative belly reinforcement of the Sea Plane concept

Similar to the Multiframe concept, the Keelson concept included several transverse frames. Instead of multiple stringers, a large longitudinal keelson would provide stiffness. Continuing with the foam core idea, the keelson was also thought to be manufactured by dressing a foam core with prepreg tape. Providing leeway between the keelson and the frames, cutouts in the lower parts of the frames would allow for deflections of the fuselage's belly without directly disturbing the payload or batteries. Besides the keelson and the multiple frames, no modification of the fuselage design was suggested, thereby reducing risk of scope creep.

Engineers at KDS identified the Keelson concept as possibly being problematic to manufacture. Especially manufacturing a keelson with a relatively large cross-sectional area which followed the contours of the fuselage, and was clad with prepreg tape which needed to be cured in an autoclave. As for the Multiframe concept's stringers, the keelson was deemed possibly redundant, which in turn increased solution value. However, this modification resulted in the Keelson concept being too similar to the Multiframe concept, and was therefore

removed from further consideration. Figure 4.9 depicts the Keelson concept.

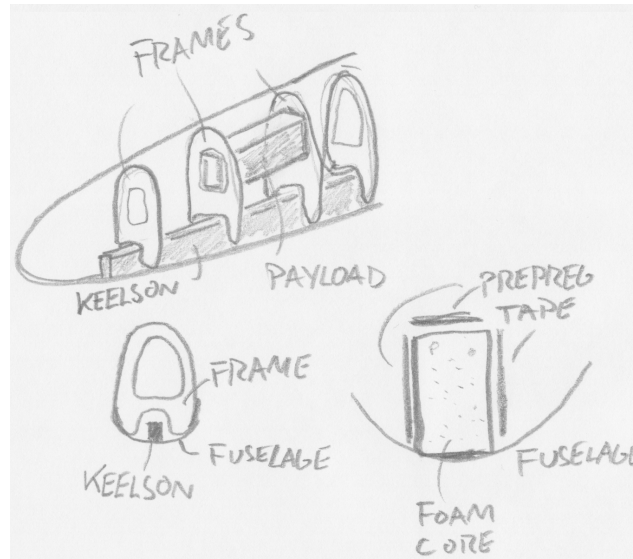


Figure 4.9: Sketch of the main features of the Keelson concept

The fourth concept, the Sandwich Skin, differed from the other three in the way that its skin did not consist of a single laminate. Instead, the suggested skin consisted of a sandwich structure with a foam core clad with laminate layers on each side. Providing shear stiffness on its own, the sandwich skin was assumed not having to rely on as many frames as previously suggested concepts. Due to this, the number of frames was cut to two, one for each of the major internal components (payload and batteries). This resulted in a concept proposal consisting of relatively few components, which added to the assumed pros of foam, with good impact damping capabilities, being used in a sandwich structure, and no alteration having to be done to the existing fuselage design. Engineers at KDS pointed to experience of sandwich structures being problematic to manufacture, especially for such curved shell structures as the UAV fuselage. Another identified drawback associated with the Sandwich Skin concept, was that permanently installed, large frames could hinder access to the front and rear of the fuselage (camera and motor, not included in this thesis), possibly resulting in the nose and rear to be detachable/accessible from elsewhere. However, despite these drawbacks the Sandwich Skin concept was chosen to be included in the analyses. Primarily, it was deemed to be able to provide valuable insight into the performance of two different skin structures for the fuselage, adding knowledge to further design efforts and development decisions. Figure 4.10 depicts the Sandwich Skin concept.

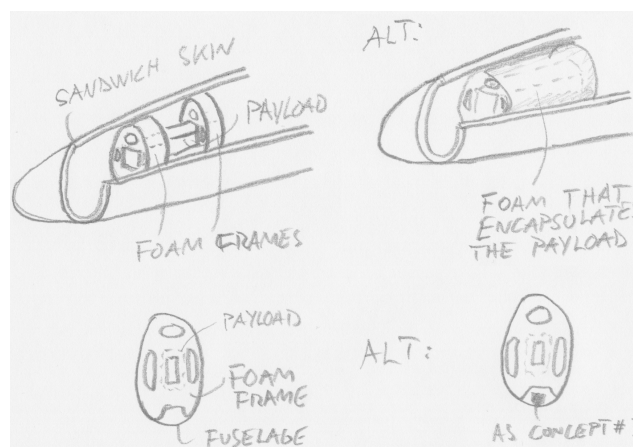


Figure 4.10: Sketch of the main features of the Sandwich Skin concept

4.2.2 Computer Aided Design

Before the proposed internal fuselage structure was developed using the tools described in the Methods chapter, a modification of the existing fuselage nose section was performed. This modification was done to remove geometry which were non-tangent with the rest of the fuselage and therefore could give rise to issues during modeling, production, and loading. In Figure 4.11, the resulting nose section is presented next to the old geometry.

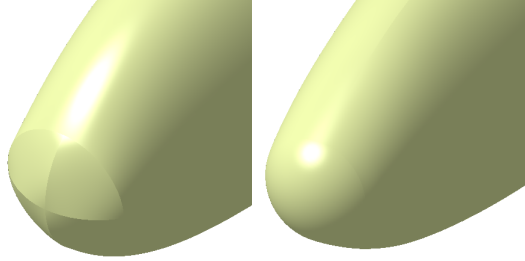


Figure 4.11: *Nose geometry modification. Left: old nose section, right: new nose section.*

This modification increased the total length of the fuselage from 1.35 [m] to 1.38 [m], which remained well within the constraining maximum length of the storage crate dimensions specified in Chapter 1.

Multiframe Concept

Figure 4.12 depicts the CAD model of the Multiframe concept. Nine frames in addition to the aft closing section make up the internal stiffening structure. An added feature is the belly-reinforcement which consists of the same material as the frames (Rohacell 110 IG foam). In the CAD model, the payload (front) and the batteries (rear) are represented using simple dummies consisting of an isotropic material with an applied thickness to meet weight estimations. Besides the frames, the main feature which separates the Multiframe Concept from the Sandwich Skin Concept is the thin composite skin with a thickness of 1.44 [mm] (nine 0.16 [mm] plies). This thickness was based on a recommendation from an experienced engineer at KDS of a skin thickness of $1 \leq t \leq 2$ [mm].

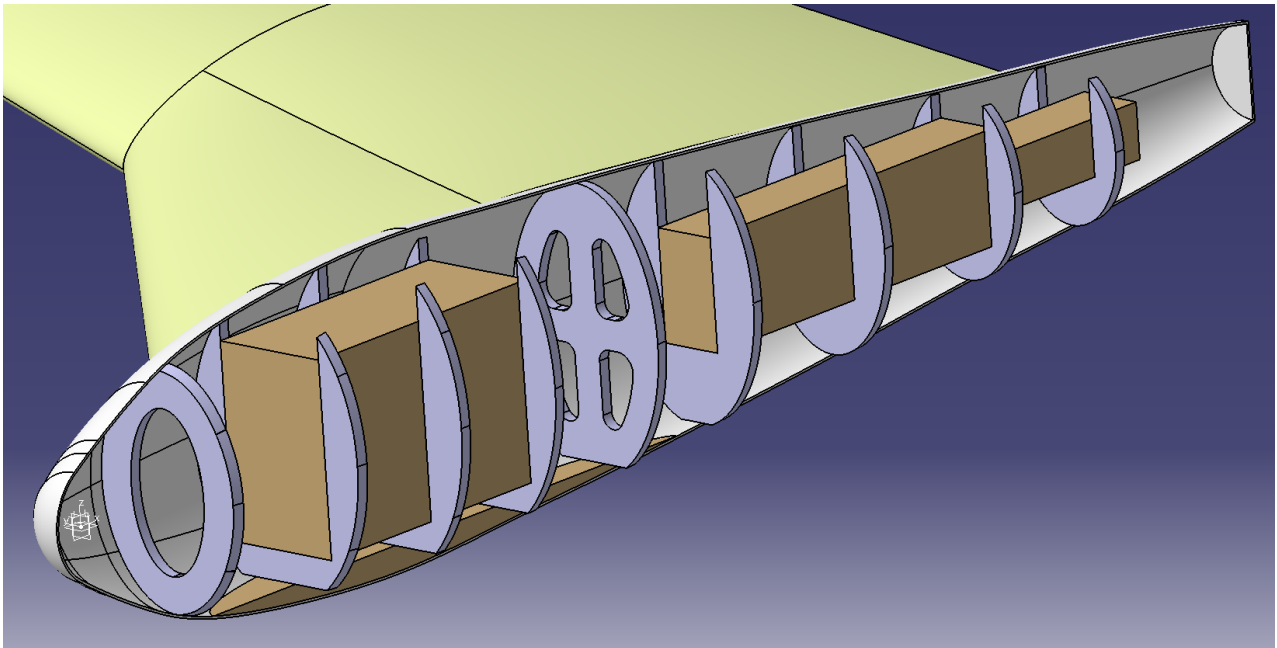


Figure 4.12: *Multiframe Concept*

Sandwich Skin Concept

The Sandwich Skin Concept can be seen in Figure 4.13. Compared to the Multiframe Concept, the frames are fewer, but more complex. Completely submerged into the frames, the payload and batteries are surrounded by more material than for the Multiframe Concept. These larger frames have more surface area in contact with the inner skin surface, adding to area for the transfer of forces. As opposed to having a single laminate skin, the Sandwich Skin Concept has a sandwich skin with a core of 8 [mm] Rohacell foam (same as used for the frames), which is clad, on both sides, with five plies of the same composite material used for the Multiframe Concept. Total skin thickness is $2 \times 5 \times 0.16 + 8 = 9.6$ [mm].

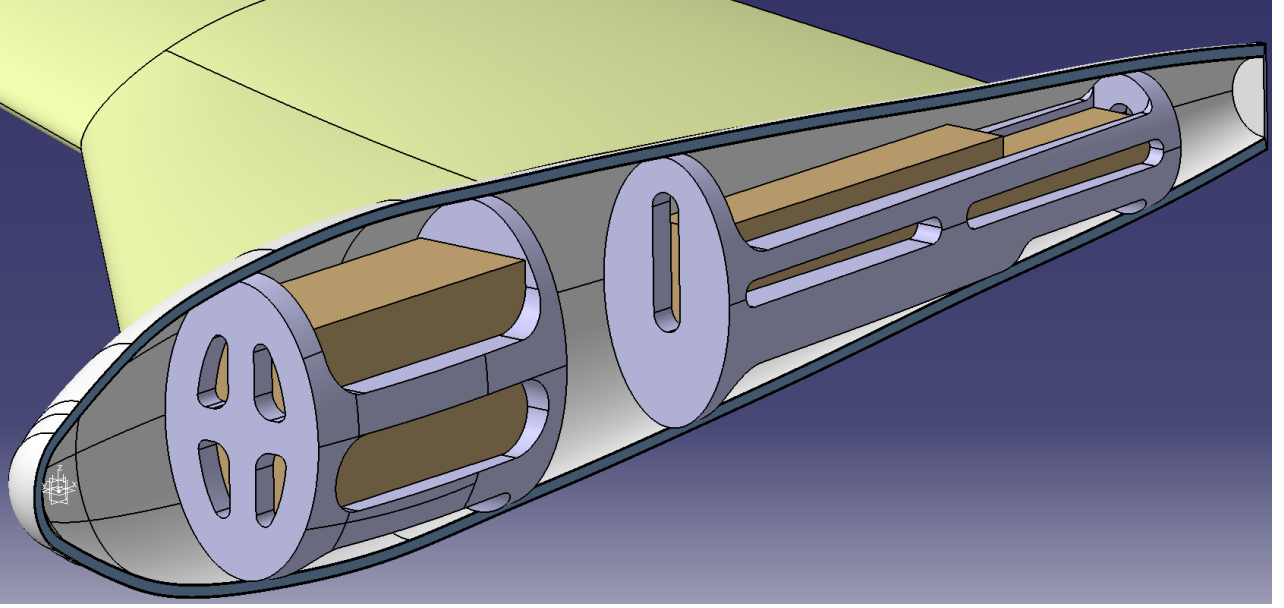


Figure 4.13: *Sandwich Skin Concept*

4.3 Orthotropic Constants Study

Table 4.1 presents the results of the Orthotropic Constants Study. As can be seen, the resulting von-Mises stress is fairly constant throughout all tests. However, when the Poisson's ratio in the yz plane is increased to almost 0.5, the stress decrease slightly, a result which is turned and magnified by setting ν_{xz} to the same value. To avoid this increase in stresses due to guesstimated values, the material parameters were set to those of test number 10 (which was more in accordance with the other material parameters). This decision was also backed by Kristiansen (2013). Test geometry and setup are presented in more detail in Appendix D.

Table 4.1: Test settings and results

Test	E_z [GPa]	ν_{yz}	ν_{xz}	Max eq. stress [MPa]
1	0.001	0.001	0.001	80.4
2	10	0.001	0.001	80.4
3	10	0.1	0.001	80.4
4	10	0.1	0.1	80.4
5	20	0.1	0.1	80.4
6	20	0.499	0.1	78.9
7	20	0.499	0.499	99.4
8	0.001	0.499	0.499	80.4
9	0.001	0.001	0.499	80.4
10	10	0.122	0.122	80.4

4.4 Finite Element Analysis

This section contains results obtained through Finite Element Analysis (FEA), starting with the stacking sequence testing. Following the stacking sequence testing, the results of both the pitch angle and descend velocity testing are combined into one section. A discussion and further evaluation of the results, including assumed consequences, are included in Chapter 5.

For the initial tests, quite prominent "sporadic" failure was observed for all cases. Here, "sporadic" was defined as reported material failure in single, or very small clusters of, elements which were relatively far away from larger clusters of reported failure. These sporadic results were assumed unrealistic due to them turning up in areas where the stresses were relatively small (far smaller than in the areas directly influenced by the impact), such as on the side of the rear skin section and on the nose of the UAV.

After conferring with Lauth (2013), one error source was identified as being the values used in the stress limit material model for the composite prepreg. Although the Tsai-Wu failure criterion for thin shells was applied, which only relies on certain in-plane stress limits (see Chapter 3), numerical values had to be inserted even for those values that initially were set to 0 (which were set to 0 due to them not taking part in the failure criterion). Relatively, the values inserted were very small and it was therefore assumed that they would not influence the solution in any noticeable manner other than reducing some of the sporadic "noise". By using *Tsai-Wu constants* in the material definition (as described in Chapter 3), it was made certain that the Tsai-Wu failure criterion was in fact used instead of any other failure criterion, for instance Tsai-Hill. Values inserted to remove some of the sporadic noise can be seen in Table 4.2, in Figure 4.14, the result before and after inserting these values can be seen for a small segment of the skin where this helped in reducing noise.

Table 4.2: Inserted stress limits to reduce sporadic failure, as a reference, Tensile X was set to $407.7 [MPa]$ and Shear XY was set to $55.6 [MPa]$

Parameter	Value $[MPa]$
Tensile Z direction	2
Compressive Z direction	-2
Shear YZ	2
Shear XZ	2

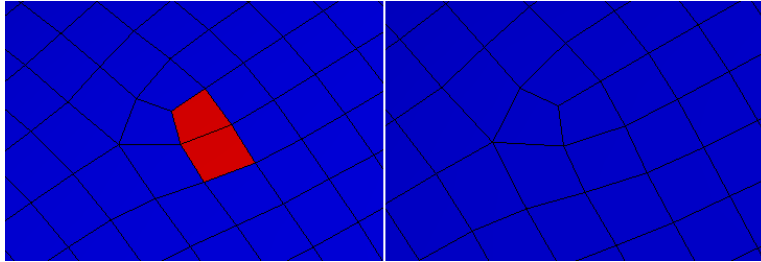


Figure 4.14: Before (left) inserting the values found in Table 4.2 and after (right), case: $2.5 [m/s]$ $\theta = 0 \text{ deg}$ $t = 3 [ms]$

4.4.1 Stacking Sequence Testing

The stacking sequence testing was performed for the Multiframe concept only, with the assumption that results were transferable to the Sandwich Skin concept, meaning that the best suited stacking sequence for the Multiframe concept, was assumed to also be the best suited for the Sandwich Skin concept. Stacking sequences tested are presented in Table 4.3. In Figure 4.15, the results for maximum equivalent stress (von-Mises) can be seen for the case of 0 deg pitch angle and 2.5 [m/s] descend velocity.

Shell element result settings (equivalent stress, max/min principal stress, and max shear stress) was set to *Top/Bottom*, meaning that results were shown for the top and bottom faces simultaneously, which combined with *Entire Section* plotted the results for the bottom layer of ply #1 (outer surface) and top layer of ply #9 (inner surface) (which corresponded to the top of Ansys' layer #9, outer surface, and the bottom of layer #1, inner surface). In practice, this meant that stresses presented in Figure 4.15 and other equivalent results were for either ply #1 or ply #9, whichever largest at the moment the result was saved by the solver. These settings were deemed correct due to the maximum stresses being found on either the inner or outer surface of the skin.

Table 4.3: Stacking sequences tested

#	Stacking Sequence
1	[0, 45, -45, 45, 0, -45, 45, -45, 0]
2	[0, 45, -45, 45, 90, 45, -45, 45, 0]
3	[90, 0, 90, 0, 90, 0, 90, 0, 90]
4	[45, -45, 45, -45, 45, -45, 45, -45, 45]
5	[90, 45, -45, 90, 0, 90, -45, 45, 90]

Appendix E contains plots of maximum and minimum principal stresses, maximum shear stress, and gradual failure plots, similar to that of Figure 4.17. All cases presented in Figure 4.15 ended in failure of the skin material, an example of the gradual failure for one of the cases can be seen in Figure 4.17. However, differences in resistance towards failure could be observed between the different stacking sequences. Figure 4.18 depicts the contrast between the strongest and the weakest stacking sequence. Ply-wise initial failure for each stacking sequence can be seen in Table 4.4.

Table 4.4: Time of first failure [ms]

	Stacking sequence				
Ply	#1	#2	#3	#4	#5
9	0.54	0.54	0.54	0.81	0.48
8	1.05	0.75	0.60	0.84	0.81
7	1.05	1.02	0.60	0.90	0.87
6	1.05	1.05	0.63	1.02	0.75
5	1.05	0.99	0.72	1.08	0.84
4	1.14	1.14	0.75	1.20	0.90
3	1.68	1.80	1.02	1.44	1.47
2	1.80	1.80	1.23	1.62	1.38
1	1.41	1.41	1.05	1.41	0.96

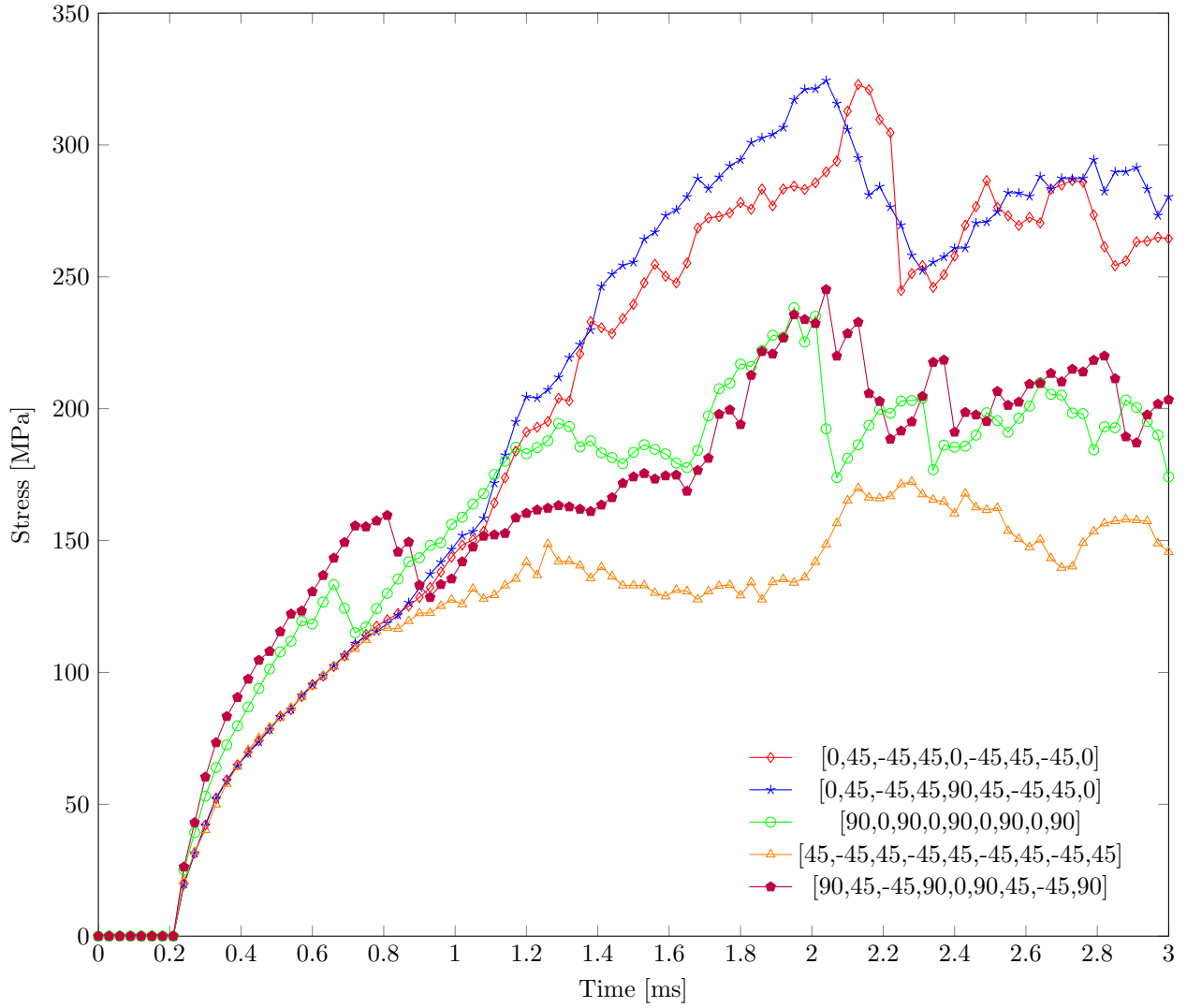


Figure 4.15: *Maximum von-Mises stress for five different stacking sequences*

Figure 4.15 shows that the stacking sequences that start and end with a 0 deg ply orientation, and thus are stiffest along the center line of the body, absorb more of the loading in the outer plies than the other stacking sequences. The same behavior, at a less extent, can be seen for the stacking sequences that starts and ends with 90 deg ply orientations, with the $[45, -45, \dots]$ stacking sequence absorbing the least of the loading in the outer/inner plies and thus spreading more of the load to the core plies. Here, the last effect, spreading the load to all of the plies, was considered beneficial as it reduced the loading for the outer and inner plies.

Stress results, specifically the contour lines, were clearly influenced by the ply's 0 deg direction, and differences between 0 deg, 45 deg, and 90 deg were quite distinct. Both 0 deg and 90 deg resulted in an approximate symmetric stress distribution, at least prior to severe multi-ply failure occurring. The 45 deg ply orientation resulted in a skewed/rotated distribution, with a clear correlation between the stress contours and the ply's stiffest local x -direction and the secondary, not so stiff, y -direction (see Chapter 3 for material data presenting the difference between the x and y directions in the unbalanced woven ply).

In Figure 4.16, the equivalent (von-Mises) stress distribution, with the local 0 deg and 90 deg fiber directions highlighted, for three stacking sequences is shown at the time $t = 0.6$ [ms]. Even though results for every stacking sequences are not shown, the same distribution can be found for stacking sequences that start out with the same principal fiber orientation. All scenes depicted in Figure 4.16 are in ply #1 (Ansys layer #9) for the Multiframe concept, in other words, the ply that is in contact with the ground.

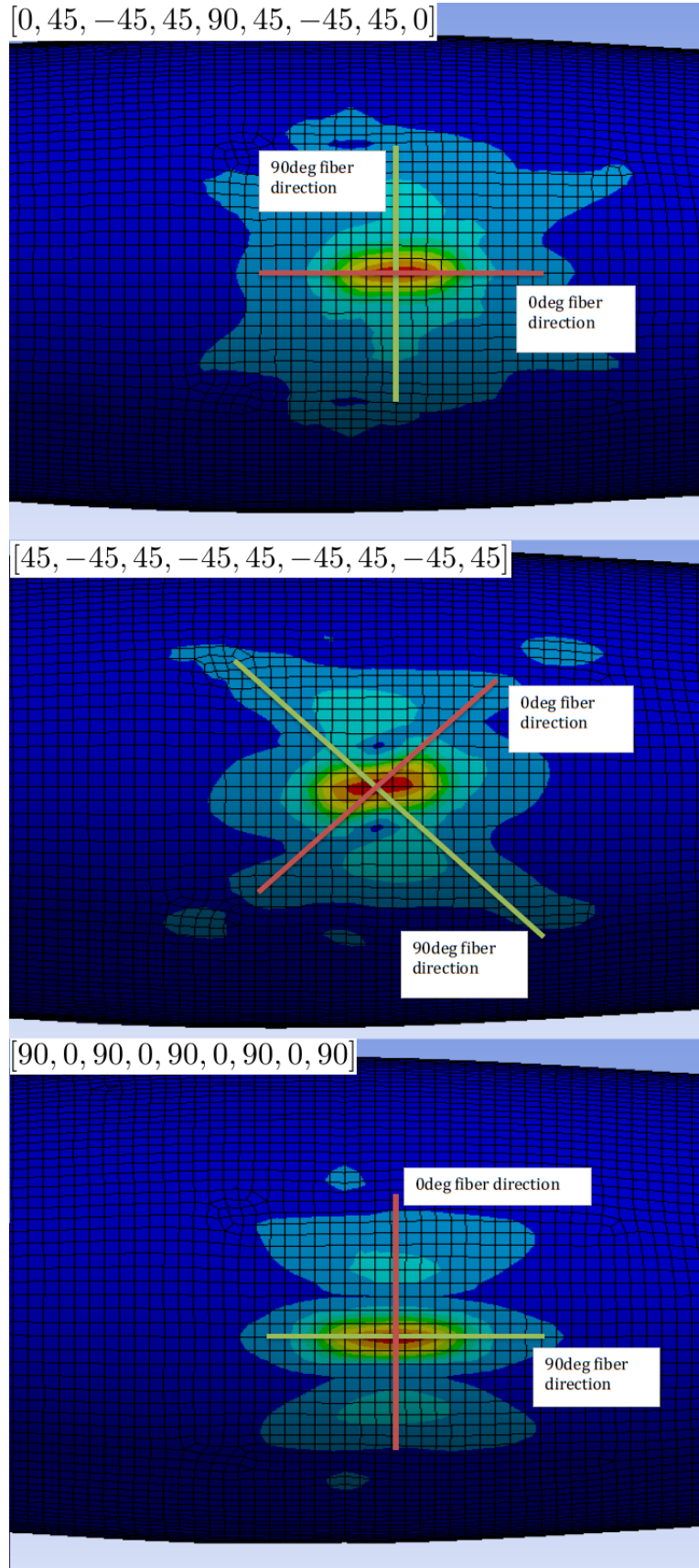


Figure 4.16: *Stress distribution relative to the ply's 0 deg and 90 deg fiber directions at $t = 0.6$ [ms], stress contours have not been generalized*

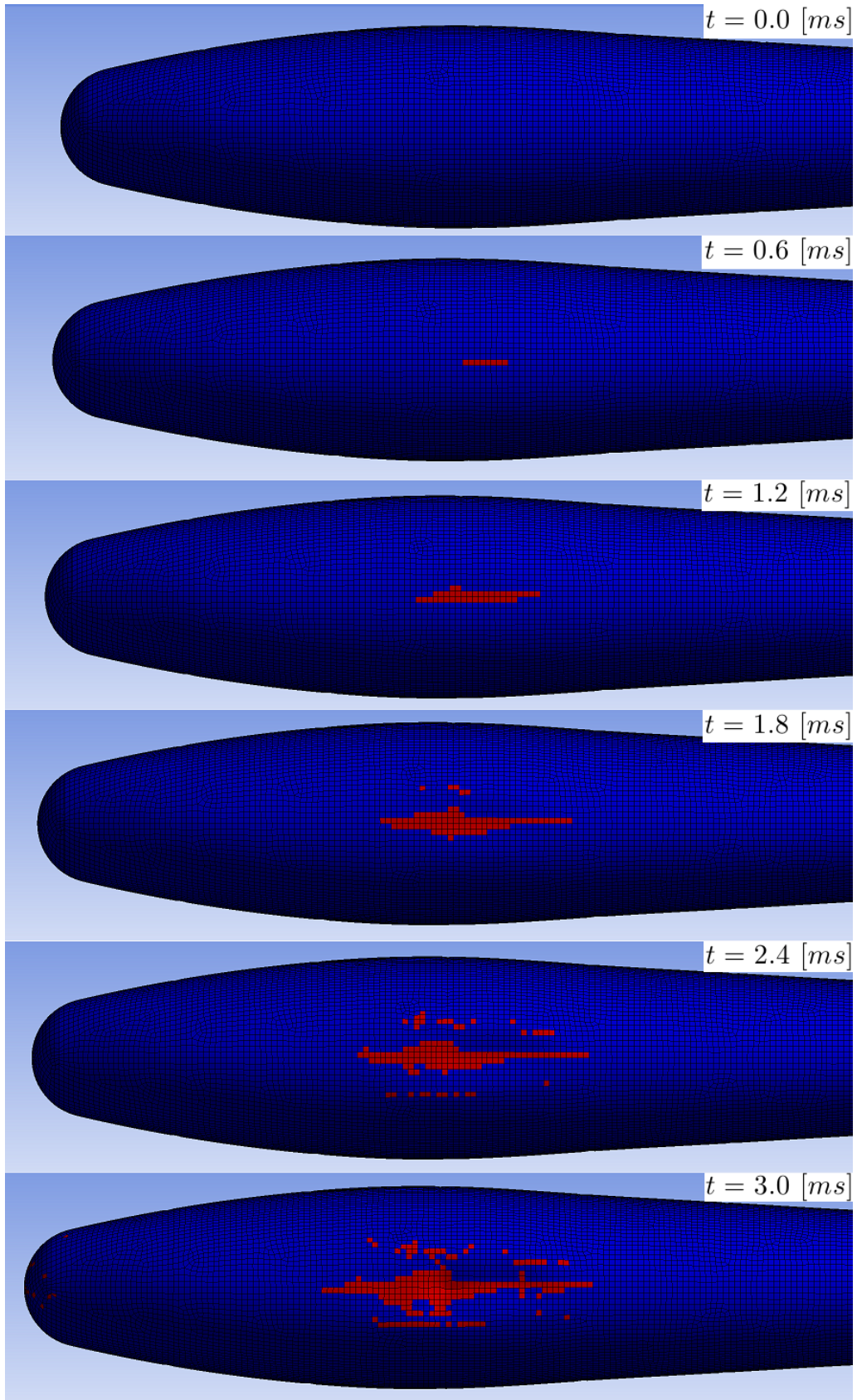


Figure 4.17: *Material failure for the $[90, 0, 90, 0, 90, 0, 90, 0, 90]$ stacking sequence, ply #9 (inner)*

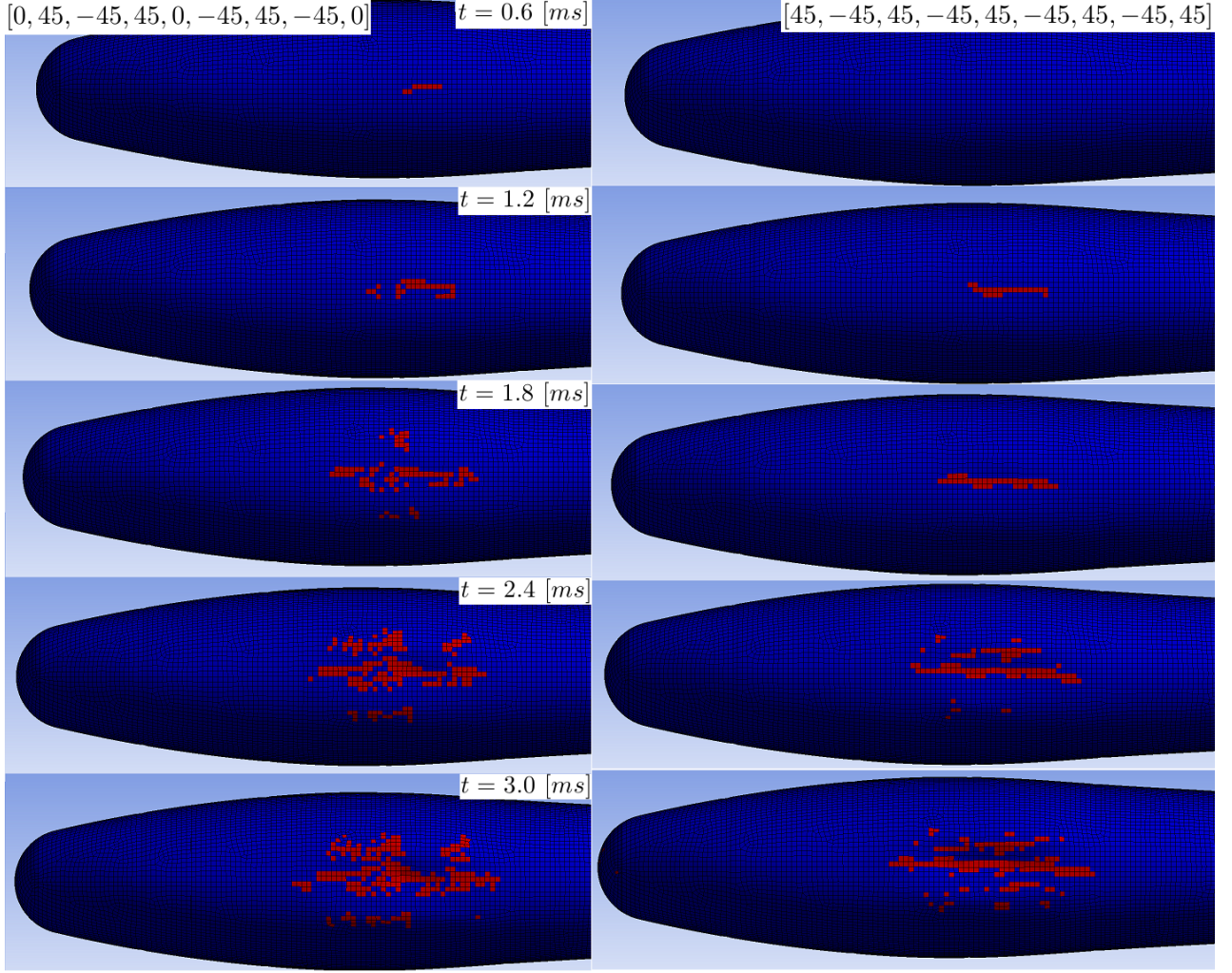


Figure 4.18: Comparison of resistance towards failure between the stacking sequences $[0, 45, -45, 45, 0, -45, 45, -45, 0]$ and $[45, -45, 45, -45, 45, -45, 45, -45, 45]$, ply #9 (inner)

Most results were symmetric up until failure, however, as failure was initiated, which generally had a non-symmetric propagation in the different plies, these stress results also became non-symmetric. Since post-failure in Ansys consists of removing the material's ability to sustain any shear stresses or negative pressures, (Ansys 2011), it is easy to understand why stress results were non-symmetric when the material failure itself was. However, the question of why failure propagates in a non-symmetric manner remains. One possible explanation is that the mesh was not perfectly symmetric, and therefore the impact stress wave would not propagate perfectly symmetric.

4.4.2 Pitch Angle (θ) and Descend Velocity Testing

For more results regarding failure for each ply, every concept, and all tests, see Appendix F.

Multiframe Concept

For the case where the descend velocity was set to 1 [m/s], the Multiframe concept still experienced quite severe failure in all plies. Essentially, the results for the 2.5 [m/s] test was replicated, but at a slower pace. The duration of the 1 [m/s] test was set to 7.5 [ms], which turned out to encapsulate more of the impact than what was done for the 2.5 [m/s] case. Therefore, end results for the 1 [m/s] case might look worse (also due to the extra sporadic reported failure) than the end results for the 2.5 [m/s], but they are not directly comparable. Adding to this was the uncertainties regarding relative distance between the skin and the ground, which was especially difficult to control for the Sandwich Skin, therefore, cases with the same pitch and descend velocity, but with different concepts, did not result in impact at the same time.

Besides a pitch angle of $\theta = 0$ deg, $\theta = 6$ deg was also tested. That particular pitch angle was chosen from the results of the Landing Parameter study, section 4.1.1, which showed that for a pitch angle of 6 deg, the stresses and strains in the skin was at a minimum. However, since the Landing Parameter study was performed on an empty fuselage model (of isotropic material), and did not include payload, batteries, nor frames, it turned out to not be directly transferable. Shortly after initial impact, the last frame (#9), which was connected to the skin at the bottom and had batteries resting on it, directly transferred the momentum of the batteries to the skin, resulting in massive skin material failure. The same phenomena could subsequently be observed for frame #8, #7, and to some extent also frame #6. To mitigate this severe failure, the above mentioned frames were trimmed so that they were not in direct contact with the bottom of the inner skin, thus disconnecting the direct path between the batteries and the point of impact. It is also noteworthy to mention that for these analyses, erosion on geometric strain had to be enabled to avoid numerical problems (with the default strain value of 1.5). In Figure 4.19, the failure of ply #9 (inner), before and after trimming the frames, is shown for the Multiframe concept at the time $t = 7.5$ [ms] for a descend velocity of 1.0 [m/s]. Although only *reducing* material failure, the results seen in Figure 4.19 certainly promote the solution of trimming the frames so that they are not in direct contact with the belly of the UAV.

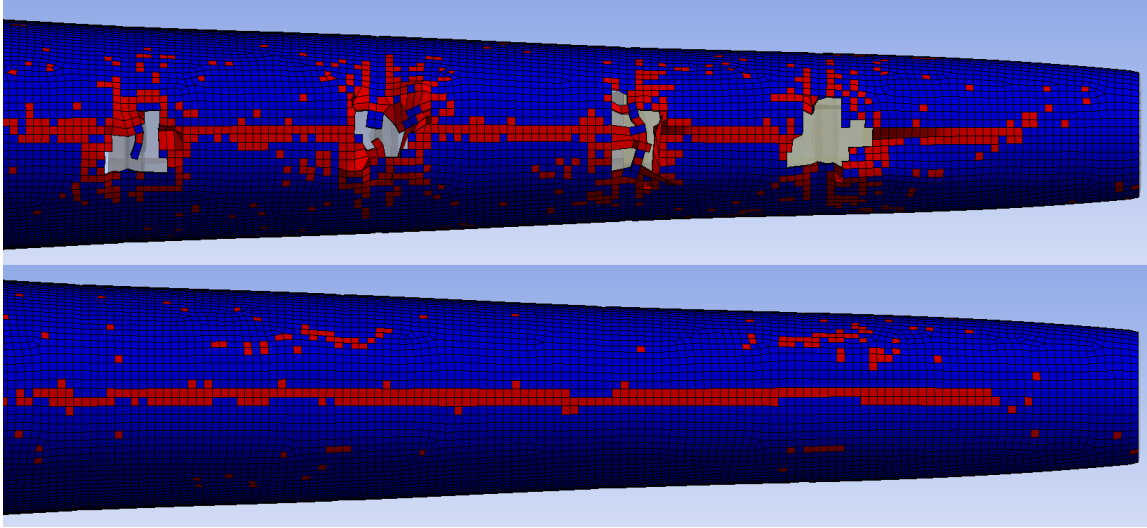


Figure 4.19: Failure in ply #9 before (top) and after (bottom) trimming frames #6 – 9 for the Multiframe concept, 6 deg pitch angle and a descend velocity of 1 [m/s], taken at the time $t = 7.5$ [ms]

At a descend velocity of 2.5 [m/s], the results were quite similar to that of the 1 [m/s] case. With a simulation duration of 3.0 [ms], the sporadic failure, due to assumed numerical issues, was less prominent than for the 1 [ms] case which had a simulation duration of 7.5 [ms] due to the lower descend velocity. Therefore, the results shown in Figure 4.20 for the 2.5 [m/s] case looks "cleaner" and maybe even not as severe, however, it probably would have looked even worse than that of the 1 [m/s] case if the simulation would run longer (at least the "actual", as opposed to "sporadic", failure). The simulation was not extended due to failure

already being reported, and the given insight regarding the loading and behavior of the concept was considered satisfactory.

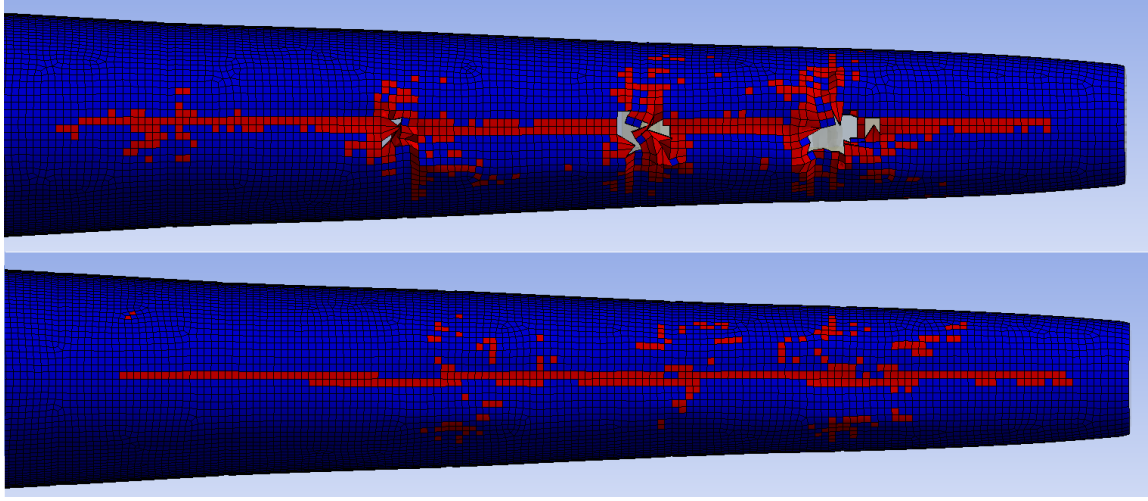


Figure 4.20: *Failure in ply #9 before (top) and after (bottom) trimming frames #6 – 9 for the Multiframe concept, 6 deg pitch angle and a descend velocity of 2.5 [m/s], taken at the time $t = 3.0$ [ms]*

Prominent for all cases where the pitch angle was set to 0 deg, was the forcing of the bulge inwards towards the payload. As the fuselage makes contact with the ground, the bulge start to deflect inwards, resulting in an increased localized tensile stress on the inner surface of the skin, which eventually leads to failure being reported along the center-line of the belly, in the innermost ply. After a short moment (in [ms]), a ridge start to appear on the inside, being formed by the inwards-forced bulge. This in turn leads to the outer skin experiencing an increase in tensile stress to the point of failure. Although none of the reported principal stress exceeds material strength limits, the combined stress state is severe enough to result in failure. The buckling behavior of the bulge can be seen in Figure 4.21.

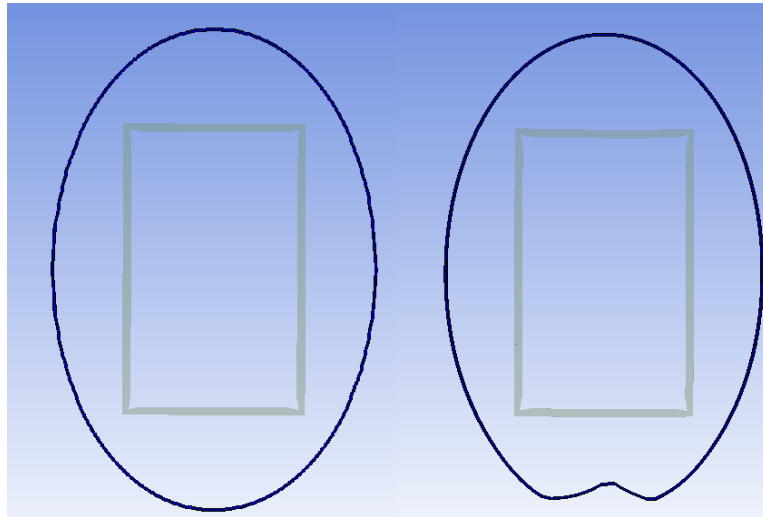


Figure 4.21: *Cross-section of the skin (and payload) for the 2.5 [m/s], 0 deg analysis showing the buckling of the bulge at the start (left) and end of the analysis (right)*

Sandwich Skin Concept

From the results presented in Appendix F, when dividing the sandwich skin into two laminates, one outer and one inner (disregarding the foam core), it can be seen that plies with similar reference fiber direction, return, at least very close to, identical failure results. One explanation for this would be that since the total skin thickness is 9.6 [mm], where 8 [mm] is the foam core leaving 0.8 [mm] for each of the inner and outer laminates, and the solver was set to use three shell sublayers (Analysis Settings), this could result in a poor resolution for the through-thickness evaluation of stresses and strains. In turn, possibly resulting in a, close to, uniform stress distribution in the inner and outer laminates, which in the end turns up as identical results for the plies grouped together in the respective laminates. An increase in shell sublayers would probably increase through-thickness accuracy, however, increasing the accuracy to such an extent that the relatively very thin inner and outer laminates had shown any improvement in accuracy, would probably add a lot of complexity to the model, severely increasing solve time. Already exceeding 13 hours in solve time for the 1 [m/s] case, this increased accuracy was considered too costly in terms of time resources. With three sublayers, the solution includes layers on the top, in the middle, and on the bottom of the surface, thereby returning accurate results for the outer- and innermost plies. In practical terms, this analysis setting of three shell sublayers meant that results reported for all plies in the inner and outer laminates could be considered as the results for plies number 10 and 1 respectively (not counting the core as a ply, starting the count from the outer surface).

As the "ridge" starts to form due to the bulge of the belly being pressed inwards, the inner plies start to fail along the bottom center-line. This behavior was also observed for the Multiframe concept, but for the Sandwich Skin concept, this only occur in the plies of the inner laminate. For the outer skin laminate, failure does not occur along the center-line, but rather at the points where the load from the frames are transferred to the skin. Figure 4.22 depicts both the failure of inner-laminate plies and the failure observed for outer-laminate plies, descend velocity and pitch angle was set to 2.5 [m/s] and $\theta = 0$ deg respectively.

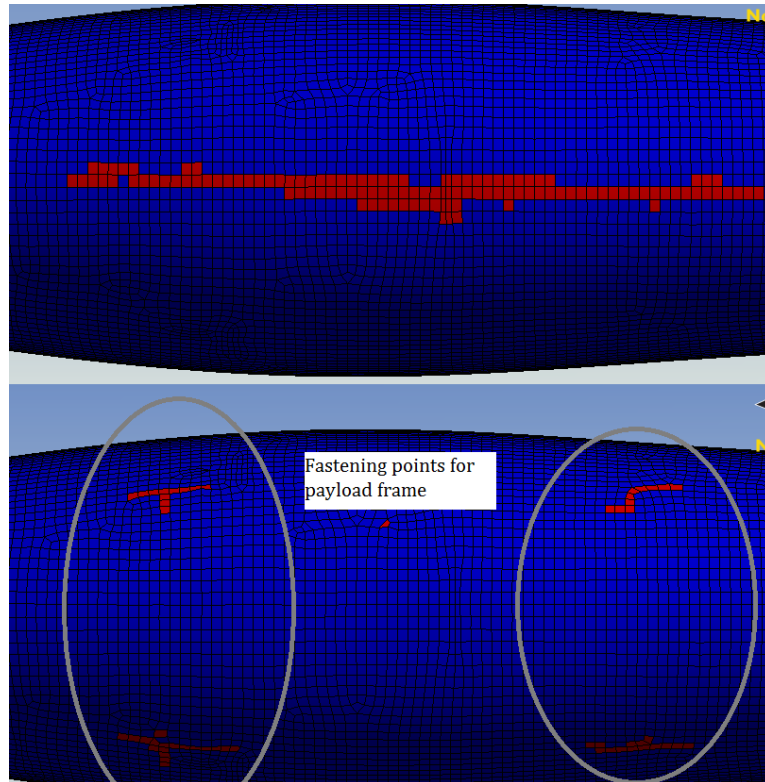


Figure 4.22: Failure in the inner ply (top) and outer ply (bottom) of the Sandwich Skin concept, descend velocity 2.5 [m/s], pitch angle $\theta = 0$ deg, $t = 4$ [ms]

Setting up a section plane (cut view) allowed the results for the outer plies to be scrutinized in more detail.

The failure was linked to the inertia forces of the payload being transferred to the skin, raising the question whether the frames were strong enough to support it, this behavior is depicted in Figure 4.23.

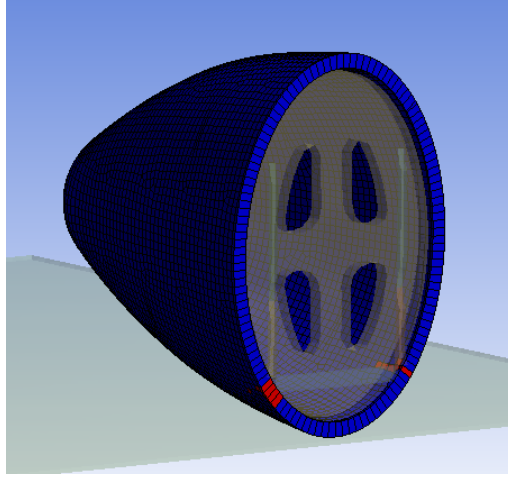


Figure 4.23: *Section cut showing the area of failure for the outer most ply (#1) as well as location of the payload and front frame supporting it, $t = 5$ [ms] $\theta = 0$ deg 2.5 [m/s]*

A possible explanation to why this behavior was not seen in the Multiframe concept's tests, was due to it being designed with three frames holding the payload, which were linked to the skin, and therefore was better equipped to soften the impact. Possibly, if the frames would have been represented using solid elements, or simplified in a manner which better represented actual geometry, the results could have turned out differently. However, this probably did not influence the failure reported for the inner laminate, and therefore it was not deemed time-worthy to modify the frame simplification in search of a better representation.

At a descend velocity of 1 [m/s] and a pitch angle of $\theta = 0$, the reported failure in both the inner and outer laminate is considerably less than for the 2.5 [m/s], $\theta = 0$ case. With reference to Figure 4.22, which depicts inner and outer failure for the 0 deg, 2.5 [m/s] case, Figure 4.24 shows a less severe inner- and outer-laminate failure.

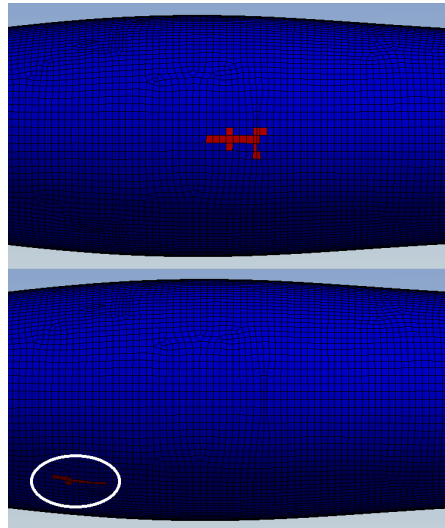


Figure 4.24: *Failure in the inner ply (#10, top) and outer ply (#1, bottom) for the 0 deg, 1 [m/s] Sandwich Skin test at the end of the simulation $t = 8.5$ [ms]*

When setting the pitch angle to 6 deg, failure occur in both the inner plies along the center-line of the belly,

as well as the areas for the inner plies where the rear battery frame is connected, and in the outer plies where the battery frame is connected in the rear and in the area where the body representing the batteries increases in size. This failure result can be seen for the inner and outer plies in Figure 4.25.

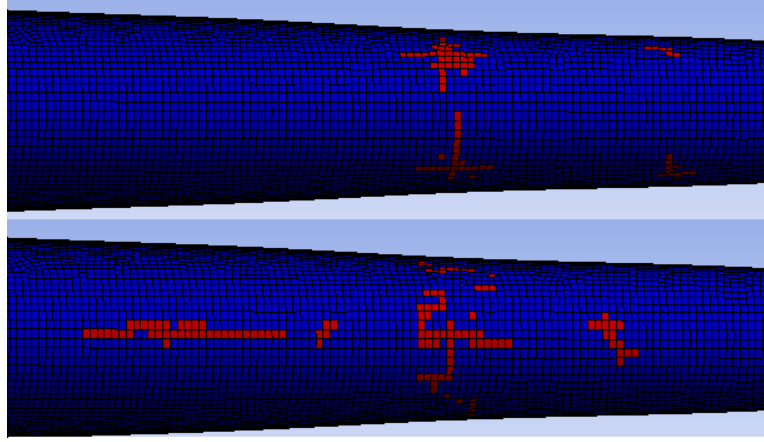


Figure 4.25: *Failure in the outer ply (top) and inner ply (bottom) for the Sandwich Skin concept, descend velocity 2.5 [m/s], $\theta = 6$ deg, $t = 4$ [ms]*

For the case where the pitch angle was set to 6 deg and the descend velocity to 1 [m/s], failure in the innermost ply did not occur for the Sandwich Skin concept. However, for the outermost ply, failure in the area where frames had been fastened on the inside, and where the body representing the batteries increases in size, did occur, as can be seen in Figure 4.26.

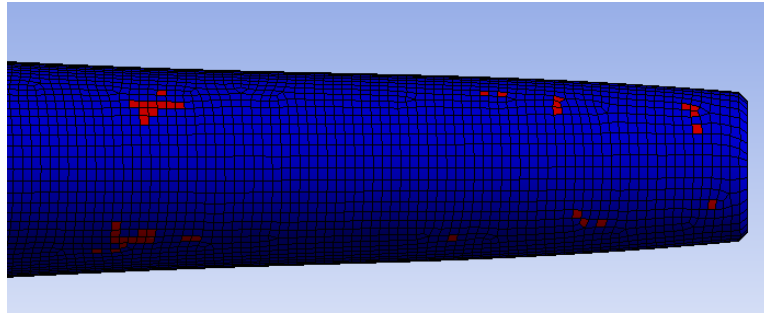


Figure 4.26: *Failure in the outer ply for the Sandwich Skin concept, descend velocity 1.0 [m/s], $\theta = 6$ deg, $t = 4$ [ms]*

5 Discussion

5.1 Concept Development

Creative work such as concept development is ideally performed in a team consisting of individuals with varied experience and different mindsets. Identifying functions, solutions, and possible synergies from each other's ideas are only a few of the advantages doing concept development in a group have over performing it alone. Due to this, the concepts generated for skin and internal structure could possibly have been different and better suited if the concept development had been done in a group as opposed to the author doing it by himself. However, as the communication with, and feedback received from, experienced professionals at KDS was of such good perceived quality, these risks are assumed to be as minimized as possible. Also bear in mind that the main scrutinized part of the UAV, the skin, was tested for two different skin solutions, the Sandwich Skin and the Multiframe concepts, with the latter being a fairly traditional solution that, arguably, should have been tested no matter what due to its simplicity.

5.2 Finite Element Analysis

The process of performing Finite Element Analyses of the two different skin and internal structure concepts could have been improved on by utilizing Ansys version 14.5 instead of 14.0. By doing so, ACP (post) would have been available for Explicit Dynamics systems, and solid bodies could have been combined with surface bodies in meshes consisting of both solid and shell elements. However, this version was not available from Chalmers, or any other sources, and could therefore not have been adopted for this project. When studying the alternative to the chosen path, utilizing version 14.5 without ACP (pre) to define the composite skin, it does not look as bleak. Version 14.0 with ACP (pre) gave much better control over the fiber directions and applied thicknesses, than what using the native-in-Mechanical option *Layered Section* could ever have done. This statement is backed up by the author's personal experience from trying to evaluate results obtained using *Layered Section*, from the start of the project to up until late April.

Results presented in Chapter 4 give little reason for celebration, however, it is far better to have these results at an early stage of the development than in later stages where design changes would have been much more costly. At a total weight of 12.5 [kg], with as little surface area in contact with the ground as UAV concept three has, the solution of landing the UAV on its belly is not feasible. For the Multiframe concept, the impact with the ground forces the narrow bulge of the belly upwards, resulting in failure in all plies. Failure initiates in the inner-most ply (last in the stacking sequences) due to high local tensile stresses, and propagates to other plies as the inner-most ply weakens (starts to lose its resistance towards shear stresses). After a short period of time (keep in mind that the unit of time for explicit analyses is milliseconds), as a ridge on the inside of the fuselage starts to form, failure is initiated in the areas on both sides of the bottom center-line of the skin, starting in the outer-most ply (#1). At this point, severe failure has occurred in all plies and the UAV's skin is deemed broken.

Although ending in failure as well, the Sandwich Skin concept walks a different path to it. Starting out, the same inner laminate failure occurs for most cases, but the outer side of the fuselage does not show the same failure along the center-line of the belly as the Multiframe concept's outer plies do. For the outer plies of the Sandwich Skin structure, failure is initiated at the areas where the payload frame surface has been attached to the skin. It seems as though the inertia forces from the mass of the payload are transferred through the frames, resulting in failure on the opposite side of the skin. Possibly, these results could have been different if the frames, which originally are connected to the skin along the longitudinal bars of the frames, were not simplified to the basic surface structures used here. As mentioned above, this would have required version 14.5 of Ansys, which was not available to the author during the project. Since the buckling behaviour observed for the Multiframe concept does not, at least not to the same extent, occur for the Sandwich Skin concept, the outer laminate does not experience failure along the center line of the belly. Due to this, the Sandwich Skin concept can be said to display improved resistance towards buckling relative to the Multiframe concept.

5.3 Future Recommendations

Clearly, continuing development work on the third airframe concept's current design, with belly landing as a means of landing, is not suggested. If the LocalHawk project scope regarding size and total weight are not altered, a re-evaluation of different means of landing the UAV should be performed. If the preferred solution still is belly landing, then a redesign of the fuselage is needed. Possible improvements that could be considered are listed below:

1. Increase the surface area in contact with the ground during landing to reduce impact force loading
2. Avoid a direct path between the impact load and heavy-weight objects such as the payload and batteries
3. Change the material of the skin to something stiffer, such as carbon fiber
4. Avoid concentrated loads, such as thin, trimmed frames
5. Try to distribute the mass as much as possible
6. Include longitudinal stiffening elements, especially for the belly, that can stiffen the fuselage up and resist buckling of the belly.

Although being presented as means to facilitate the continued use of belly landing for an un-altered project scope, parts of the list above could also be used as general guidelines for designing UAVs with belly landing as a chosen solution.

An optional path would be to alter the project scope, scale down the UAV airframe concept and facilitate belly landing by applying some, or all, of the guidelines presented in the list above.

As for the knowledge generated regarding the application of explicit FE solvers, it could be transferred to the professional branch of KDS (not student affiliated projects) and add to existing know-how. For professionals with experience in conducting implicit FE analyses, the provided guidelines in this thesis, especially its appendices, could possibly bridge the gap and enable him or her to successfully utilize explicit FE solvers.

6 Conclusion

The research questions stated at the outset of this thesis were:

- Is belly landing as a conceptual solution feasible for the LocalHawk UAV?
- If not, what changes could be performed to facilitate belly landing?
- How does the different skin and internal structure concepts perform during belly landing?
- How can an explicit solver successfully be applied to simulate the low-velocity impact of the UAV?

Two concepts for skin and internal structure were developed using product development methodology and analyzed in a low-velocity impact simulation by utilizing an explicit solver. As presented in Chapter 4 and discussed in Chapter 5, the proposed solution of belly landing for the design of the LocalHawk UAV, concept three, is not feasible. Relatively high weight combined with a small landing surface area on the belly of the UAV results in failure in all of the tested cases, for both concepts of skin and internal structure. However, the results of this thesis can be used to guide continued design. Focusing on saving weight wherever possible and increasing the surface area of the body in contact with the ground, could in the end result in a viable concept for the LocalHawk UAV with the advantages of belly landing. In addition to the conclusion of belly landing not being suitable for the third UAV concept, it has also been shown that cutting load paths between the internal components and the belly minimizes the damage to the skin (and probably also the internal components). Other recommendations can be seen in the list provided in the Discussion, Chapter 5.

This thesis has successfully applied a commercial explicit solver to a low-velocity impact problem. Know-how regarding application of explicit solvers to low-velocity problems has been generated and is readily available for KDS to adopt. Analysis settings as well as best-practice during pre-processing have been presented and discussed. Both a general guide for doing explicit analyses, as well as a case presenting some of the differences between high-velocity and low-velocity impacts are included in the appendices. These appendices, along with the main body of the thesis, could be of assistance to anyone learning to apply explicit FE solver to impact problems.

Bibliography

- Abrate, S. (2001), 'Modelling of impacts on composite structures', *Composite Structures* **vol. 51**, pp. 129–138.
- Akhilesh, K. J., Sathyamoorthy, S., Bharath, K. & Laxminarayan, K. (2012), Impact analysis of mini uav during belly landing. Submitted to the India HyperWorks Technology Conference Series 2012.
- Almefelt, L. (2011). Lecture hand-outs in the course PPU140 "Design methodology preparatory course", unpublished, Gothenburg: Chalmers University of Technology.
- Ansys (2011), *Ansys 14.0 Help System*, SAS IP, Inc. Help System for Ansys release 14.0.
- Ansys (2012), *Ansys 14.5 Help System*, SAS IP, Inc. Help System for Ansys release 14.5.
- Ansys (2013), *Introduction to Ansys Explicit STR*. Course held by Mikael Lauth on behalf of EDR&Medeso AB in Gothenburg, March 2013.
- ANSYS.NET (2002), 'Review of yield/failure criteria', http://ansys.net/ansys/tips_sheldon/STI03_Yield_and_Failure.pdf. online: accessed April 30th 2013. ANSYS.NET newsletter.
- Armstrong, M. (2013). Composite Technologist, Gurit. Personal Communication April 2013.
- Austin, R. (2010), *Unmanned Aircraft Systems: UAV Design, Development, and Deployment*, Hoboken: John Wiley & Sons.
- Barnard, J. (2010), 'Use of unmanned air vehicles in oil, gas and mineral exploration activities', http://www.barnardmicrosystems.com/ME4%20files/download/BML_AUVSI_2010.pdf. online: accessed February 13th 2013. Barnard Microsystems Ltd.
- BBC News (2012), 'Drones to protect nepal's endangered species from poachers', <http://www.bbc.co.uk/news/science-environment-18527119>. online: accessed February 13th 2013.
- Callister, W. D. (2007), *Materials Science and Engineering: An Introduction*, 7th edn, New York: John Wiley & Sons.
- Cantwell, W. J. & Morton, J. (1991), 'The impact resistance of composite materials - a review', *Composites* **22**(5), 347–362.
- Flanagan, D. P. & Belytschko, T. (1981), 'A uniform strain hexahedron and quadrilateral and orthogonal hourglass control', *International Journal for Numerical Methods in Engineering* **17**, 679–706.
- Franklin, W. (2010), *Structures and Materials*, Reston: American Institute of Aeronautics and Astronautics (AIAA), chapter 19, pp. 491–550.
- Guizzo, E. (2011), 'Video: Watch flying robots build a 6-meter tower', <http://spectrum.ieee.org/autotom/robotics/diy/video-watch-flying-robots-build-a-6-meter-tower>. online: last controlled June 01st 2013.
- Hart-Smith, L. J. (1992), 'The ten-percent rule for preliminary sizing of fibrous composite structures', Conference Paper. Society of Allied Weight Engineers: 51st Annual Conference, Hartford, Connecticut, May 18-20. Paper number 2054.
- HRW (2009), 'Precisely wrong: Gaza civilians killed by israeli drone-launched missiles', http://www.hrw.org/sites/default/files/reports/iopt0609webwcover_0.pdf. Report published by the organization Human Rights Watch.
- Imaoka, S. (2001), 'Implicit vs. explicit dynamics', http://ansys.net/?mycat=tnt_sheldon13. online: accessed Feb.04.2013.
- Kristiansen, P. O. (2013). Project Engineer, KONGSBERG. Personal Communication March/April 2013.
- Lauth, M. (2013). Senior Engineering Analyst, FEM, EDR&Medeso. Personal Communication March-May 2013.

- Lien, J. R. & Løvholden, G. (2001), *Generell Fysikk: Mekanikk*, 3rd edn, Oslo: Universitetsforlaget. Norwegian.
- Liu, G. R. & Quek, S. S. (2003), *The Finite Element Method: A Practical Course*, Oxford: Elsevier/Butterworth-Heinemann.
- Liu, K. S. & Tsai, S. W. (1998), 'A progressive quadratic failure criterion for a laminate', *Composites Science and Technology* **58**, 1023–1032.
- Megson, T. (2010), *An Introduction to Aircraft Structural Analysis*, Oxford: Elsevier/Butterworth-Heinemann.
- Meriam, J. L. & Kraige, L. G. (2008), *Engineering Mechanics: Dynamics*, Vol. 2, 6th edn, Hoboken: John Wiley & Sons.
- Merriam-Webster (2013a), 'Video: Watch flying robots build a 6-meter tower', <http://www.merriam-webster.com/dictionary/airframe>. online: last controlled June 01st 2013.
- Merriam-Webster (2013b), 'Video: Watch flying robots build a 6-meter tower', <http://www.merriam-webster.com/dictionary/fuselage>. online: last controlled June 01st 2013.
- NASA Dryden Flight Research Center (2013), 'Nasa chases climate change into the stratosphere', <http://www.nasa.gov/centers/dryden/news/NewsReleases/2013/13-01.html>. online: accessed February 13th 2013.
- Oxford Dictionary of Physics* (2005), 5th edn, Oxford: Oxford University Press.
- Pahl, G., Beitz, W., Feldhusen, J. & Grote, K. H. (2007), *Engineering Design: A systematic approach*, 3rd. edn, London: Springer.
- PBS Nova (2002), 'Spies that fly: Time line of uavs', <http://www.pbs.org/wgbh/nova/spiesfly/uavs.html>. online: accessed February 13th 2013.
- Pugh, S. (1990), *Total Design: Integrated Methods for Successful Product Engineering*, Wokingham: Addison-Wesley.
- Rao, S. S. (2011), *The Finite Element Method in Engineering*, 5th edn, Boston: Elsevier.
- Raymer, D. P. (2012), *Aircraft Design: A Conceptual Approach*, 5th edn, Reston: American Institute of Aeronautics and Astronautics (AIAA).
- Richardson, M. O. W. & Wisheart, M. J. (1996), 'Review of low-velocity impact properties of composite materials', *Composites Part A* **27A**, 1223–1131.
- Robinson, P. & Davies, G. A. O. (1992), 'Impactor mass and specimen geometry effects in low velocity impact of laminated composites', *International Journal of Impact Engineering* **12**(2), 189–207.
- Rohacell (2013), 'Material information rohacell ig', <http://www.rohacell.com/product/rohacell/en/products-services/rohacell-ig-ig-f/pages/default.aspx>. online: last accessed May 26th 2013.
- SCRA (2006), *STEP Application Handbook ISO 10303*, 3rd edn, SCRA, 5300 International Boulevard North Charleston, SC 29418, USA. Available online at http://www.uspro.org/documents/STEP_application_hdbk_63006_BF.pdf (15.04.2013).
- Shah, P. Z. (2009), 'Pakistan says u.s. drone kills 13', <http://www.nytimes.com/2009/06/19/world/asia/19pstan.html>. online: last controlled June 01st 2013.
- Simulia (2012), *Getting Started with Abaqus: Interactive Edition*, Dassault Systemes: Simulia, Rising Sun Mills, 166 Valley Street, Providence, RI 02909-2499, USA. User Guide for Abaqus/CAE.
- Sjöblom, P. O., Hartness, J. T. & Cordell, T. M. (1988), 'On low-velocity impact testing of composite materials', *Journal of Composite Materials* **22**, 30–52.
- Sun, J. S., Lee, K. H. & Lee, H. P. (2000), 'Comparison of implicit and explicit finite element methods for dynamic problems', *Journal of Materials Processing Technology* **105**, 110–118.

- Sundström, B., ed. (2007), *Handbok och formelsamling i Hållfasthetslära*, Stockholm: Institutionen för hållfasthetslära KTH. Swedish.
- Taylor, R. L., Nithiarasu, P. & Zhu, J. Z. (2005), *The Finite Element Method Set: Its Basis and Fundamentals*, Vol. 1, 6th edn, Oxford: Elsevier/Butterworth-Heinemann.
- The Economist (2012), ‘This is your ground pilot speaking’, <http://www.economist.com/news/science-and-technology/21567053-autonomous-civil-aircraft-could-be-flying-cars-go-driverless-your>. online: accessed February 13th 2013.
- Tolson, S. & Zabaras, N. (1991), ‘Finite element analysis of progressive failure in laminated composite plates’, *Computers & Structures* **38**(3), 361–376.
- Tsai, S. W. & Wu, E. M. (1971), ‘A general theory of strength for anisotropic materials’, *Journal of Composite Materials* **5**, 58–80.
- Ulrich, K. T. & Eppinger, S. D. (2012), *Product Design and Development*, 5th. edn, New York: McGraw-Hill.
- Wikipedia (2013), ‘The economist’, http://en.wikipedia.org/wiki/The_Economist. online: last controlled June 01st 2013.
- Yüksel, S. (2009), Low velocity impact analysis of a composite mini unmanned air vehicle during belly landing, Master’s thesis, METU: Middle East Technical University.
- Zenkert, D. & Battley, M. (2011), *Foundations of Fibre Composites*, chapter 7. Fatigue of Composite Materials, pp. 7.1–7.28.

Appendices

A Explicit Analyses

This appendix contains a rough user's guide to performing explicit analyses. Ansys 14.0 has been the applied FEM software for this thesis work, however, at the initial part of the thesis, version 14.5 was used (as access to ACP (pre) and therefore v. 14.0 had not been granted). The course taken at EDR&Medeso was given in version 14.5, and therefore, this appendix guide is written for that particular version of Ansys. Due to this, instructions given here may not be applicable for other software packages. Settings and instructions given here are, at least close to, 100% transferable to Ansys version 14.0.

A.1 Introduction

As described in the main section of this thesis, explicit analyses are normally used to investigate transient events of short duration ($\Delta t < 1[s]$). A typical problem where an implicit solver could be applied successfully is for a static, structural analysis. For such a case, there often exists one or more areas of the structure in question which is of special interest (for example critical design features where the loading results in stress concentrations). Special attention is then directed at this area with the mindset that "if the weakest point survives the loading, the rest of the structure will also". For an explicit analysis, a stress wave which propagates throughout the entire structure is one of the major contributors to the loading. Explicit analyses are often therefore scoped to the entire structure, where small features might not influence the result quite as much as it might for a static analysis (stress concentrations).

This appendix aims partly to give readers who have experience with implicit FEA an introduction to explicit "thinking", and partly to give readers an insight into the process of preparing and running an explicit analysis so that they can better interpret and understand the main body of this thesis. Please note that this appendix does not replace a training manual/course written/given by experienced professionals. Statements which have no citations are based on the author's own experience with running both implicit and explicit analyses. The author takes no responsibility for work based on this appendix.

A.2 Pre-Processing

Pre-Processing encompasses all of the preparatory work that is needed for the analysis to run, achieve realistic results, and do so within an acceptable time duration. This section will follow the steps required in Ansys, starting with Materials Definition (Engineering Library in Ansys), Geometry Preparation, Contacts and Body Interactions, Meshing, Boundary Conditions, and Analysis Settings.

A.2.1 Materials Definition

An extensive library is available in Ansys for describing material properties (in addition to lots of predefined materials). This guide will not go into detail concerning models used for elastic/plastic/hyperelastic etc. behavior, those are either pretty much the same as for implicit analyses, or they do not fit within the scope of this appendix. The important thing to remember when doing explicit analyses, is that mass is central in dynamic events, therefore density must be accurately defined.

A.2.2 Geometry Preparation

Preparing geometry for explicit analyses differs from implicit preparation in the sense that for explicit analyses, a throughout-the-structure uniform mesh (see section A.2.4) is very important, and care should therefore be taken to facilitate this *for the entire structure* and not just a particular section of it.

A.2.3 Contacts and Body Interactions

Ansys Workbench will automatically define Bonded contacts between bodies included in the imported assembly. Generally, contact definitions between bodies that are supposed to collide should be deleted. Contact between colliding bodies is handled by the settings under Body Interactions. Here, frictionless, frictional, bonded, and reinforcement may be chosen as body interaction.

If shell elements are used and Contact Detection is set to Trajectory, the property Shell Thickness Factor becomes available. Lauth (2013) recommends setting this factor to 1, which according to Ansys (2012) means that the contact shell thickness will be equal to the physical shell thickness.

A.2.4 Meshing

Meshing of a given structure to be analysed using an explicit solver, differs from meshing the same structure when it is to be analysed using an implicit solver. The mesh directly influences the solve time due to the time step for an explicit analysis being proportional to the size of the smallest element (Ansys 2013). A uniform element size facilitates the computation of the dynamic stress wave that propagates throughout the mesh.

In Ansys, the physics preference must be set to "Explicit" (default for an explicit analysis but if a stand-alone mesh is produced, then the physics preference need to be specified) (Ansys 2013). An "Explicit" mesh physics preference influences whether or not midside nodes for solid elements are kept or dropped by default (dropped, linear elements only), degree of smoothing, and pace of transition. Smoothing (low, medium, or high) refers to the number of iterations performed by the software while creating the mesh to position nodes relative to surrounding nodes and elements with the overall goal of increasing element quality (Ansys 2012). Setting the smoothing to high (default for explicit), ideally, produces a uniform mesh. Transition (slow or fast) sets the element-size growth pace between areas of differently sized elements by controlling the maximum growth factor between elements. A slow transition setting produces smooth transitions, while a fast setting results in more abrupt changes in element size.

Element Type

Hex elements are the preferred solid elements for explicit analyses due to them being more efficient and sometimes more accurate for slower transients (Ansys 2013). Ansys (2013) suggest striving for hex elements, but also argues that tetrahedral elements can fulfil accuracy and solution time requirements. In Ansys, a wide variety of methods can be used for meshing 3D, solid bodies:

- Automatic
- Sweep
- Tetrahedron
 - Patch Conforming (Delaunay method)
 - Patch Independent (Octree method)
- Multizone
- Hex Dominant

Sweep, Multizone, and Hex Dominant will all produce meshes consisting of, mostly, hexahedral elements while Tetrahedron will, as the name suggest, produce tetrahedral elements. The Tetrahedron method can be divided into two different sub-methods; Patch Conforming, and Patch Independent. Patch Conforming (PC) creates elements which conforms with outer edges, faces, and vertices by defining the mesh from the surface and inwards. Patch Independent (PI) on the other hand, starts from the core of the body and proceeds outwards until it reaches a surface, therefore not always reproducing edges, faces, and vertices exactly. According to Lauth (2013), PC has a tendency to produce non-uniform meshes with poor internal-element quality, especially for bodies with complex surfaces. PI on the other hand, results in more uniform meshes since the complexity of the body surfaces are not given any consideration when meshing the internal volume of the body. For this reason, PI is the preferred tetrahedral mesher for explicit analyses since mesh uniformity is of major importance.

When producing meshes consisting of hexahedral elements, pyramid elements may be used by the meshing algorithm. These pyramid elements will be divided into two tetrahedral elements when starting an explicit analysis, possibly resulting in very small elements which in turn will decrease the time step (i.e. increase solve time). Due to this production of small elements, special care should be taken when meshing to avoid, at least reduce the total number of, pyramid elements. As will be made clearer under section A.2.6, some "tricks" may be applied to reduce the impact of a small amount of pyramid/small elements to the total solution time.

For surface bodies, quadratic elements are preferred over triangular elements. Generally, 2D elements will result in a larger time step than for 3D elements and will therefore, in addition to the simplified model, reduce solve time. In Ansys, Automatic (Quadrilateral dominant) or Uniform Quad/Tri are the most common methods for producing meshes for explicit analyses.

Mesh Refinement

A typical application for implicit solvers are for static structural analyses. Often, there is a particular area of the structure that is of special interest due to elevated stresses relative to the rest of the structure. When defining the mesh, local refinement can then be applied to enhance accuracy in this area, as opposed to the entire mesh, and thereby save computational resources for other areas of the structure where accuracy is less important. For explicit analyses, the stress wave propagation throughout the entire structure is of major importance and the position of the region with the highest stress changes with it. Therefore, element size should be uniform for the entire structure (to a certain degree), and mesh refinement for explicit analyses rather consists of increasing element uniformity, quality, and if possible facilitating the direction of stress-wave propagation by "constructing" a flow path, meaning the elements are oriented in the same direction.

When evaluating the overall quality of the mesh, visual inspection serves as a valuable tool. Since internal elements of solid-body meshes influence the solver time step just as much as the elements that are visible at the surface of the mesh, visual inspection should not be confined to external elements only. Using dynamic cross sections, Section Plane in Ansys, with whole elements shown can greatly aid this process. If mass scaling is applied (see sections A.2.6 and A.3.2), control of elements using dynamic cross sections is important, but could also highlight problematic areas of the mesh.

A.2.5 Boundary Conditions

Besides defining a force or a pressure, loading can be defined as an initial velocity (both translational or angular). Drop tests where objects are simulated being dropped from a given height could be performed with the object being distanced from a surface at the given height with an applied standard earth gravitational acceleration. However, this would be a quite serious waste of computational resources as the time it takes for the object to hit the ground would be processed with, approximately, depending on deformation, erosion and other effects, the same time step as for the impact itself (i.e. very small). Instead, simple kinematic relations should be applied to obtain the impact velocity and the geometry modeled with a very small gap (0.1 [mm] is not too small). An example for constant acceleration is a drop from 5 [m]:

$$\begin{aligned} V^2 - V_0^2 &= 2as \\ V_0 &= 0 \\ a &= g = 9.81 \left[\frac{m}{s^2} \right] \\ s &= 5 [m] \\ V &= \sqrt{2gs} = \sqrt{2 * 9.81 * 5} = 9.9 \approx 10 \left[\frac{m}{s} \right] \end{aligned}$$

A.2.6 Analysis Settings

Before Ansys can run an explicit analysis, the end time, or duration of problem, must be specified. Default settings are chosen by Ansys for all other settings so when duration is specified, the solver may run. However, there are several tools available to facilitate solve time and accuracy. This guide will not describe all of them, but rather some pre-defined analysis types (based on impact velocity) and essential controllers.

Mass Scaling and Time Step

Prior to presenting the pre-defined settings incorporated in Ansys, some of the more important, efficiency wise, controllers will be discussed.

To reduce the total number of cycles to complete an explicit analysis (and thereby reducing the CPU solve time), mass scaling can be applied. Controlled by a user-determined minimum CFL (Courant-Friedrichs-Lewy) time step, mass scaling adds mass to elements which have a shorter CFL time step than the user-defined CFL time step. The goal is to increase overall solution efficiency without impacting accuracy or the integrity of

the results. Since it is a dynamic event, and mass is essential to the description of forces and moments, mass scaling should be used with utmost care. Evaluation of total mass added, and in which areas this mass is added, is very important when determining whether or not the results are valid.

Why added mass increases the time step can be seen from investigating the CFL condition:

$$\Delta t \leq f \times \left[\frac{h}{c} \right]_{min} \quad (\text{A.1})$$

Here, f is a time step safety factor, h is the characteristic length of the element, and c is the speed of sound in the material. Since the time step is inversely proportional to the speed of sound, it becomes proportional to the mass of the element (Ansys 2013):

$$\Delta t \propto \frac{1}{c} = \frac{1}{\sqrt{\frac{C_{ii}}{\rho}}} = \sqrt{\frac{m}{VC_{ii}}} \quad (\text{A.2})$$

Where C_{ii} is the material stiffness, ρ is the material density, m is the mass, and V is the element volume.

As mentioned above, mass scaling is controlled by setting a minimum CFL time step under "Analysis Settings". A simple procedure to obtain this time step is (also see Chapter 3):

1. Set type to Program Controlled under Analysis settings (default pre-defined setting), see below for more info
2. Set maximum number of cycles to a low number, but enough cycles so that the time step is stabilized (100 cycles is often more than enough)
3. Create a user defined result for time step (either type **timestep** for user defined result, or click "Solution", "Worksheet", and scroll down to **TIMESTEP**)
4. Evaluate all results
5. Explore the mesh to see which parts/elements have a short time step, use best judgment to determine a suitable time step
6. Change Analysis type to one with mass scaling enabled (Low Velocity, Efficiency, or Quasi-Static) and type in the determined time step
7. Run the analysis once more (few cycles)
8. Create a user defined result for mass scaling (either type **mass_scale** or find **MASS_SCALE** in the worksheet), or open the file **admodel.prt** and find the mass added for each part and total mass added for the entire model
9. If mass added and time step is acceptable, then change number of cycles to default value (1e7) and run the entire analysis

Hourglass Damping

Hourglassing occurs when elements are distorted in a special way so that the length of the diagonals in the element remains unchanged (Ansys 2013). Since strain rates and forces are expressed using diagonally opposite corners of an elements, there is no resistance to distortion when hourglass instability (hourglass distortion occurring in several elements in a region) occur. Partly due to the lack of stiffness, hourglass deformations can invalidate the results of an analysis and should be kept to a minimum (Ansys 2012).

Ansys has two built-in formulations available for hexahedral, solid elements; AUTODYN standard and Flanagan-Belytschko. AUTODYN standard hourglass damping is the default setting and is the most efficient in terms of memory and speed (Ansys 2013). The Flanagan-Belytschko formulation however is, as opposed to the AUTODYN standard formulation, invariant under rigid body rotation and is therefore better suited for large rigid body rotations. Invariant under rigid body rotation indicates that the hourglass forces sums to zero under rigid body rotation (Ansys 2012). The Flanagan-Belytschko formulation is based on the paper presented by Flanagan & Belytschko (1981).

Pre-defined Settings

There are five different pre-defined analysis settings in Ansys:

- Program Controlled (default)
- Efficiency
- Quasi-Static
- Low Velocity
- High Velocity

Details for each of these pre-defined settings can be found in the Ansys manual and will not be presented here. However, some trends can be identified to highlight differences between maximum/minimum robustness, and high/low velocity impacts.

Being the default setting, Program Controlled is focused on robustness of the solver and leaves little to the user to decide. Mass scaling is not applied which means that the user does not have to manually set a minimum CFL time step. As the name implies, Efficiency is designed to minimize solve time at the expense of robustness and sometimes also accuracy (Ansys 2013). All other pre-defined settings uses a time step safety factor of 0.9, but choosing Efficiency changes this factor to 1. Mass scaling is activated with a maximum element scaling factor of 1000% and maximum part scaling of 1000. Program Controlled and Efficiency are positioned at opposite ends of an imagined robustness-scale. Program Controlled with its turned off mass scaling, inherent robustness, and 0.9 time step factor *will get you there, slowly*. Efficiency on the other hand with a lack of a time step safety margin, possibly extensive mass scaling, and focus on reducing CPU cost *might not get you there, fast*.

High Velocity settings are recommended for large deformations or simulations where the impact velocity exceeds 100 [m/s], while the Low Velocity settings are recommended for small deformations or simulations where the impact velocity does not exceed 100 [m/s] (Ansys 2013). Please note that here, low velocity settings used in Ansys, does not imply the views presented in the Literature Review in the main body of the thesis, Chapter 2. When choosing Low Velocity, mass scaling is activated and the user has to define a minimum CFL time step as described earlier. For High Velocity on the other hand, mass scaling is deactivated. This could be expected considering the high initial velocities could possibly lead to relatively large deceleration forces, rendering the analysis sensitive to changes in mass. Another difference between High/Low Velocity settings, is the hourglass damping formulation used; AUTODYN standard is used for High Velocity, while Flanagan-Belytschko is used for Low Velocity. An imagined, possible result for low-velocity impacts, is the impactor ricocheting off of the target, entering a state of rigid body rotation thereby motivating the use of, the less efficient but invariant under rigid body rotation, Flanagan-Belytschko formulation. Continuing with this imagined example, an impactor with, what Ansys defines as high velocity, could possibly penetrate the target, thus reducing the need for an invariant-under-rigid-body-rotation formulation (i.e. motivating use of AUTODYN standard formulation for hourglass damping).

Body or element self contact has up until now remained unmentioned, however, a difference between High and Low Velocity settings is that High Velocity enables both element and body self contact, motivating application of High Velocity settings for problems where large deformations are expected. Low Velocity on the other hand (as well as Efficiency and Quasi-Static), disables self contact for both body and element, thereby removing waste of computational resources when checking for self contact in analyses where the user is certain that such events will not occur.

A.3 Post-Processing

Besides evaluating the influence specific explicit controllers have on the accuracy of results, post-processing of explicit analyses does not necessarily differ noticeably from post-processing of implicit analyses.

A.3.1 Results

Which results to check for is problem dependent. However, equivalent (von-Mises) stress and plastic strain are generally of interest for analyses including flexible structures (with material plasticity defined).

Typically, for a low velocity/strain problem, material erosion is not as interesting as it is for high velocity/strain problems.

A.3.2 Evaluating Accuracy

Engineering judgment should always be applied when evaluating results, but depending on the analysis settings used (see section A.2.6) the accuracy of the results should be evaluated with respect to particular controllers used. Proper evaluation is critical if Efficiency settings has been used, particularly if extensive mass scaling has been applied. Total mass added from mass scaling can be found in the file `admodel.prt` (generated when using the AUTODYN solver) which gives a part-by-part summary as well as total mass added. As described in section A.2.6, mass scaling can be evaluated directly from the model as well by creating a user defined result. Visualizing the extent of mass scaling can help in identifying problematic areas which in turn could prove valuable for mesh/model refinement.

Basic result validation with respect to mass scaling would be to check that parts experiencing acceleration does not have an unacceptable amount of mass added.

Besides mass scaling, hourglass energy should be controlled and evaluated relative to the total energy for the system (kinetic plus potential). In Ansys, this can be found under Solution → Solution Information and changing Solution Output to Energy Summary. If problems with hourglassing should occur, Lauth (2013) suggests the following:

- Refine the mesh
- Avoid point/line contacts
- Change hourglass damping controls to Flanagan-Belytschko (if not already applied)

B Sample Case - Explicit Analysis Walk-through

This Appendix serves to give readers of this thesis a walk-through of a simple explicit analysis. It will focus on setting up the analysis, and using the right controllers to ensure an efficient solve process and realistic results. To eliminate uncertainties related to geometry or material data, the geometry is simple, the problem is straight-forward, and common isotropic materials are used. As opposed to the model used in this thesis, the model for this walk-through consists only of 3D, solid elements. This limitation to 3D elements only, is performed so that the reader could get an insight into both 2D (main body) and 3D (appendix) elements.

A typical case for explicit analyses are impacts between bodies with high relative velocity, so called high-velocity impacts (HVI). However, explicit solvers could also be used for impacts between bodies with low relative velocity, or low-velocity impacts (LVI), as done in this thesis. In this appendix the same geometry will be used for both HVI and LVI, with the intent of highlighting differences between the two in setting up the analysis and using controllers to our advantage.

B.1 Preparation

Here, "preparation" refers to creating the geometry and importing it into the analysis system. Catia V5R20 was used to create the CAD geometry and Figures B.1 through B.4 depicts this.

The model consists of a bullet-shaped impactor hitting a flat surface (1 [mm]) at an angle. Figure B.1 shows the surface measurements (50 × 50) in [mm].

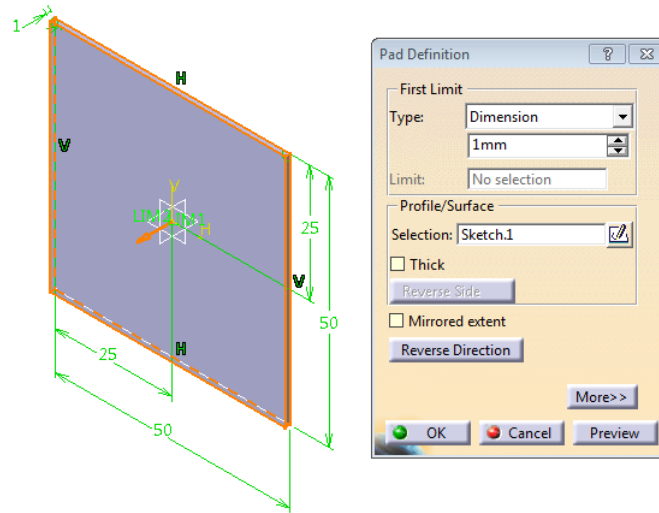


Figure B.1: *Surface extrusion*

Since the impactor is supposed to hit the plate at an angle, a plane needs to be defined which will form the support for the impactor sketch. Using one of the global planes as reference (here: zx plane), a new plane can be defined at a -20° angle, see Figure B.2.

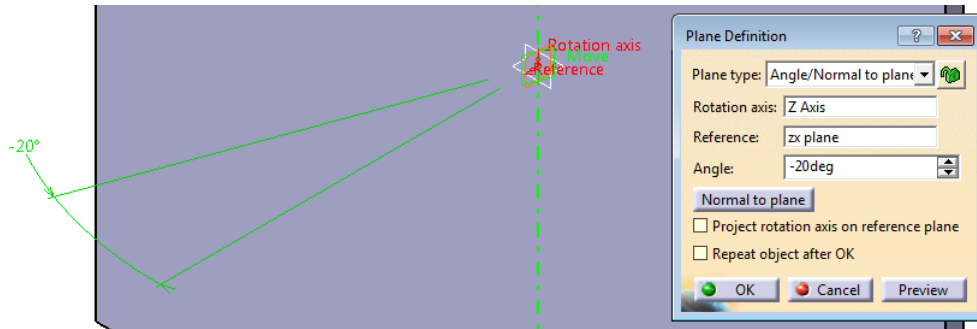


Figure B.2: *Definition of sketching plane for the impactor*

In Figure B.3, the impactor sketch can be seen. Notice the distance from the origin set to 13.05 [mm], this will, when revolved, result in a very small gap between the two bodies. Representing a "waste" in computational resources due to the movement from the initial position to the impact position having to be simulated using very small time steps, the gap between two impacting bodies should always be minimized (see Appendix A for more info). The distance between the two bodies can be seen in Figure B.4.

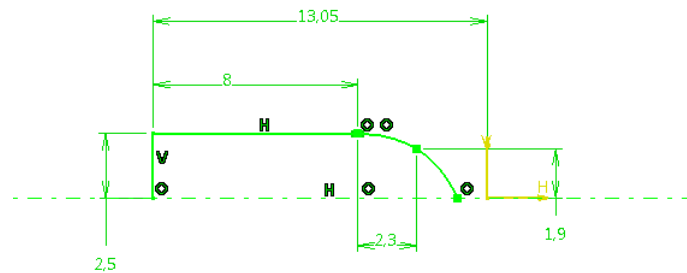


Figure B.3: *Impactor sketch for revolve/shaft*

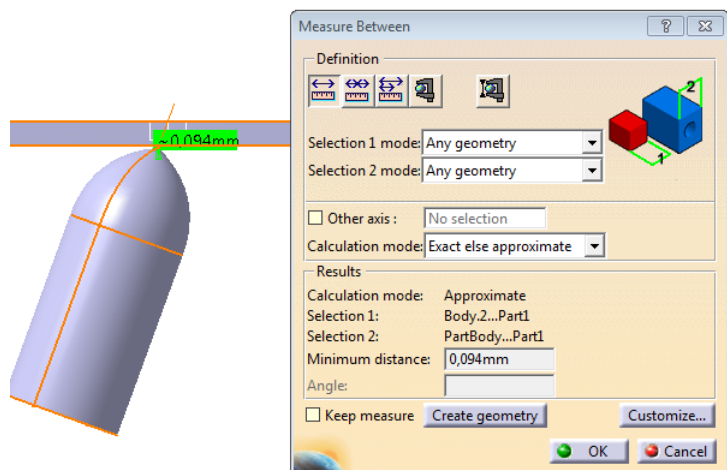


Figure B.4: *Distance between bodies*

Saving the geometry using the neutral file format STEP (.stp), will enable the use of virtually any FE software.

B.2 Pre-Processing

Pre-processing includes material definition, possible geometry modifications/simplification, meshing, defining boundary conditions, and setting up the analysis.

B.2.1 Material Definition

Since the intent is to minimize sources of error or ambiguity, so that this Appendix could be applied for other FE software packages with an explicit solver, the material models used were kept at a basic level. Both materials were taken from the Ansys General Non-Linear materials library; structural steel for the impactor and aluminium for the plate. Material constants for both materials are presented in Table B.1. Yield Strength and Tangent Modulus are used in a Bilinear Isotropic Hardening model.

Table B.1: Material parameters

Property	Aluminium Alloy	Structural Steel	Unit
Density	2770	7850	$[kg/m^3]$
Young's Modulus	71	200	$[GPa]$
Poisson's Ratio	0.33	0.3	$[-]$
Bulk Modulus	69.6	167.67	$[GPa]$
Shear Modulus	26.7	76.9	$[GPa]$
Yield Strength	280	250	$[MPa]$
Tangent Modulus	500	1450	$[MPa]$

B.2.2 Meshing

Here, two meshes will be presented, one created using default settings, and an improved mesh which will be created using user-input/mesh controls and modified geometry.

Default Mesh

In Figure B.5, the mesh generated using default settings is presented.

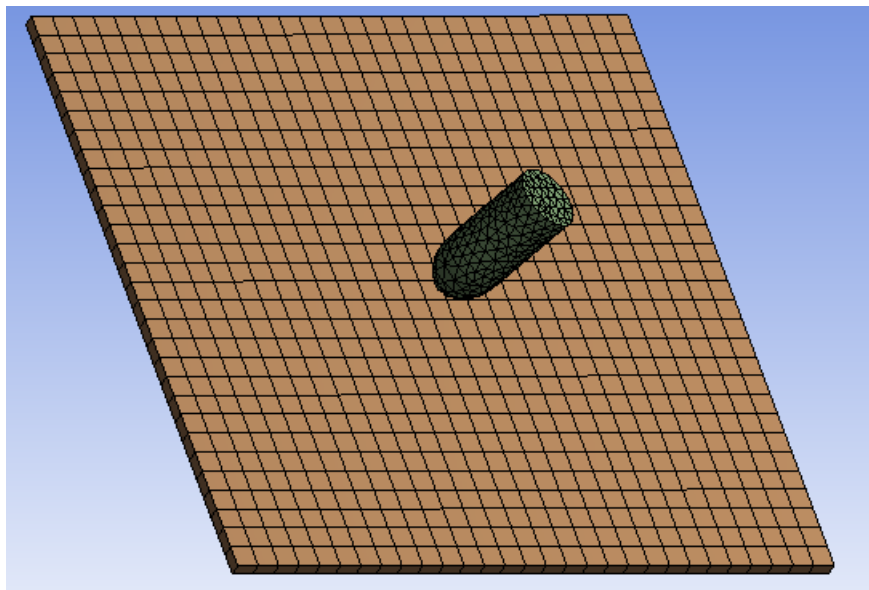


Figure B.5: *Default mesh*

Hexagonal elements have been applied for the plate, which is preferable for explicit analyses (see Appendix A). However, tetrahedral elements have been used for the impactor. These tetrahedral elements have been defined using a patch conforming algorithm, which is undesirable for explicit analyses due to it possibly creating elements with poor quality and low mesh uniformity. An inspection of the nodes using a Section Plane, a plane "cutting" the geometry so that internal elements can be viewed, reveals that there is a relatively large difference in element size and a few elements with poor quality. See Figure B.6 for a section highlighting some of the unwanted mesh areas, and Figure B.7 for a selection of elements with an element quality of less than 0.55.

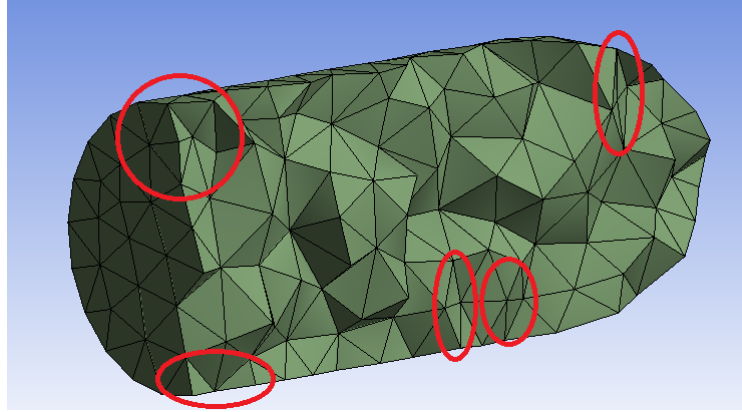


Figure B.6: *Section cut of the Impactor with some unwanted areas highlighted*

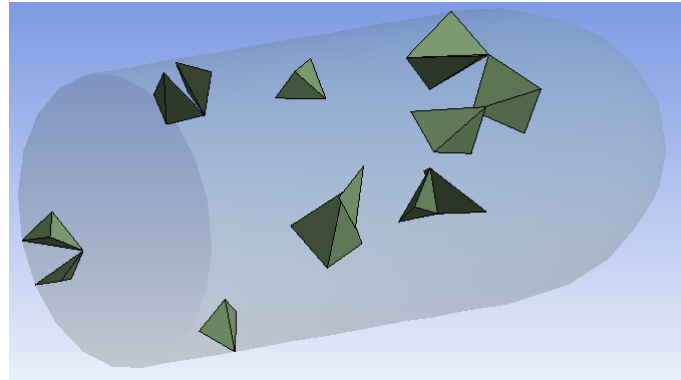


Figure B.7: *Elements with element quality less than 0.55*

If the mesh is regenerated, but now only for the impactor, it is possible to read the average element quality for the impactor to be 0.823 with $[min, max] = [0.435, 0.998]$, and the total number of elements in the impactor to be 2226. These low-quality elements could increase solve time dramatically by decreasing the solver's time-step.

Improved Mesh

Firstly, a very simple mesh improvement method is tested; patch independent tetrahedral meshing along with an element sizing of 1 [mm]. In Figure B.8, the resulting mesh can be seen when applying patch independent meshing. New average element quality for the impactor is 0.851, $[min, max] = [0.480, 0.998]$, and 2836 elements. Also, note the improved mesh uniformity in the core of the impactor, underlining the difference between patch conforming and patch independent tetrahedral meshing.

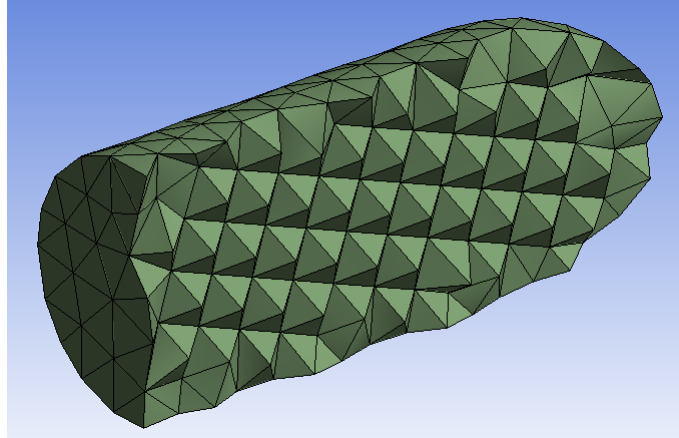


Figure B.8: Mesh created using a patch independent algorithm and an element sizing of 1 [mm]

Although, for this case, the resulting mesh using Patch Independent is of sufficient quality, further improvement might be possible. One possible way of improving the mesh is to divide the impactor into two bodies, a cylindrical stem and the "head". However, to keep the meshes of the two bodies connected, they will be joined by defining them as one multi-body part. Here, the modification will be performed in Ansys' Design Modeler, but it could be done in any CAD software. First of all, a plane is defined which is rotated -20° relative to the YZ-plane and then offset 5.05 [mm] in the z direction of the new plane, see Figure B.9. This new plane can then be used to define a *slice* between the stem and the head of the impactor, resulting in two separate bodies. Securing that the new mesh will be connected (nodes are shared between the stem and the head) is done by joining them in a multi-body part, see Figure B.10.

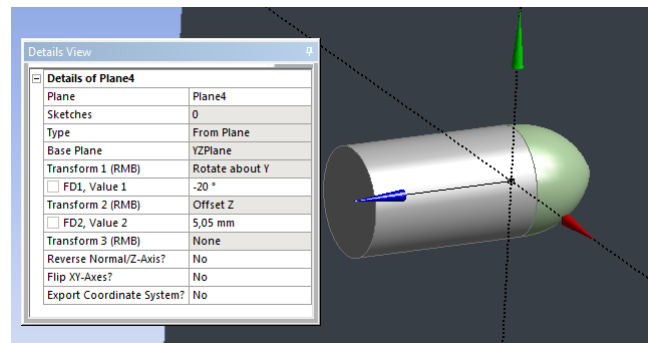


Figure B.9: New plane used to slice the impactor

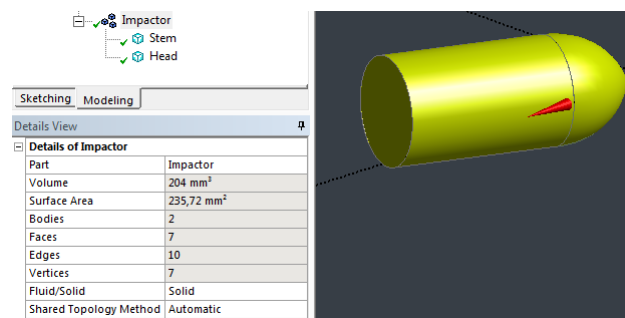


Figure B.10: Impactor defined as multi-body part

Now, the stem can be meshed independently using hexagonal elements. Using *Sweep* with a sizing of 1 [mm] generates the mesh presented in Figure B.11. This new mesh has an average element quality of 0.908 with $[min, max] = [0.815, 0.963]$.

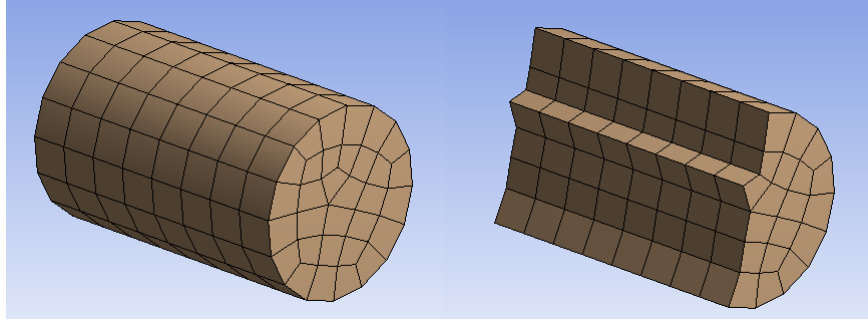


Figure B.11: *Hexagonal mesh, impactor stem*

Considering the mesh quality and mesh uniformity depicted in Figure B.11, this would be an excellent mesh to be used in an explicit analysis. However, since the stem's mesh is to be connected with the head of the impactor, which is impossible to mesh with hexagonal elements only due to its more complex shape, an evaluation of the total impactor mesh is needed. As for the mesh presented in B.8, the head is meshed using *Patch Independent* and a sizing of 1 [mm], see Figure B.12 for the resulting mesh. This mesh contains pyramid elements in the transition between the stem and the head, see Figure B.13. Pyramid elements are not supported by the explicit AUTODYN solver and will be divided up into two tetrahedral elements at the start of the analysis, resulting in small elements which will limit the maximum solver time-step and increase solve time.

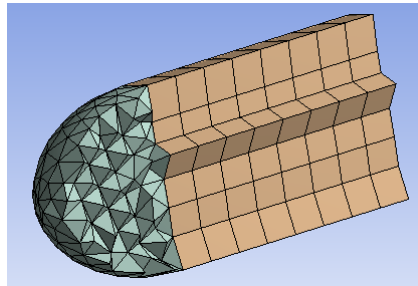


Figure B.12: *Impactor meshed with Sweep and Patch Independent methods*

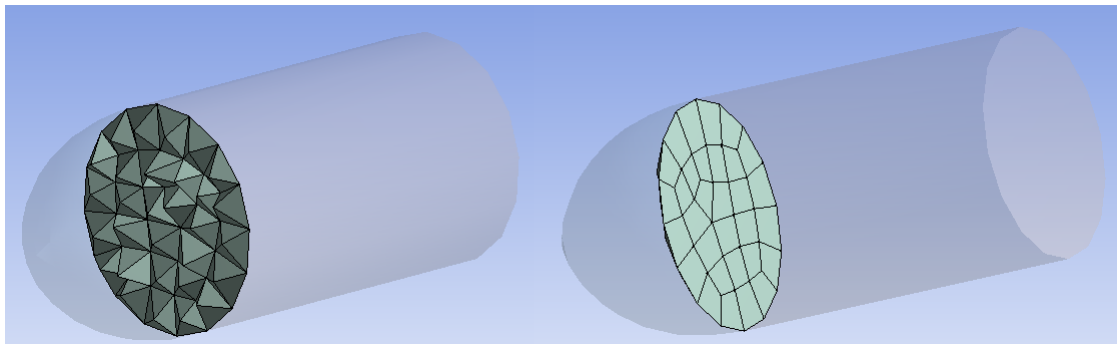


Figure B.13: *Pyramid elements*

A few pyramid elements can be countered by mass scaling (at least for LVI, see section B.2.4 or Appendix A), but here, the total amount of pyramid elements is so high that the total amount of mass added could

invalidate results. Therefore, our tracks are retraced back to the simple patch independent mesh presented in Figure B.8 (the slicing of the impactor is also undone). The ground is applied an element sizing of 1 [mm].

B.2.3 Boundary Conditions

The impactor is assigned an initial velocity defined by vector components. With an offset angle β , and an absolute velocity V , the vector components become:

$$x = -V \cos(\beta) \quad (\text{B.1})$$

$$y = V \sin(\beta) \quad (\text{B.2})$$

$$z = 0 \quad (\text{B.3})$$

Velocity components are defined using the global coordinate system, which is why the x component is negative, see Figure B.14 for the resulting vector direction.

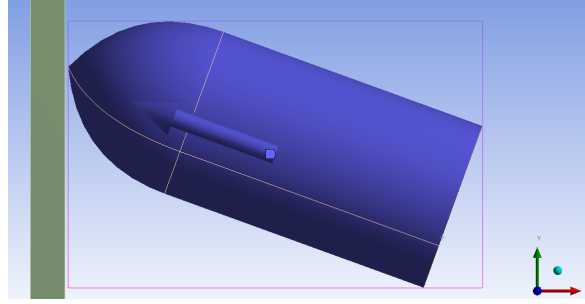


Figure B.14: *Absolute velocity direction relative to global coordinate system*

Resulting input for both the LVI (75 [m/s]) and the HVI (300 [m/s]) analyses can be seen in Table B.2 for an offset angle of $\beta = 20$ deg.

Table B.2: Velocity component input for LVI and HVI analyses

Component	LVI	HVI	Unit
x	-70.48	-281.91	[m/s]
y	25.65	102.6	[m/s]
z	0	0	[m/s]

A fixed support is applied to the four side surfaces of the plate, constraining them in all degrees of freedom, see Figure B.15.

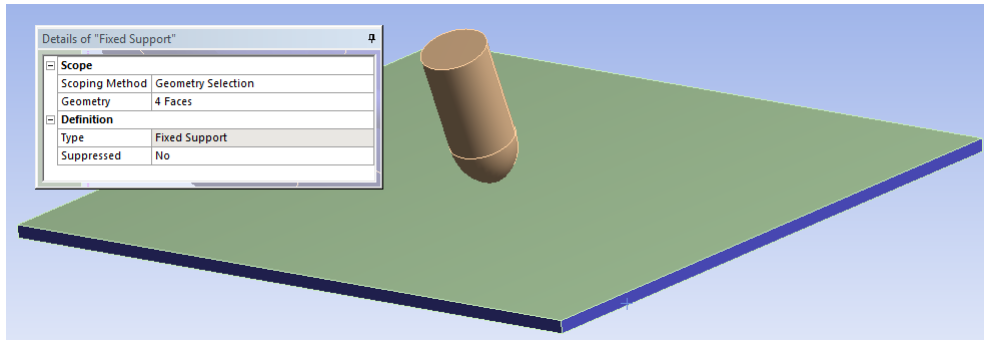


Figure B.15: *Fixed support applied to the plate*

B.2.4 Analysis Settings

Setting up the low-velocity analysis for low-velocity impact settings (analyses including velocities below $100 [m/s]$ or little deformation) requires the minimum CFL time-step to be defined prior to running the simulation (due to mass scaling being enabled). To obtain a reasonable estimate of the time-step, an iterative process of running the analysis for few cycles then evaluating added mass is performed.

First, the analysis is run with default settings (mass scaling off, focus on robustness) and the resulting time-step for all model elements evaluated. In Ansys, a user-defined result to evaluate the time-step can be applied with the expression *TIMESTEP*. Running for 20 cycles, the analysis completes almost instantly. To be certain that the time-step is stable, the Solution Output is set to *Time Increment* under Solution Information, see Figure B.16 for the result for the first 20 cycles.

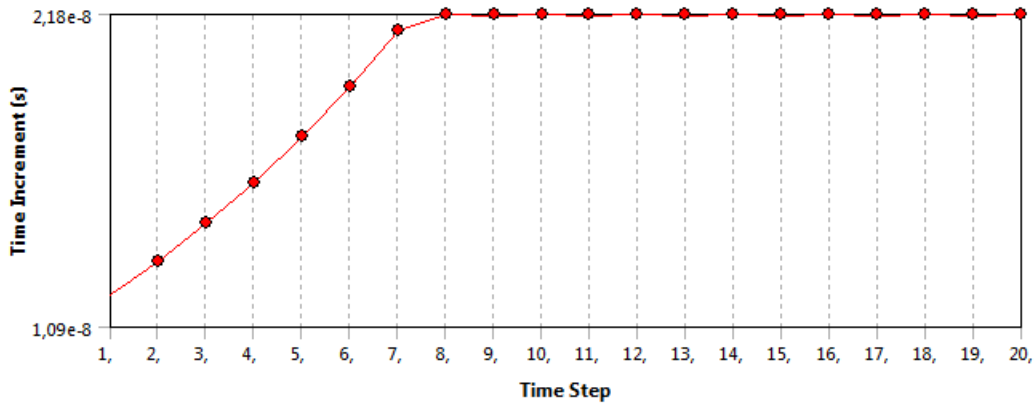


Figure B.16: *Stabilized time-step, although the horizontal axis is labeled "Time Step" it is actually cycles. Time Increment = time-step*

Stabilizing at $2.18e-8 [s]$, the time-step is rather short. Visualized results are available under the user-defined result *TIMESTEP*, see Figure B.17.

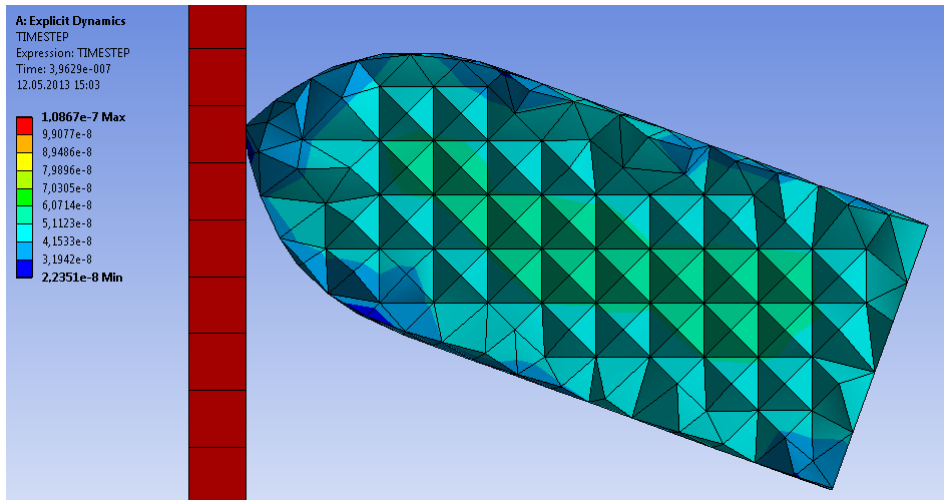


Figure B.17: *Visualized time-step, mesh. Program Controlled (default) analysis settings*

Total added mass can be evaluated by opening the file **admodel.prt** which is created by the Autodyn solver. Setting the time-step to $4e-8 [s]$ adds $0.121 [g]$ to the impactor which corresponds to 7.7% total mass added for the impactor, see Figure B.18. Since the impactor represents the kinetic energy which is imposed onto the plate, an additional 7.7% might be too big of an increase. Had it been 7.7% added to a part which was not subjected to any high accelerations, it could have been acceptable. It will always be up to the analyst

to decide if the amount of added mass is acceptable or not, here the time-step is reduced to $3.5e - 8$ [s] which corresponds to a mass increase of 2.73%.

MASS SCALING SUMMARY BY PART				
PART	MASS	ADDED MASS	TOTAL MASS	%ADDED
Plate	1.962E+04	0.000E+00	1.962E+04	0.000E+00
Impactor	1.571E+03	1.210E+02	1.692E+03	7.699E+00
<hr/>				
TOTALS	2.120E+04	1.210E+02	2.132E+04	5.707E-01

Figure B.18: Total mass added at a time-step of $4e - 8$ [s]

It is also possible to visualize the mass scaling by defining a user-defined result with the expression *MASS_SCALING*. The resulting mass scaling for a defined time-step of $3.5e - 8$ [s] can be seen in Figure B.19.

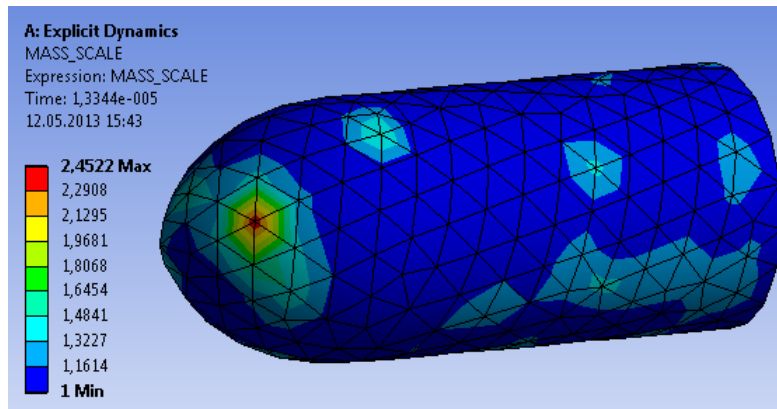


Figure B.19: Total mass scaling at a time-step of $3.5e - 8$ [s]

Recommended (by Ansys) settings are applied for both the LVI and HVI analyses, see Figure B.20.

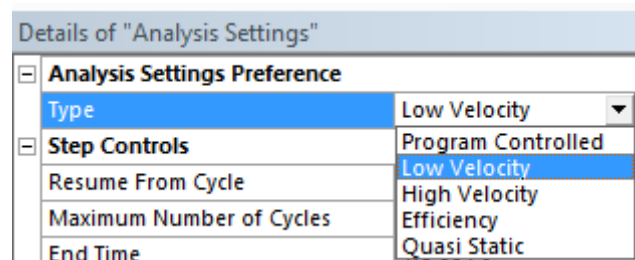


Figure B.20: Pre-defined settings by Ansys

Appendix A, section A.2.6 contains a more in-depth discussion of key controller differences between LVI and HVI. The pre-defined settings for HVI does not require any user-input. Key differences between Low Velocity and High Velocity Analysis Settings are presented in Table B.3 (Ansys 2013):

Table B.3: Analysis Settings for Low and High Velocity

Analysis Settings	Low Velocity	High Velocity
Mass Scaling	Yes	No
Hex Integration Type	1pt Gauss	Exact
Tet Integration	Nodal Based Strain	Average Nodal Pressure
Hourglass Damping	Flanagan Belytschko	AUTODYN Standard
<i>Erosion Controls</i>		
On Geometric Strain Limit	No	Yes
Geometric Strain Limit	Unchanged	1.5
<i>Body Interaction</i>		
Body Self Contact	No	Yes
Element Self Contact	No	Yes

From Table B.3, it is possible to identify some general trends in differences between LVI and HVI. Firstly, based on the differences in mass scaling and Hex integration type, LVI settings could be perceived as less accurate than HVI settings. Why mass scaling is applied for LVI but not for HVI is easy to imagine; LVI inherently includes lower velocities than HVI, which in turn means lower kinetic energy for the same mass (kinetic energy is proportional to the mass and velocity squared, $T = \frac{1}{2}mV^2$). This reduction in kinetic energy allows for small changes in mass without influencing the results as much as for analyses with higher velocities.

As discussed in Appendix A, section A.2.6, the Flanagan-Belytschko hourglass damping settings are invariant for rigid-body rotation, which possibly could be more common for LVI than for HVI. Imaginably, lower velocities (and thus significantly lower kinetic energies), would make impactors more prone to ricocheting off of the target, and thus entering a state of rigid-body rotation, instead of penetrating it.

Calculating body self contact, and even element self contact, could seem redundant for LVI analyses where such large deformation is less likely than for HVI. HVI problems on the other hand could include severe body deformations, ending in the body coming into contact with itself.

The LVI analysis is set to run for 0.00024 [s], while the end time of the HVI analysis is set to 0.0001 [s]. As mentioned earlier, when choosing the pre-defined High-Velocity settings in Ansys, no user-defined input is needed.

B.3 Post-Processing

Here, the post-processing of the LVI and the HVI analyses are presented, and the results evaluated, separately, starting out with the LVI.

B.3.1 Low-Velocity Impact (LVI)

Before the strains and stresses are controlled, the validity of the results must be investigated. One easy and basic way of doing this is to check the Energy Summary and Energy Conservation under Solution Information. Firstly, the Energy Summary shows a relatively high presence of Hourglass Energy, as can be seen in Figure B.21.

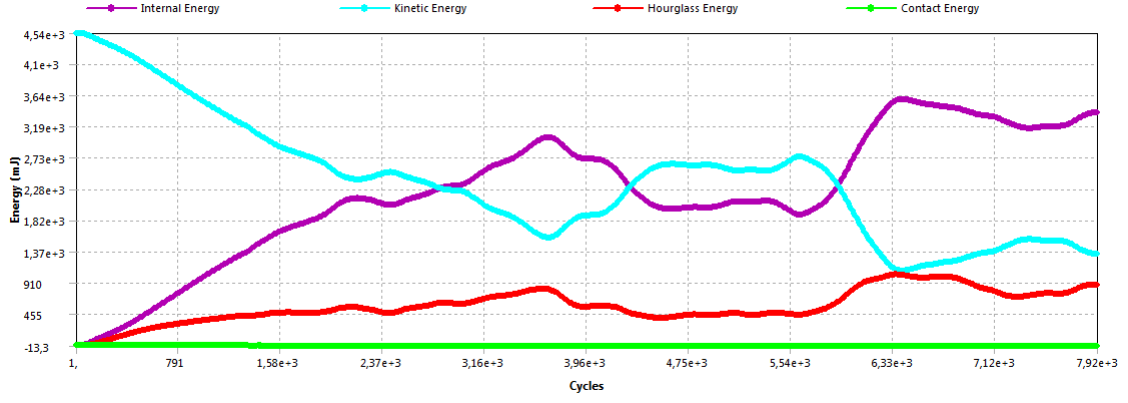


Figure B.21: *Energy Summary for the Low-Velocity Impact analysis*

Energy Conservation will provide, among other information, the Energy Error. In Ansys, the energy error is defined as:

$$R = [I + K + H] \text{ at reference cycle} \quad (\text{B.4})$$

$$C = [I + K + H] \text{ at current cycle} \quad (\text{B.5})$$

$$W = W_l + W_c + W_{cpf} + W_{bf} + E_e \quad (\text{B.6})$$

$$E = \frac{|C - R - W|}{\max(|C|, |R|, |K|)} \quad (\text{B.7})$$

Where:

- R - Reference Energy
- I - Internal Energy
- K - Kinetic Energy
- H - Hourglass Energy
- W - Work Done
 - W_l - Work done by loads
 - W_c - Work done by constraints
 - W_{bf} - Work done by body forces
 - W_{cpf} - Work done by contact penalty forces
 - E_e - Energy removed by element erosion
- E - Energy Error

From Figure B.22, which depicts the Energy Conservation for the LVI analysis, it is clear that as the impactor starts to ricochet off of the plate, the energy error increases. Comparing Figure B.21 and Figure B.22

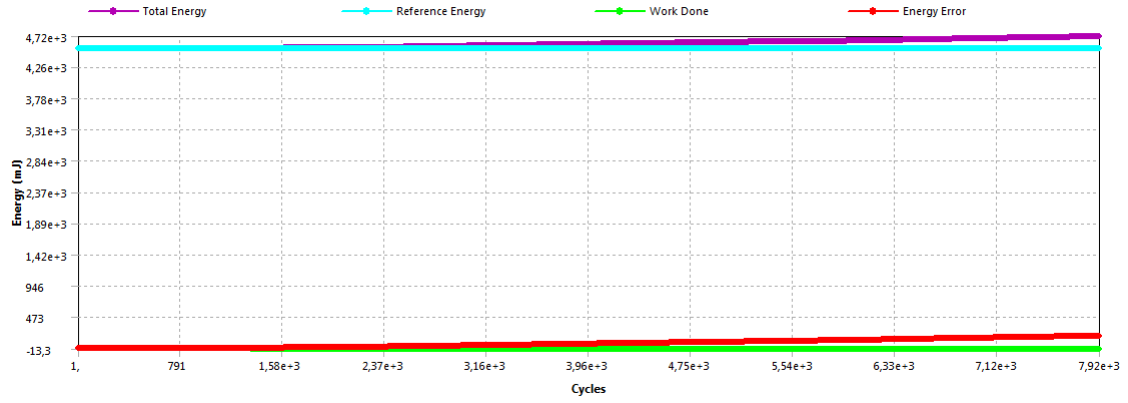


Figure B.22: *Energy Conservation, LVI*

Comparing Figure B.21 and Figure B.22, it is possible to conclude that it is the rise in Total Energy, which increases due to an increase in Hourglass Energy (Contact Energy and Work Done is approximately zero, and constant), that leads to the increase of the Energy Error. From this, means to reduce Hourglass Energy could be applied to increase solution validity. Appendix A, section A.3.2, lists three possible means to reduce Hourglass Energy (Lauth 2013):

- Refine the mesh
- Avoid point/line contacts
- Change hourglass damping controls to Flanagan-Belytschko (if not already applied)

Here, there are no point/line contacts, and Flanagan-Belytschko hourglass damping controls are already applied. Therefore, an attempt to refine the mesh will be made. Reducing the element size from 1 [mm] to 0.8 [mm] for both the impactor and the plate, severely increases the amount of elements/nodes in the model and prolongs solution time by roughly 3 [min] from approx. 2.2 [min] to 5.25 [min] (which may be a short absolute time duration, but the solution time is more than doubled compared to previous analyses).

Studying the new graphs for Energy Conservation, Figure B.23, and Energy Summary, Figure B.24, the difference from the pre mesh-refinement analysis is clear: Hourglass Energy has been drastically reduced, and the plots for Internal, Kinetic, and Hourglass Energy are smoother. The increasing Energy Error have also been severely reduced to an, almost, horizontal line.

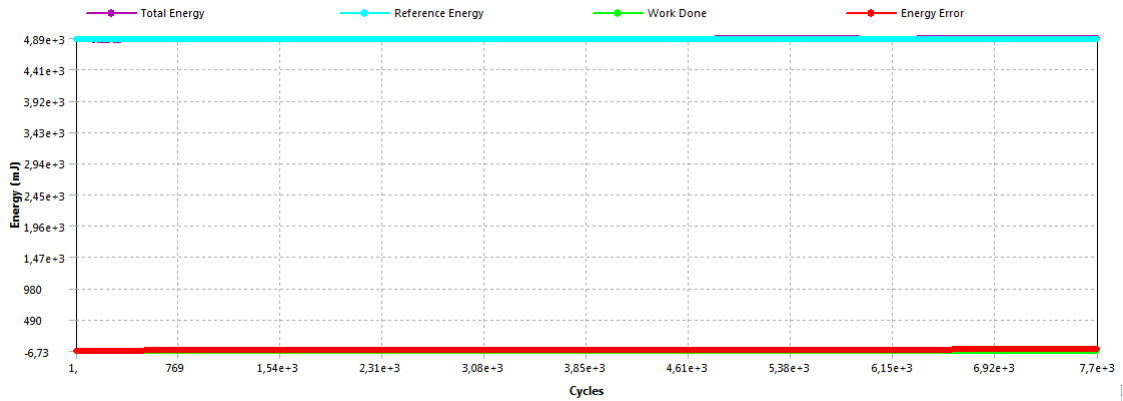


Figure B.23: *Energy Conservation, LVI, after mesh refinement*

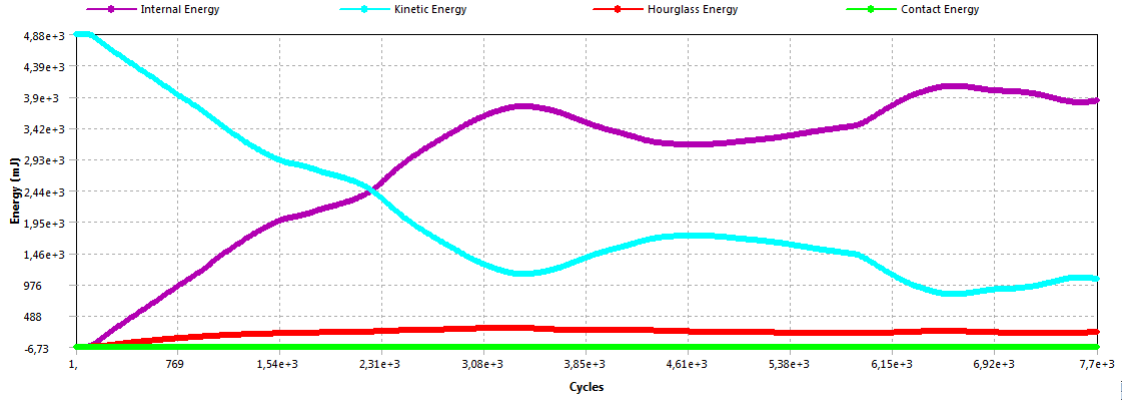


Figure B.24: *Energy Summary for the Low-Velocity Impact analysis after mesh refinement*

For isotropic materials, equivalent stress (von-Mises) and equivalent plastic strain are the most common results for post-processing. The displacement of both the plate and the impactor can be seen in Figure B.25.

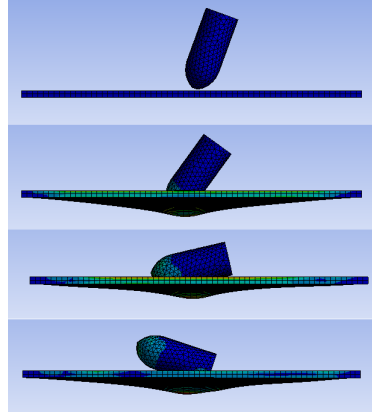


Figure B.25: *Displacement Low-Velocity Impact analysis, contours are non-uniform, equivalent stress*

B.3.2 High-Velocity Impact (HVI)

As for the LVI case, the Energy Summary and Energy Conservation plots are checked before results are evaluated. Energy Summary for the HVI case can be seen in Figure B.26, and the Energy Conservation for the HVI case can be seen in Figure B.27. Notice the disturbance in Internal Energy around cycle 1500 in Figure B.26, and the drop in total energy at the same time in Figure B.27. This behaviour is due to the impactor penetrating the plate, resulting in a loss of internal energy which is transferred into the Work Done category, see equation (B.6). Figure B.29 depicts the penetration of the plate. Since both the Energy Error and the level of Hourglass Energy is relatively low, results are considered to be of good quality.

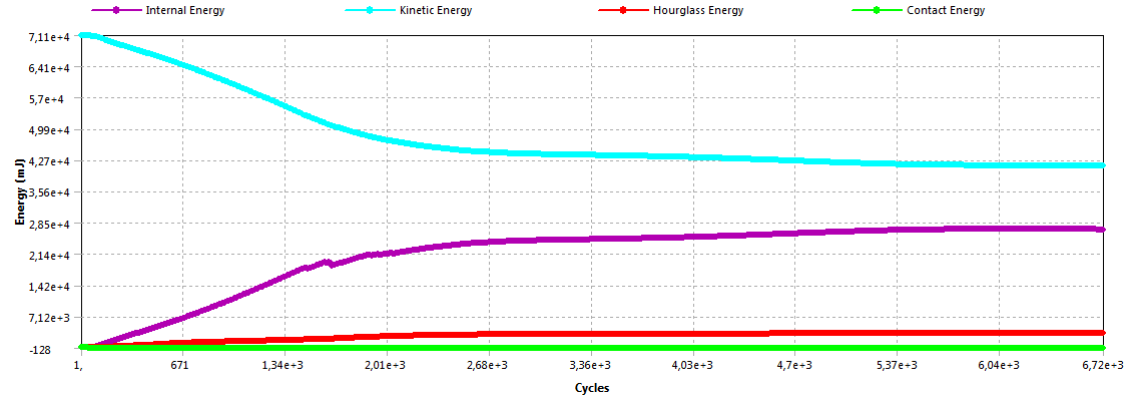


Figure B.26: *Energy Summary of the HVI analysis*

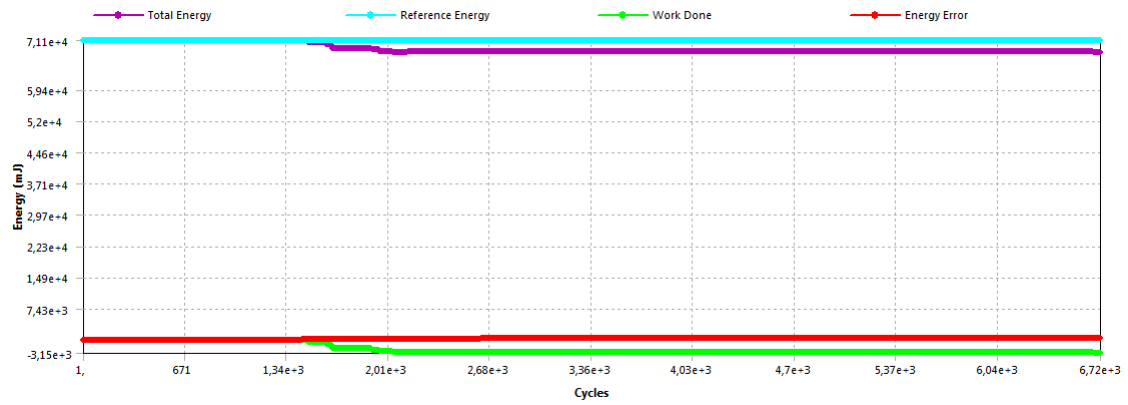


Figure B.27: *Energy Conservation of the HVI analysis*

Propagation of stress waves are central for explicit analyses, and both the elastic front of a stress wave and the secondary plastic portion of it can be central for results evaluation. In Ansys, equivalent elastic strain and equivalent plastic strain depicts this two-part wave propagation, which can be seen in Figure B.28 for the HVI case at the time $t = 2e - 6$ [s].

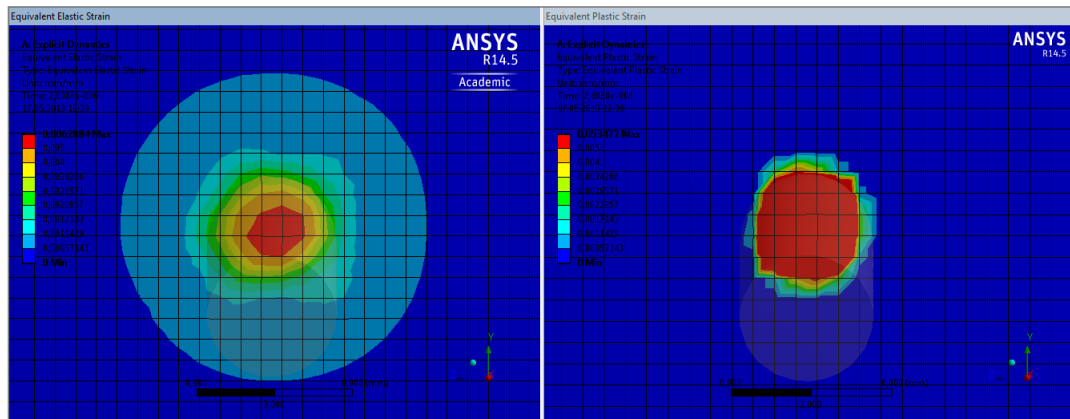


Figure B.28: *Left: Elastic Strain Right: Plastic Strain, contours are uniform, i.e. same scale*

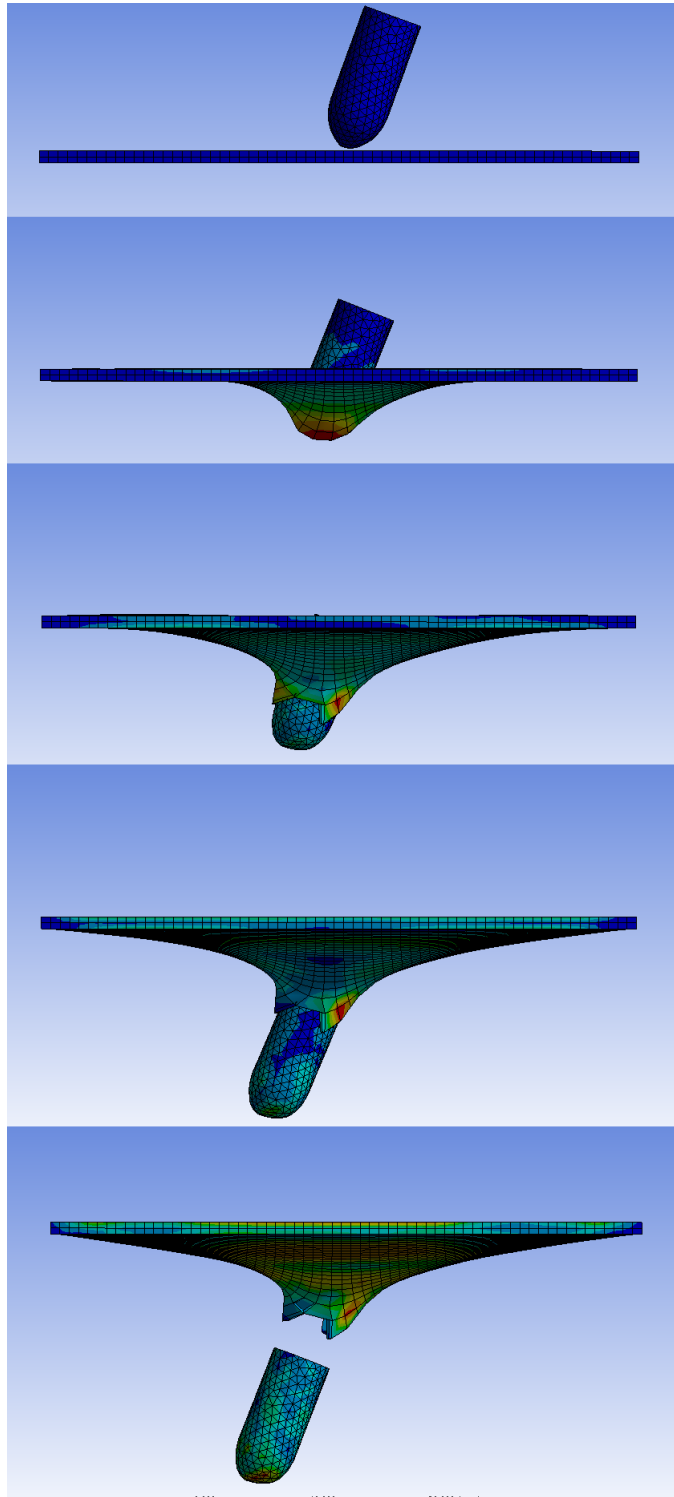


Figure B.29: *Penetration of plate, contours are non-uniform*

C Defining Composites in ACP (pre)

In this appendix you will find a more detailed description of the process of defining composite laminates in the ACP (pre) environment. The purpose of this appendix is twofold, firstly to complement the Method chapter in the main body of this thesis, and secondly to provide a reference for anyone learning to use ACP or replicating this thesis. Step-by-step, the process of preparing the Sandwich concept for analysis is presented, starting from the imported mesh with defined named selections as described in the Method chapter. The preparation of the Multiframe concept is not included as it is very similar to that of the Sandwich Skin concept.

C.1 Creating Fabrics and Verifying Imported Data

Firstly, after importing the mesh, the named selections were verified as shown in Figure C.1. In ACP, the named selections are divided into two separate groups; Element Sets (named selections consisting of surfaces) and Edge Sets (named selections consisting of edges). All Element Sets were verified to have imported correctly, but some of the Edge Sets had not been fully replicated. In Figure C.2, two Edge Sets are shown which were supposed to be of equal length. All short imported Edge Sets were extended by creating new user-defined Edge Sets by selecting nodes as shown in Figure C.3. Please note that for these edge sets to be defined, the mesh needs to be created in such a way that nodes are placed along the edges. Using Virtual Topology, although possibly simplifying meshing, could remove such edges, thus invalidating the edge set importation or even severely complicating manual definition of Edge Sets, resulting in a poorly described reference fiber orientation.

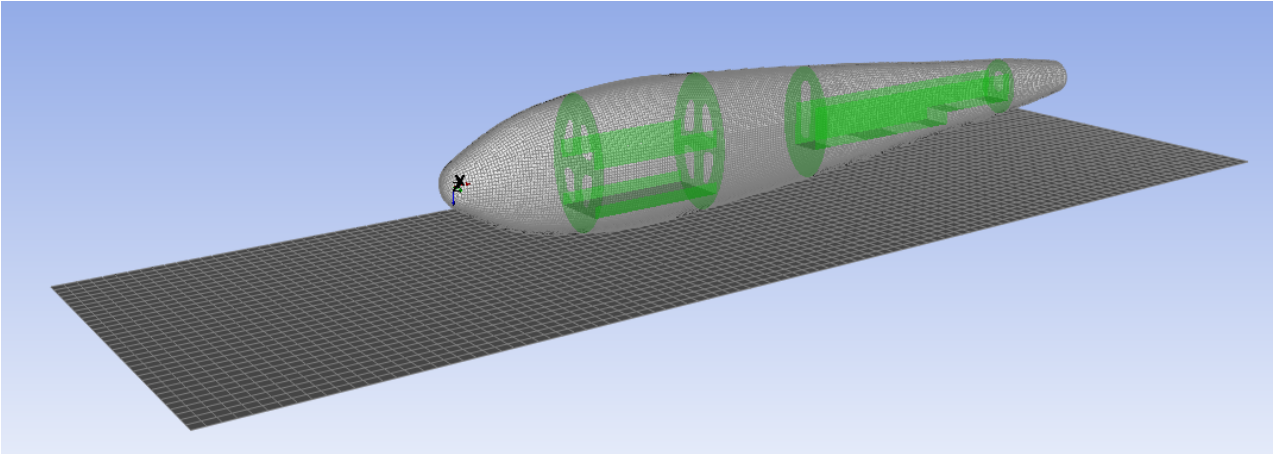


Figure C.1: *Imported mesh with the frame named selections highlighted*

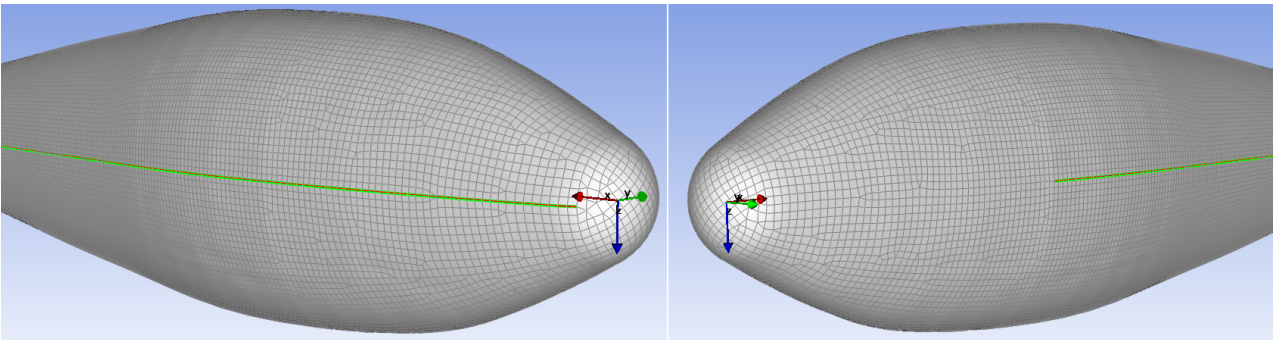


Figure C.2: *Left: Correctly imported Edge Set Right: Too short imported Edge Set*

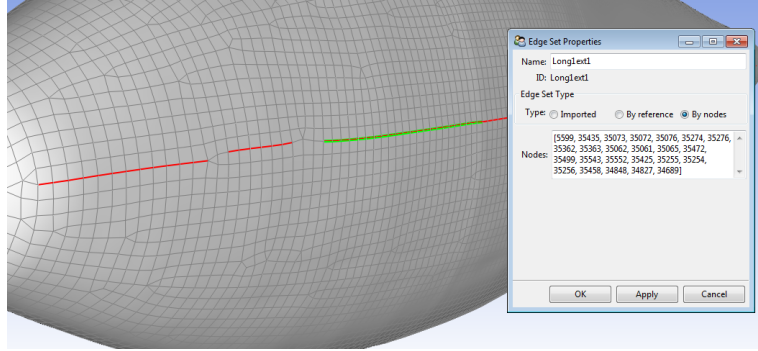


Figure C.3: *Extension of Edge Set by manually selecting nodes. The added edge sets are actually divided up into four separate sets.*

If the edge sets had not been manually extended, the oriented element set for the skin, which determines the reference direction for the fibers, would have contained a faulty reference direction in the area where the edge sets were lacking. See Figure C.4 for a comparison between the reference direction prior to and after extending edge sets.

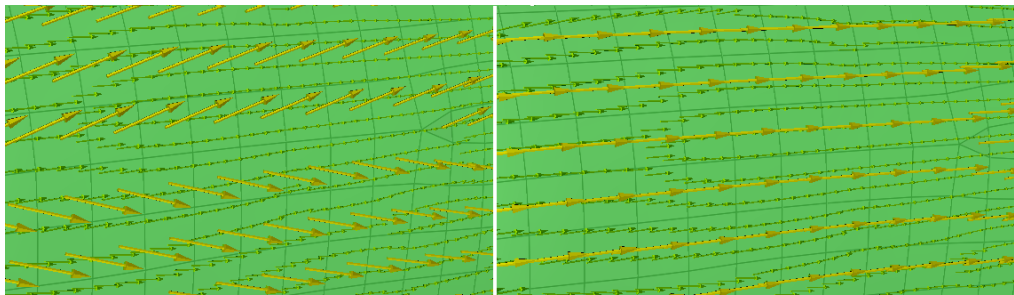


Figure C.4: *Fiber reference direction for the skin. Left: Prior to extending edge set. Right: After extending edge set*

Forming the basis of material definition, fabrics were created using the materials created in the Engineering Data component in Ansys workbench (imported into ACP (pre) along with the rest of the relevant model data). When defining the fabrics, a thickness was applied to each fabric. This meant that for bodies that consisted of the same material, but had different thicknesses, a fabric had to be defined for each body. Ideally, this would not be an issue as all composite prepreps are delivered with a specific ply thickness, but since isotropic materials were used in this model several fabrics had to be defined with different thicknesses. In Figure C.5, the fabric definitions for the composite material and the frame material is presented.

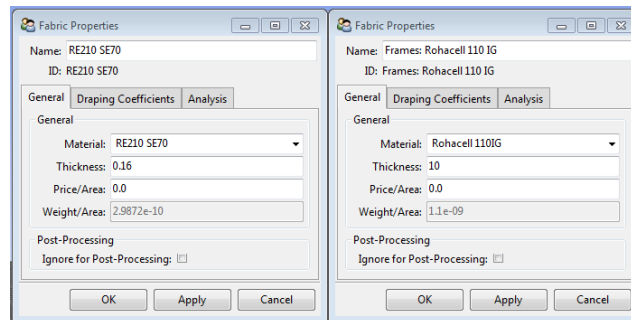


Figure C.5: *RE210 SE70 and Rohacell 110 IG fabric definition*

C.2 Importing CAD Geometry for Cutoff Rule

Since thickness was applied normal to the simplified surfaces of the frames, care had to be taken to ensure the applied frame thickness did not penetrate the skin. To solve this problem, CAD geometry can be imported into ACP to generate cutoff rules used to taper and cut plies that come into conflict with the CAD geometry. However, using the inner surface, as a continuous body, of the skin to represent the cutoff geometry did not work, and several cutoff geometries had to be saved as STEP files and imported into the ACP environment. One cutoff surface was imported for each area that could possibly come into conflict with the skin, with each one being based on the inner surface of the skin. In Figure C.6, the cutoff geometry for the floor of the frames can be seen. To apply the cutoff geometry, a rule was generated for each cutoff as can be seen in Figure C.7. These rules were later activated when creating plies, see section C.4. An exaggerated (40 [mm] instead of 10 [mm] thickness applied) result of plies cut by the imported geometry can be seen in Figure C.8.

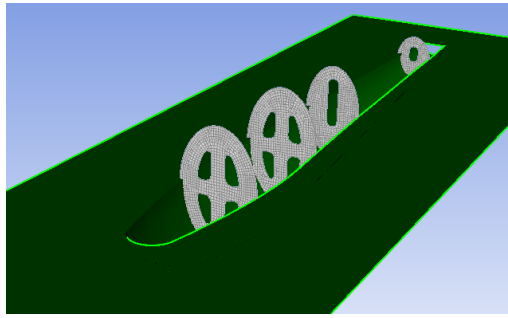


Figure C.6: *Cut-off geometry for the floor of the frames. Please note that even though it looks like the frame element sets are in conflict with the CAD geometry, they really are not.*

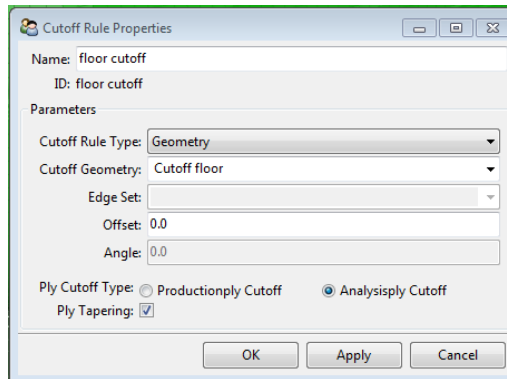


Figure C.7: *Cutoff rule for frame floors*

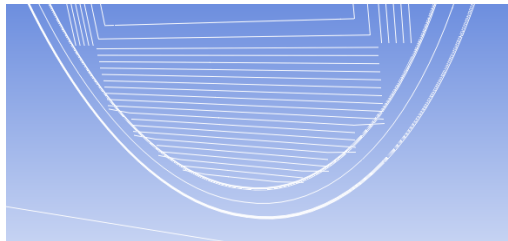


Figure C.8: *Payload frame floor cut off by imported geometry, visualized using a section cut*

C.3 Rosettes and Oriented Element Sets

Rosettes are used in Oriented Element Sets to control the reference fiber direction of plies. All bodies except the skin (including the aft section) consisted of isotropic materials, therefore rosettes were only defined for the skin. Other bodies relied on the default rosette (global coordinate system). Using the successfully imported and manually defined Edge Sets, Edge Wise rosettes were created, see Figure C.9. Since the aft section was defined in a separate Element Set, a parallel rosette with the z-direction normal to the Element Set was created.

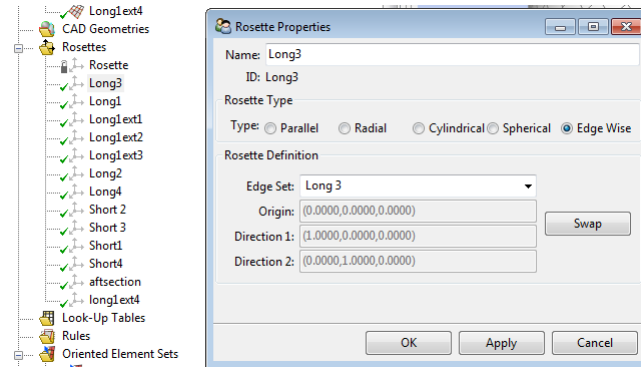


Figure C.9: *Rosettes for skin laminate*

Oriented Element Sets combine rosettes and Element Sets into sets with reference and orientation directions, and are used to define plies' 0 deg direction and layup orientation. For the skin, all of the rosettes based on Edge Sets, the Element Set containing skin elements, and an arbitrary orientation point on the skin with the orientation direction pointing *outwards* from the payload/batteries were selected to create the Oriented Element Set. Selections for the skin Oriented Element Set can be seen in Figure C.10 along with the reference direction (yellow arrows) and the orientation direction (purple arrows). Rosette selection method was set to Minimum Distance so that the rosette closest to the element was used to define the reference direction.

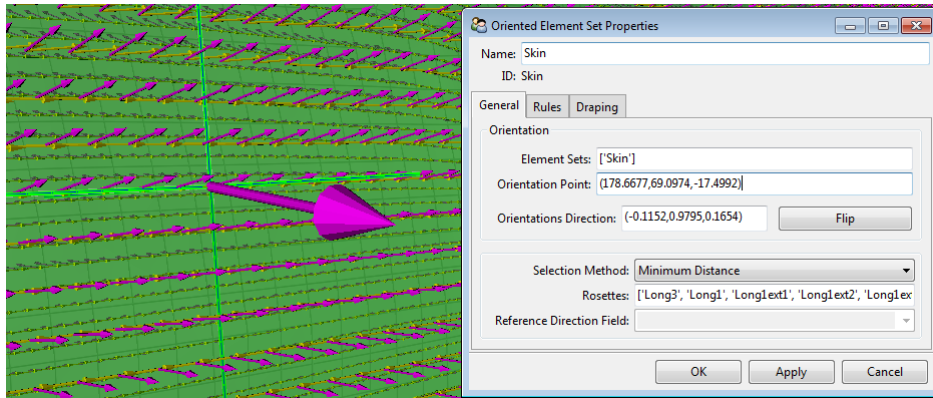
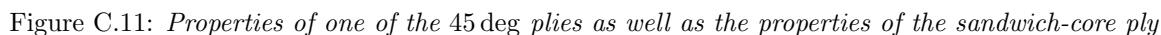


Figure C.10: *Oriented Element Set selection and result for the skin*

The Oriented Element Set for the aft section was defined using the parallel rosette and an arbitrary rosette selection method (only one selected rosette). Oriented Element Sets based on surfaces created using a "Surface from faces" option in Design Modeler (the ground, frame, batteries, and payload (el. cabinet) surfaces) were created in such a way that the orientation direction (the direction where thickness would be applied) did not come into conflict with other bodies.

For the skin Modeling Ply group, five plies on each side of the core were created with the stacking sequence $[45, -45, 45, -45, 45]$. Not being a sandwich element, the aft section was modeled the same way as the skin for the Multiframe concept; nine plies with the stacking sequence $[45, -45, 45, -45, 45, -45, 45, -45, 45]$. In Figure C.11, the properties for a 45 deg ply is shown along with the properties of the core ply, also visible is the grouping of both the Skin Modeling Ply group and the Aft section Modeling Ply group.



Cutoff rules were added during the definition of plies that could come into conflict with other plies. In the properties window, the tab "Rules" was selected and the appropriate cutoff rule chosen. The resulting table for the floor ply of the payload frame can be seen in Figure C.12.



D Orthotropic Constants Study

This Appendix contains test settings and geometry definition for the orthotropic constants study described in Chapter 3, Method. The composite plate and impactor were modeled in the Design Modeler environment, native in Ansys Workbench, as surface bodies. Thickness and stacking sequence was defined in a ACP (pre) system (see Appendix C for more information about ACP (pre)).

In Figure D.1, the measurements of the plate and impactor is presented.

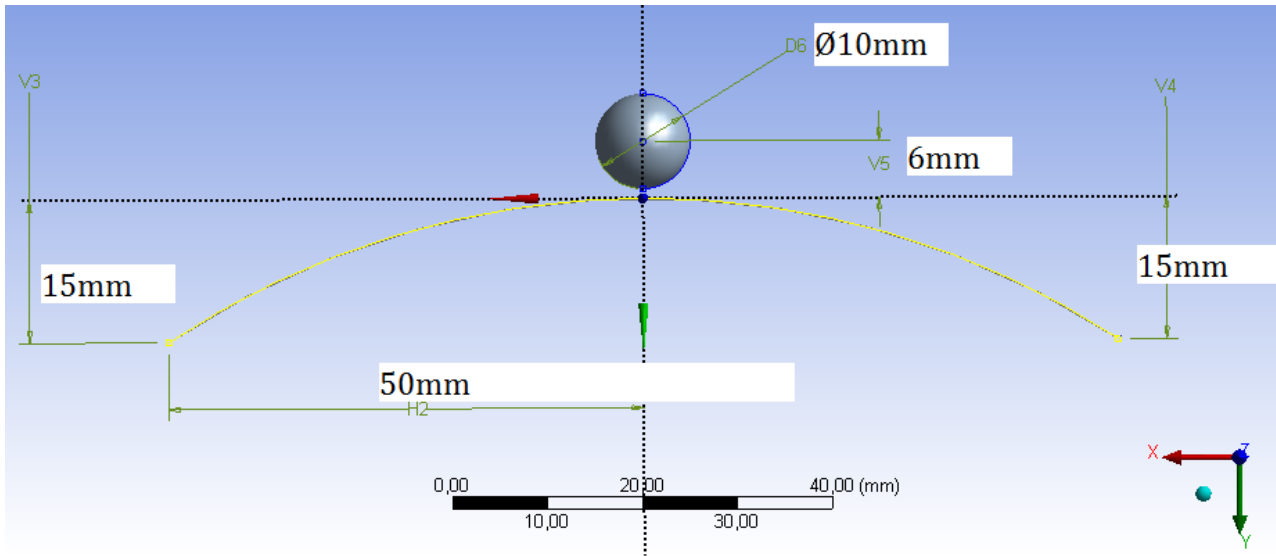


Figure D.1: *Dimensions for both the plate and the spherical impactor*

The plate was meshed using *Mapped Face Meshing* and a sizing of 4 [mm], while the spherical impactor was meshed using *Quadrilateral Dominant* and a sizing of 2 [mm]. Plate thickness was applied towards the impactor, five plies of 0.16 [mm]. See Chapter 3 for material parameters (RE210 SE70 unbalanced woven fiberglass prepreg). Thickness for the impactor was applied towards its center, *away* from the plate with a thickness of 0.5 [mm]. It was modeled using linear structural steel; $E = 210$ [GPa], $\nu = 0.3$, and $\rho = 7850$ [kg/m³], and set to *Rigid*.

In Ansys Mechanical, the impactor was given an initial velocity of 7.5 [m/s] towards the plate, default analysis settings were used and the duration was set to 0.5 [ms]. A fixed support (locking all dof) was applied to the two horizontal edges of the plate. Results were post-processed using a *Equivalent Stress* (von-Mises) result, set to *Entire Section* and *Top/Bottom*. An example output is given in Figure D.2.

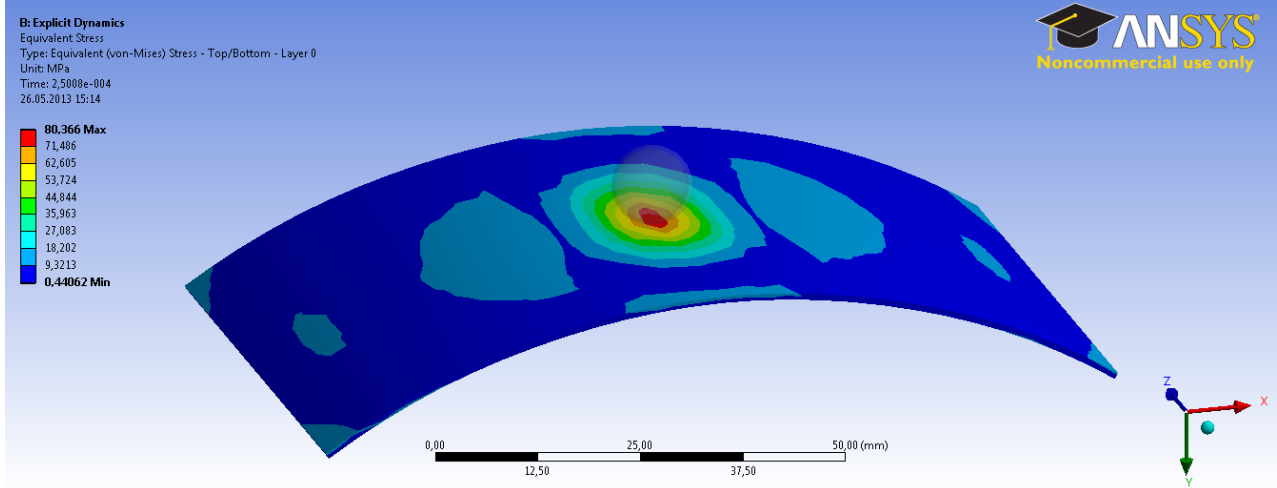


Figure D.2: *Max equivalent stress at $t = 0.25$ [ms], test 1*

Results for all ten test cases are given in Table D.1.

Table D.1: Test settings and results

Test	E_z [GPa]	ν_{yz}	ν_{xz}	Max eq. stress [MPa]
1	0.001	0.001	0.001	80.4
2	10	0.001	0.001	80.4
3	10	0.1	0.001	80.4
4	10	0.1	0.1	80.4
5	20	0.1	0.1	80.4
6	20	0.499	0.1	78.9
7	20	0.499	0.499	99.4
8	0.001	0.499	0.499	80.4
9	0.001	0.001	0.499	80.4
10	10	0.122	0.122	80.4

E Stacking Sequence Test Results

This appendix contains results of the stacking sequence testing. Firstly, plots of maximum von-Mises stress are presented, followed by maximum and minimum principal stresses, maximum shear stress, and lastly, gradual failure for each stacking sequence is represented by figures depicting material erosion.

Maximum von-Mises Stress

In Figure E.1, the maximum von-Mises stress for the five stacking sequences are shown.

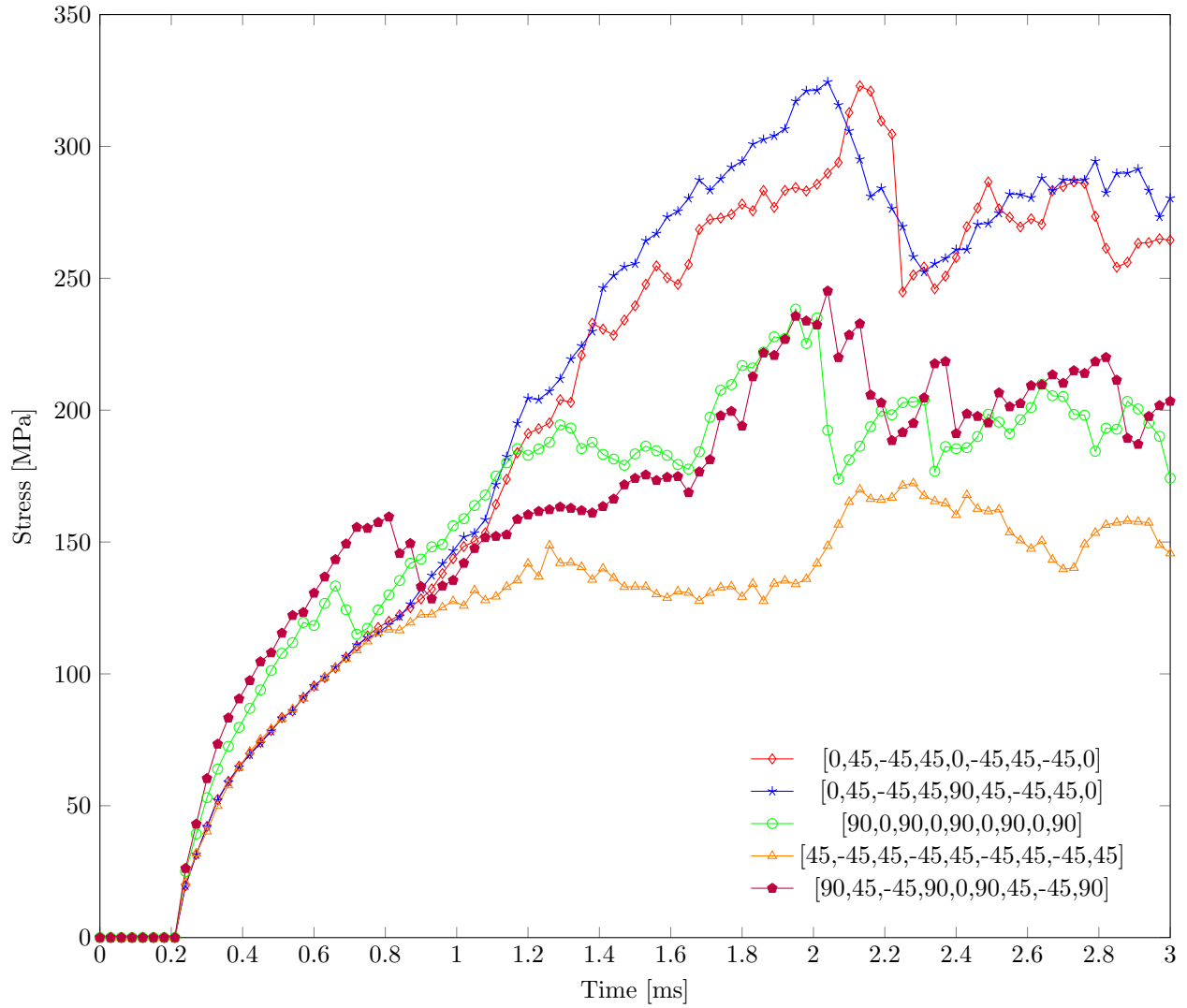


Figure E.1: *Maximum von-Mises stress for five different stacking sequences*

Maximum Principal Stress

In Figure E.2, the maximum principal stress, σ_1 , for the five stacking sequences are shown.

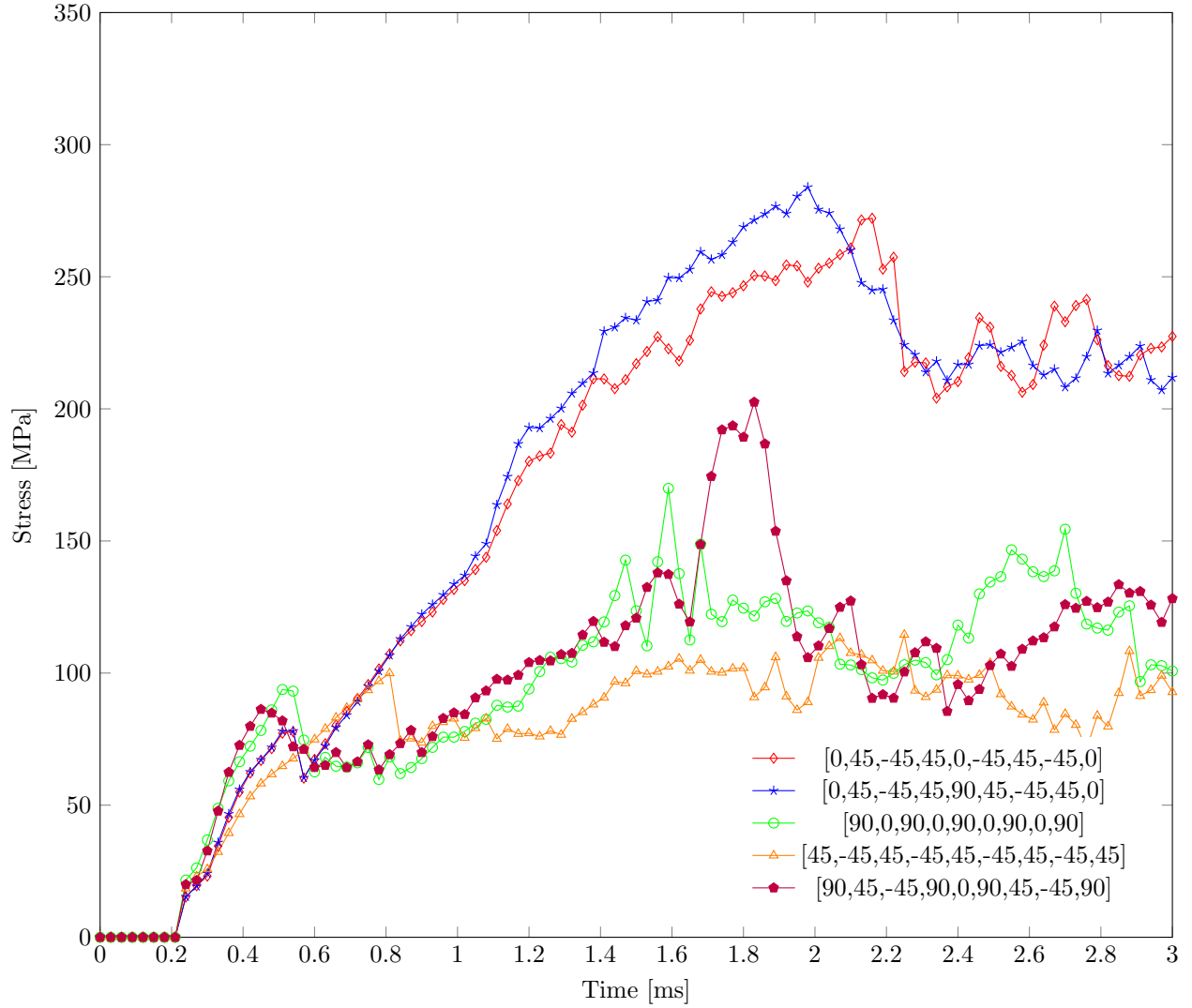


Figure E.2: *Maximum Principal stress for five different stacking sequences*

Minimum Principal Stress

In Figure E.3, the minimum principal stress, σ_3 , for the five stacking sequences are shown.

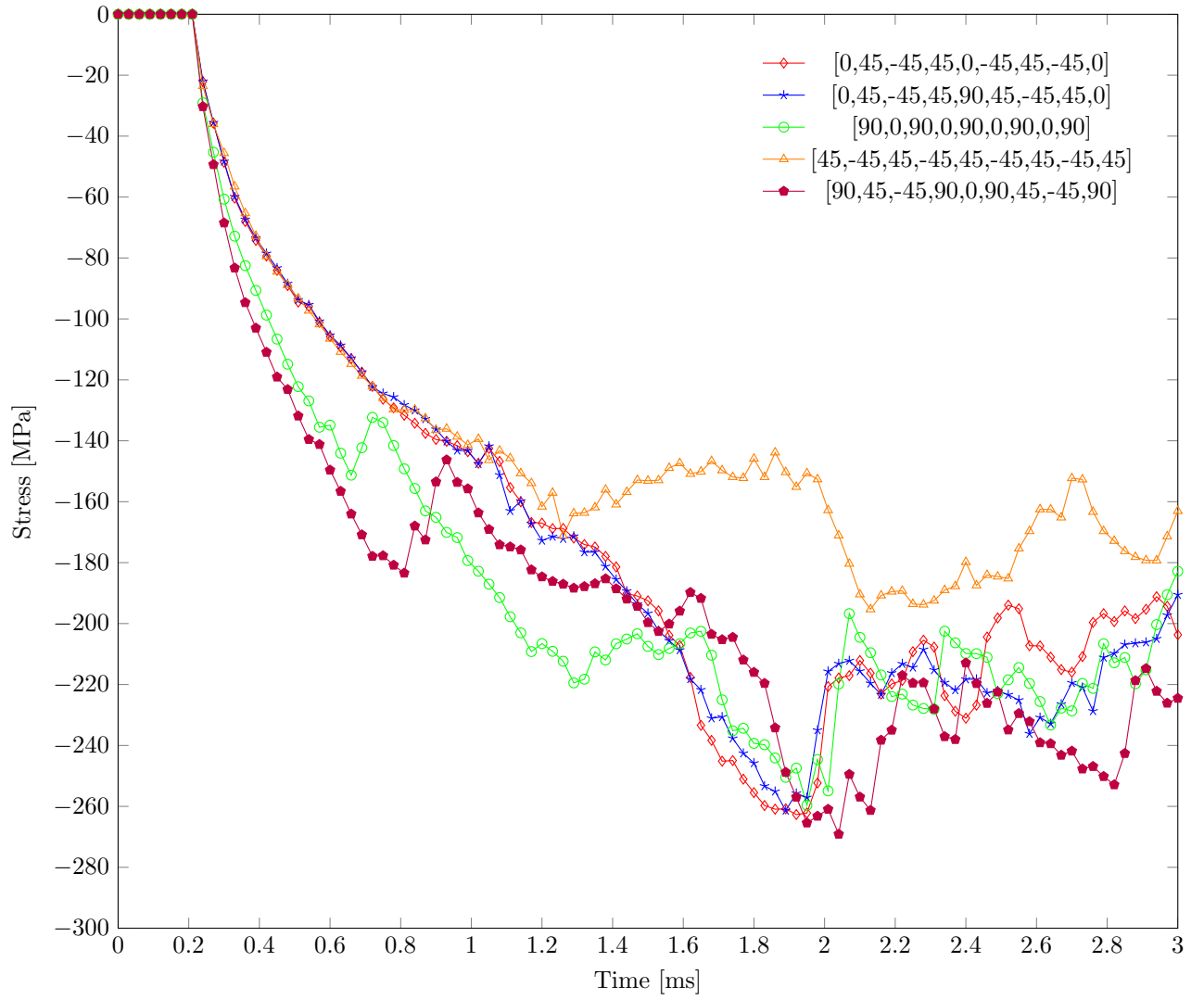


Figure E.3: *Minimum Principal stress for five different stacking sequences*

Maximum Shear Stress

In Figure E.4, the maximum shear stress for the five stacking sequences are shown.

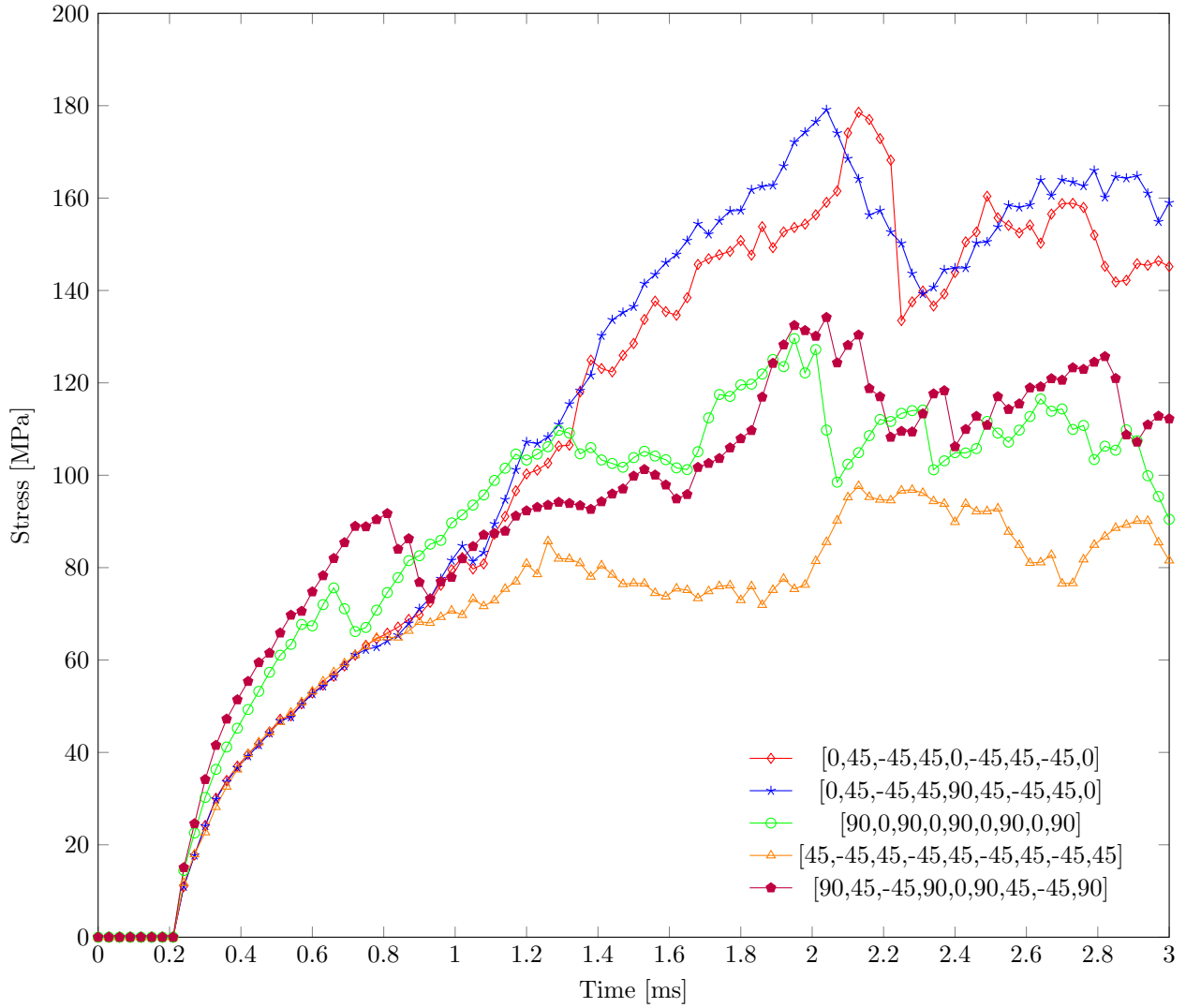


Figure E.4: *Maximum Shear stress for five different stacking sequences*

Gradual Failure Plots

All plots presented here have been generated using the user-defined result *STATUS* in Ansys mechanical, with the innermost ply selected (#9). Red elements represent reported failure according to the Tsai-Wu failure criterion for orthotropic materials.

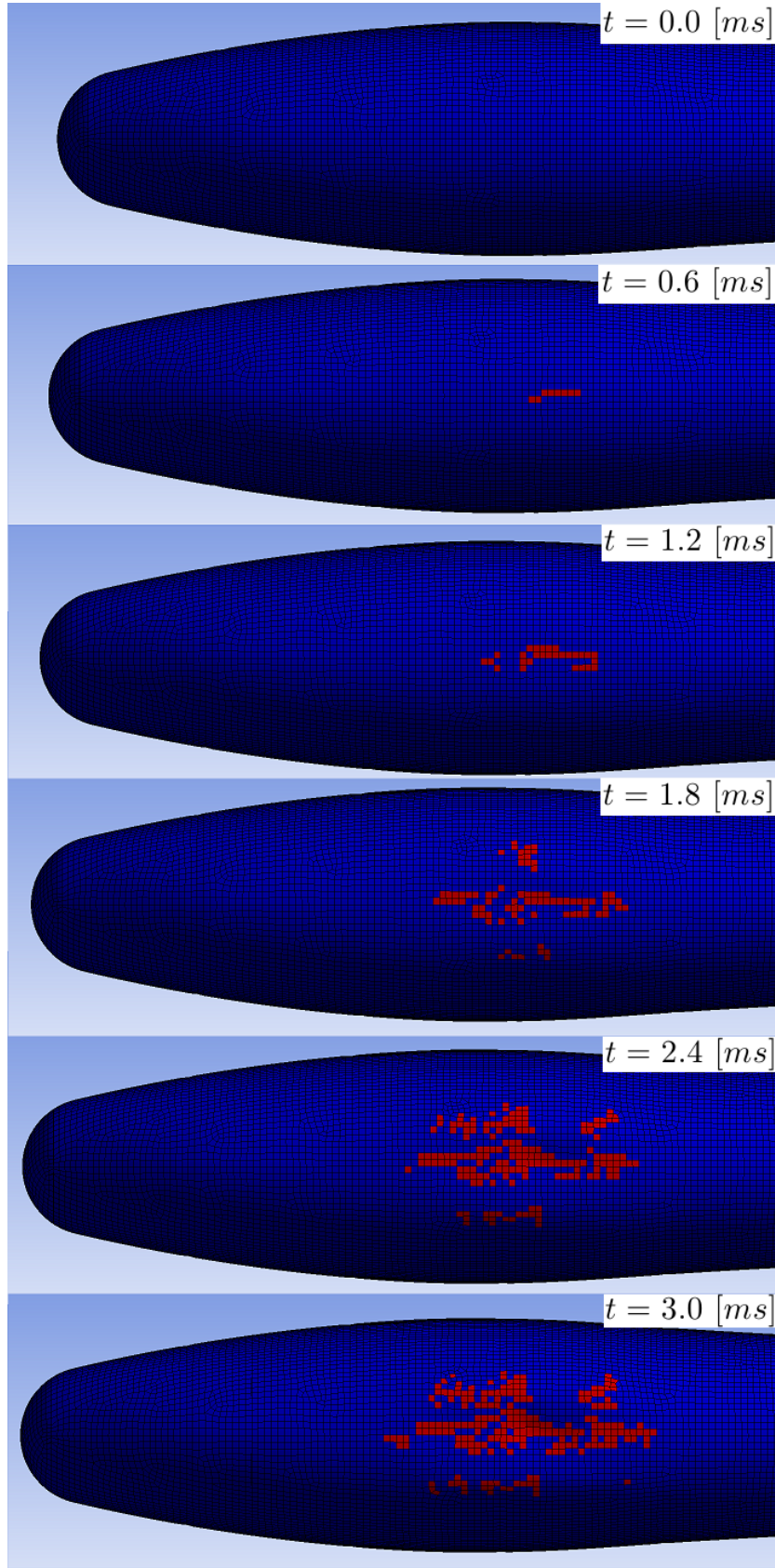


Figure E.5: *Gradual failure for the $[0, 45, -45, 45, 0, -45, 45, -45, 0]$ stacking sequence*

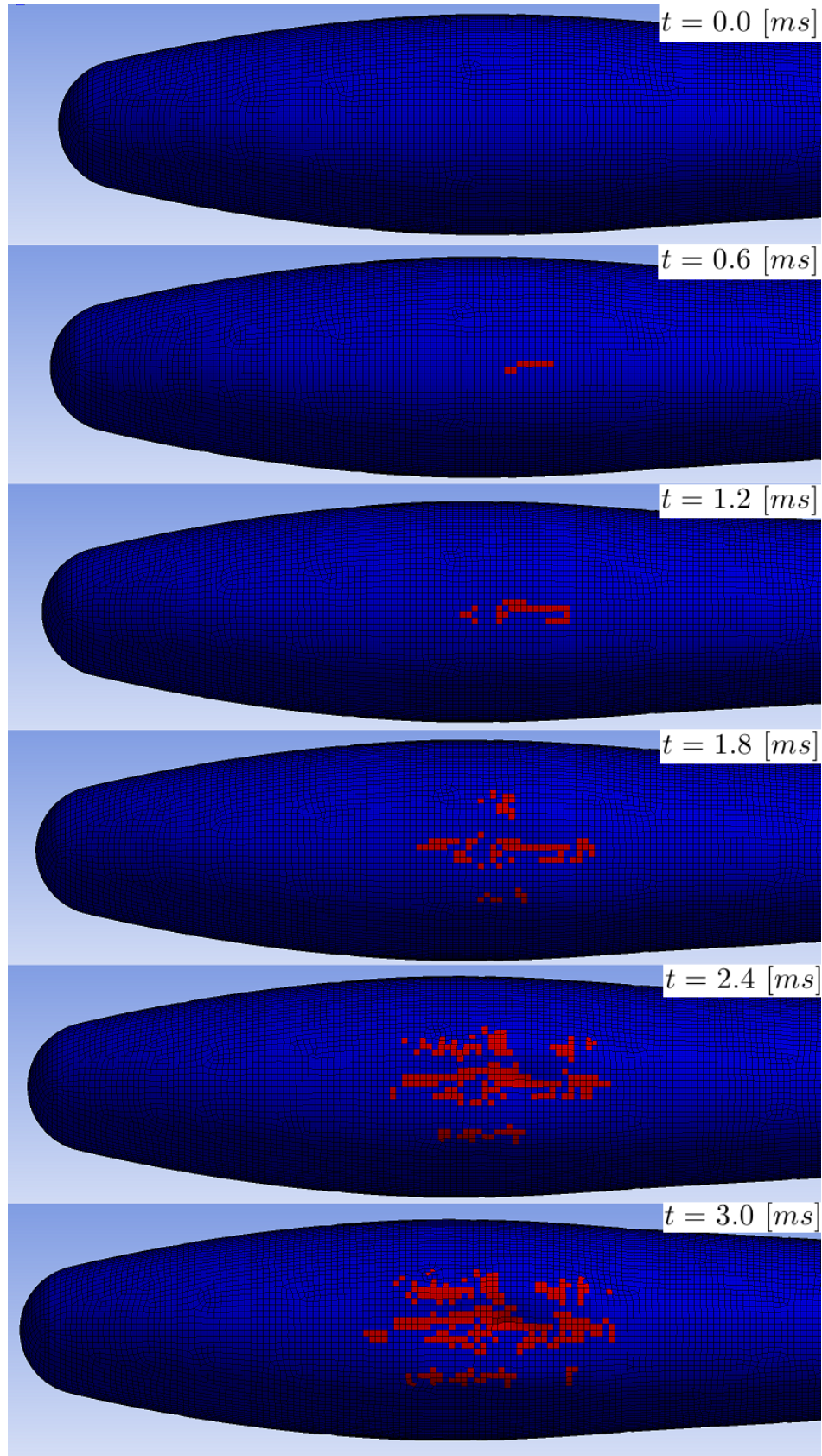


Figure E.6: *Gradual failure for the $[0, 45, -45, 45, 90, 45, -45, 45, 0]$ stacking sequence*

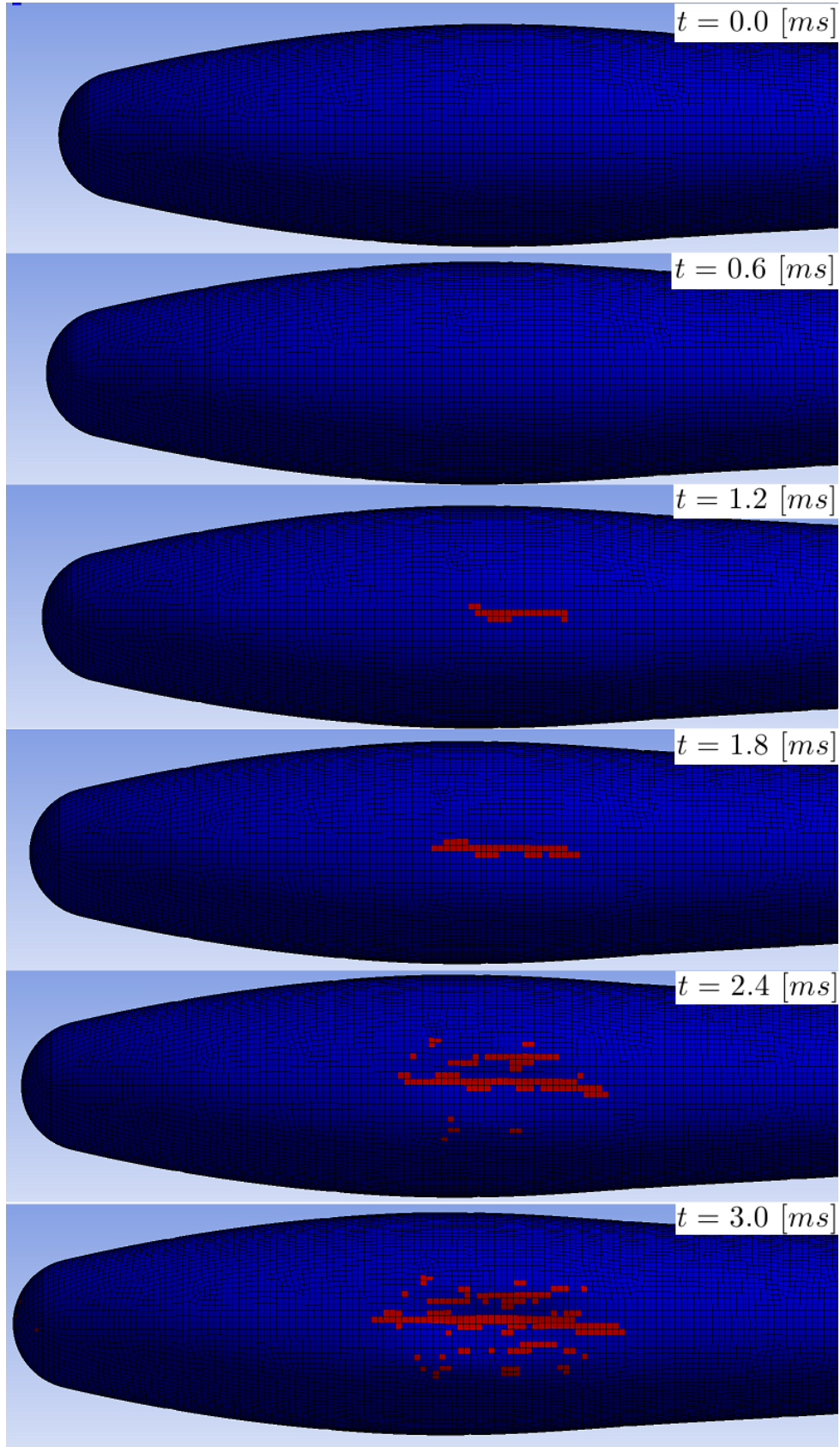


Figure E.7: *Gradual failure for the $[45, -45, 45, -45, 45, -45, 45, -45, 45]$ stacking sequence*

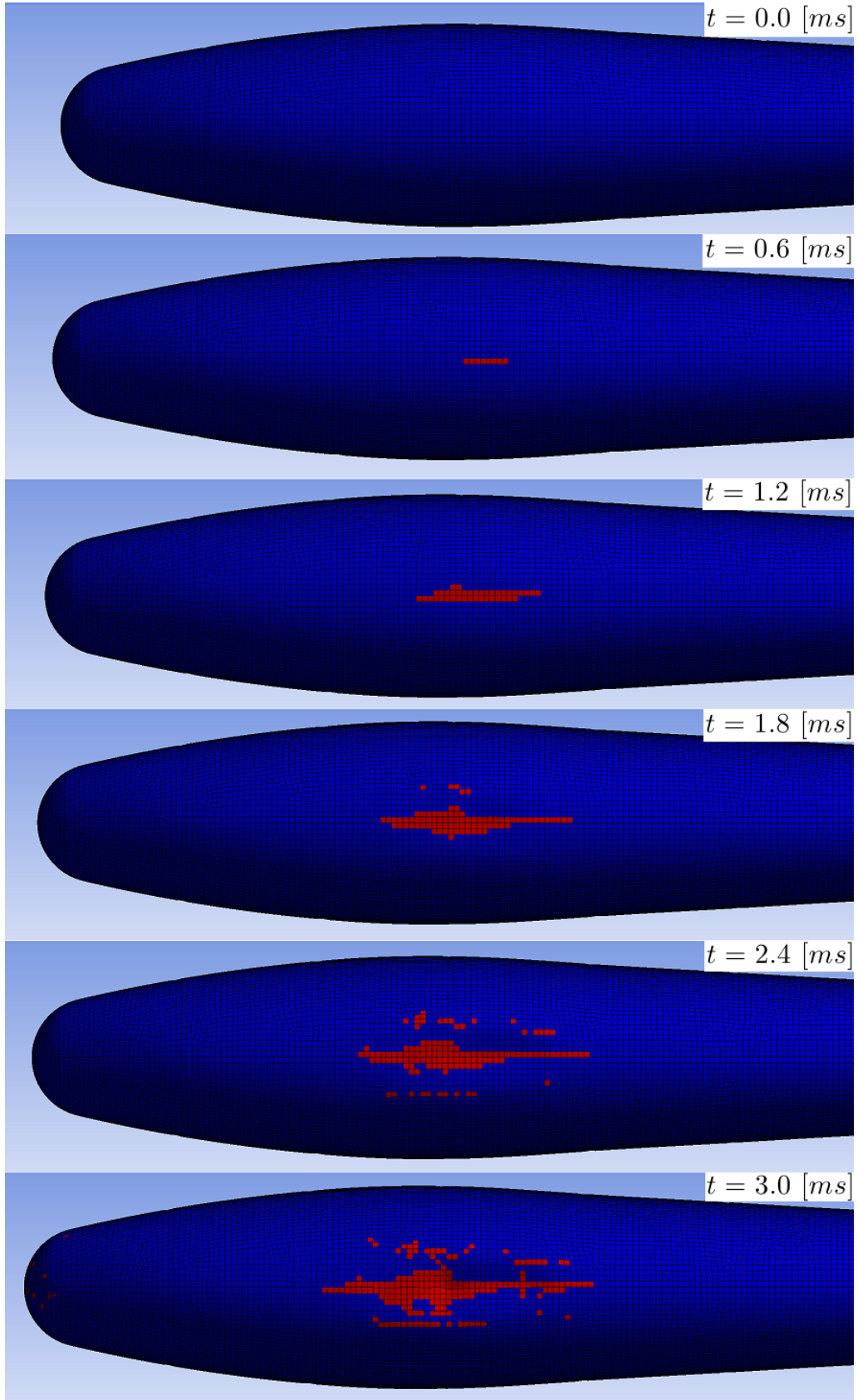


Figure E.8: *Gradual failure for the $[90, 0, 90, 0, 90, 0, 90, 0, 90]$ stacking sequence*

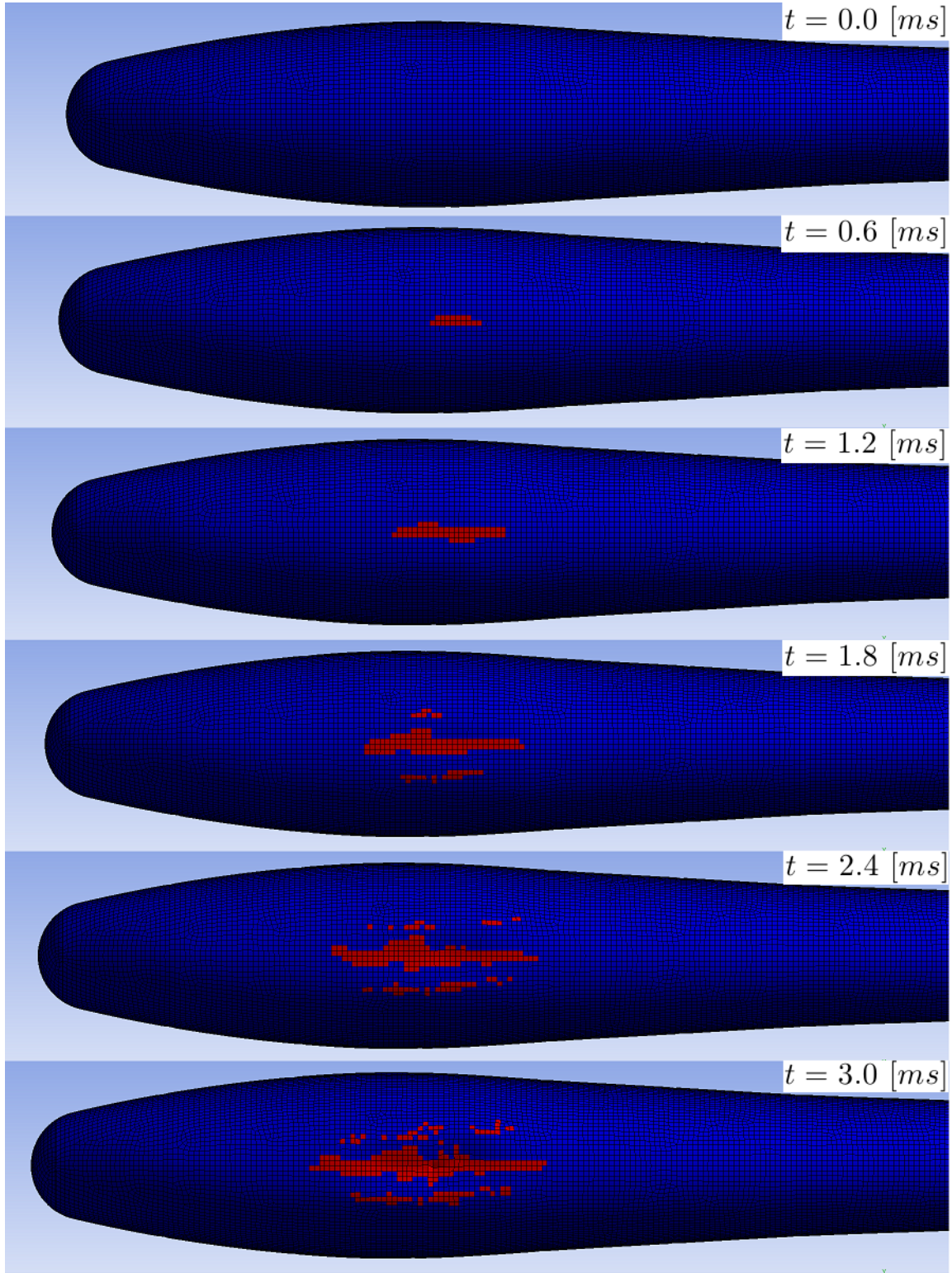


Figure E.9: *Gradual failure for the $[90, 45, -45, 90, 0, 90, -45, 45, 90]$ stacking sequence*

F Pitch (θ) and Descend Velocity Test Results

This appendix contains Figures depicting the failure in all plies at the end of the duration of each analysis. Concept, pitch angle, descend velocity, and time can be taken from the caption of the respective figures

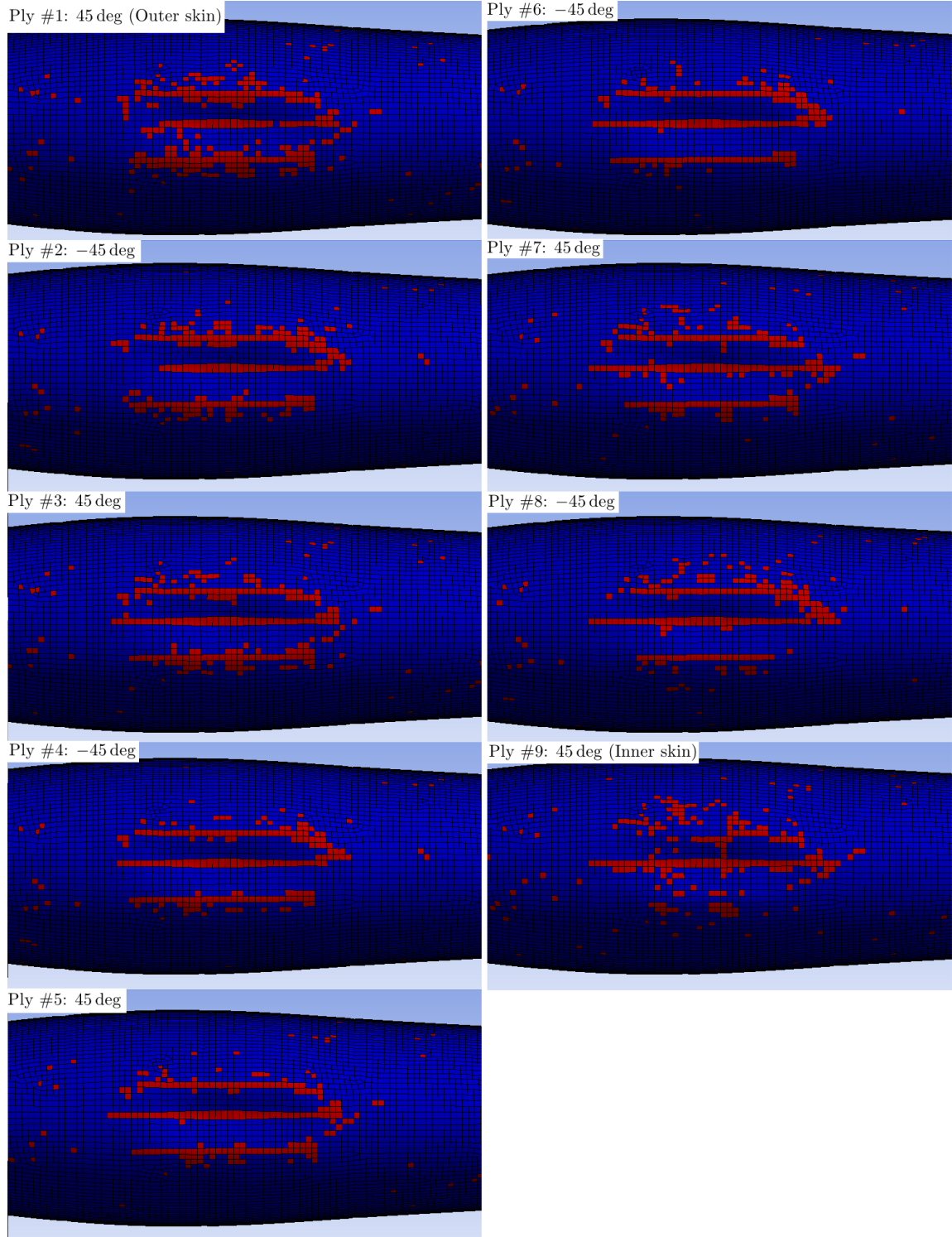


Figure F.1: *Multiframe concept* 0 deg 1 [m/s] $t = 7.5$ [ms]

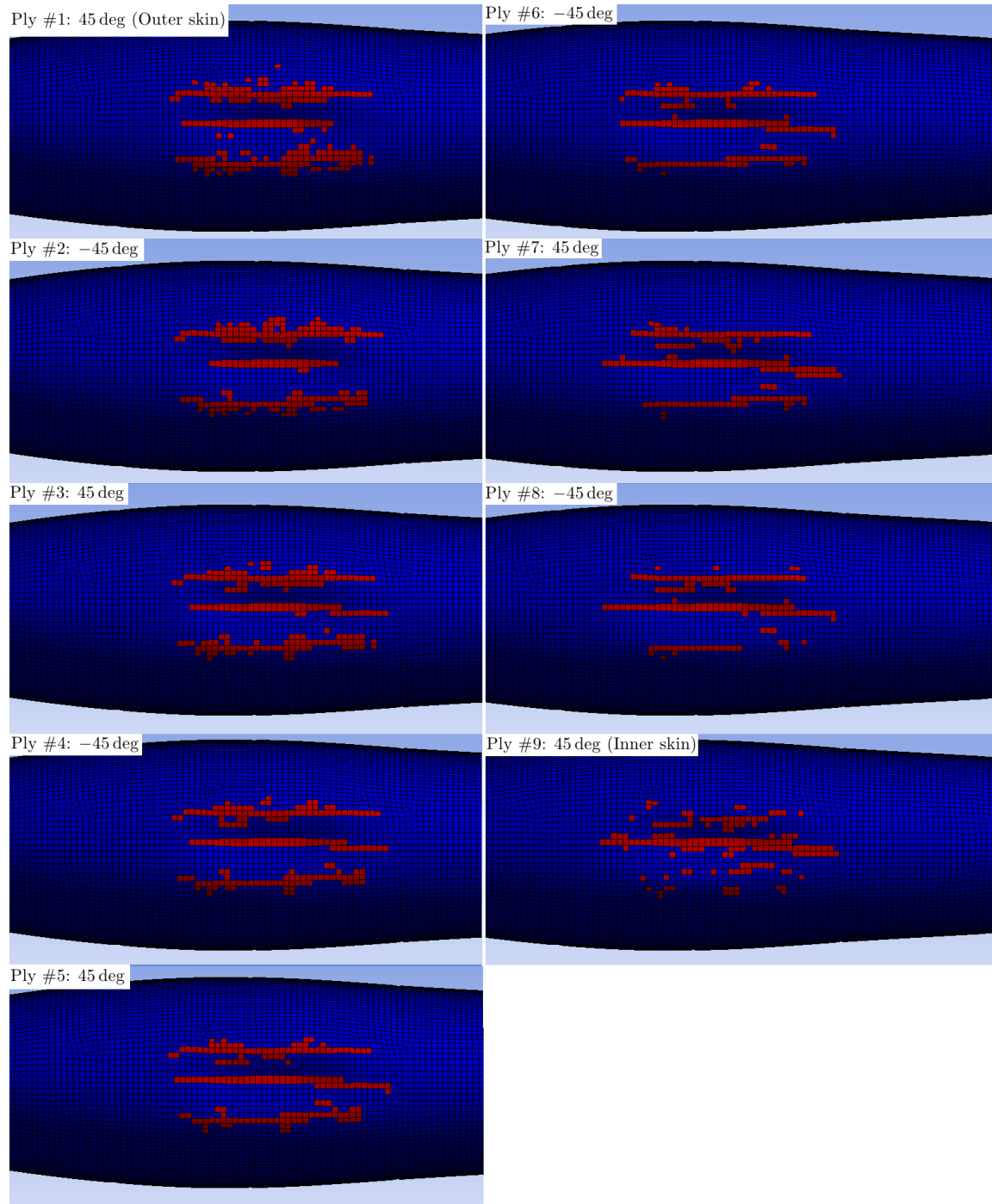


Figure F.2: *Multi-frame concept* 0 deg 2.5 [m/s] $t = 3$ [ms]

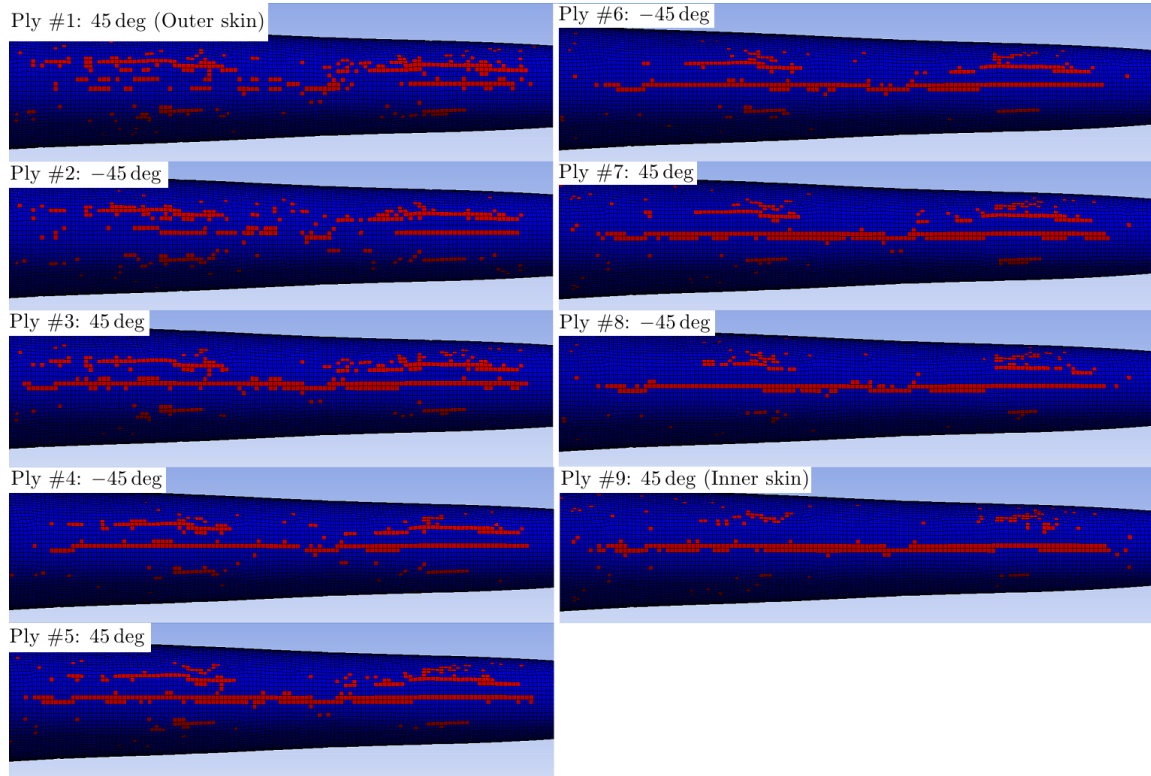


Figure F.3: *Multiframe concept 6 deg 1 [m/s] $t = 7.5$ [ms]*

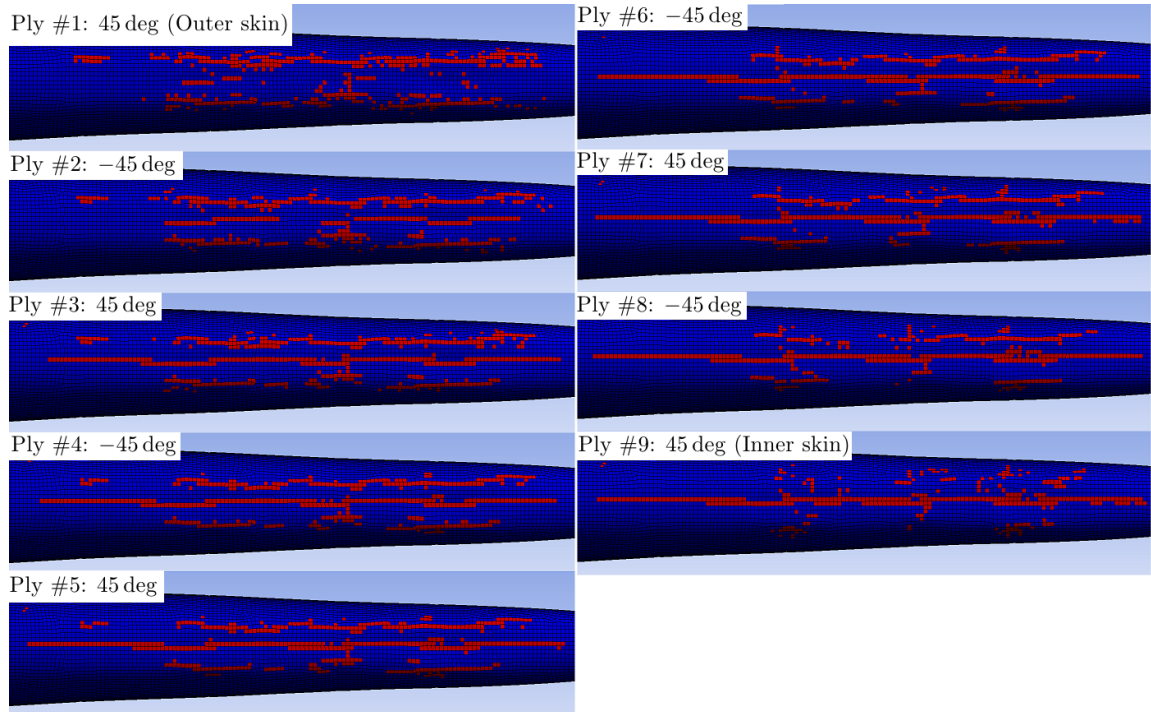


Figure F.4: *Multiframe concept 6 deg 2.5 [m/s] $t = 3$ [ms]*

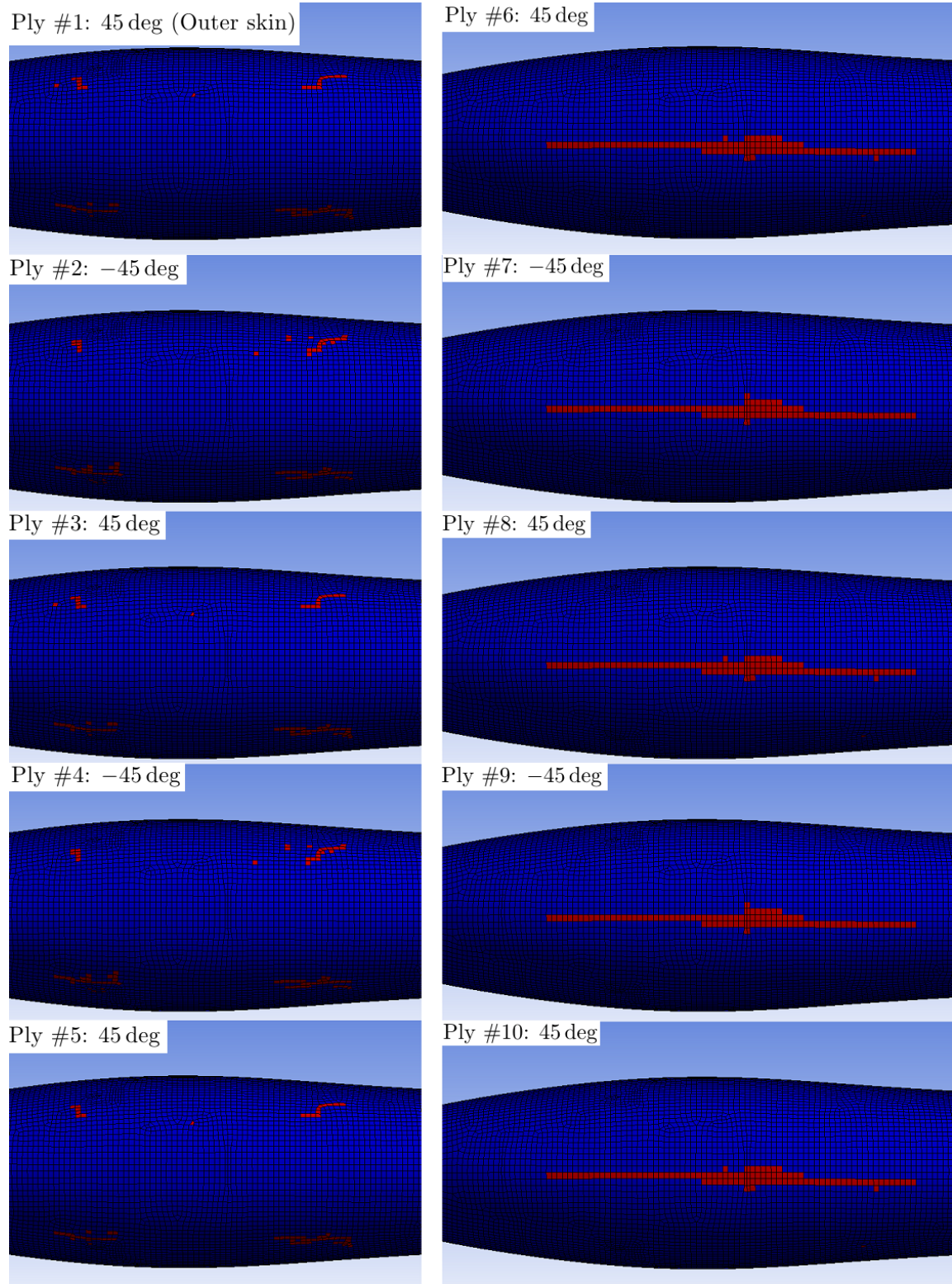


Figure F.5: *Sandwich Skin concept* 0 deg 2.5 [m/s] $t = 5$ [ms]

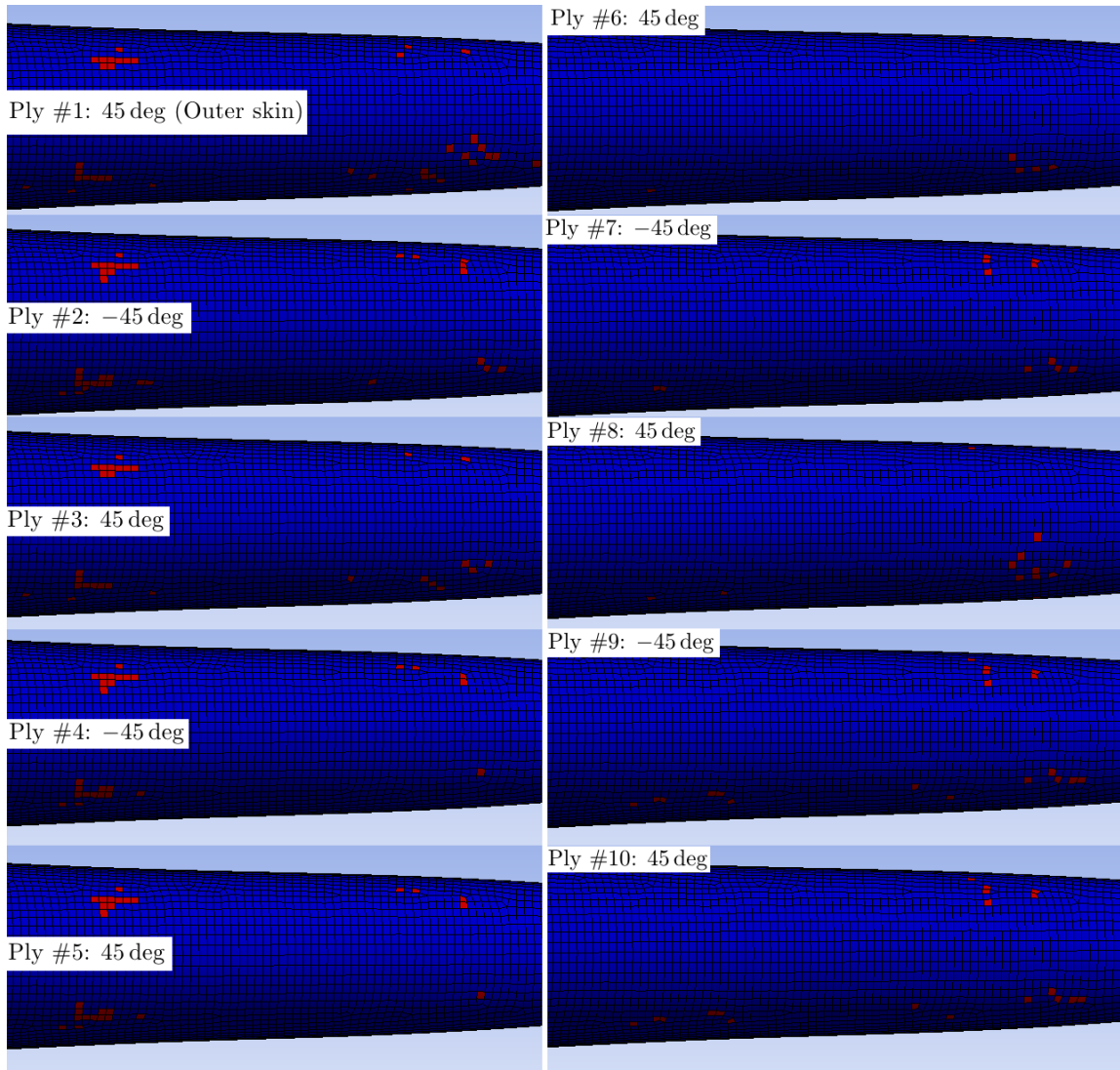


Figure F.6: *Sandwich Skin* concept 6 deg 1 [m/s] $t = 11$ [ms]

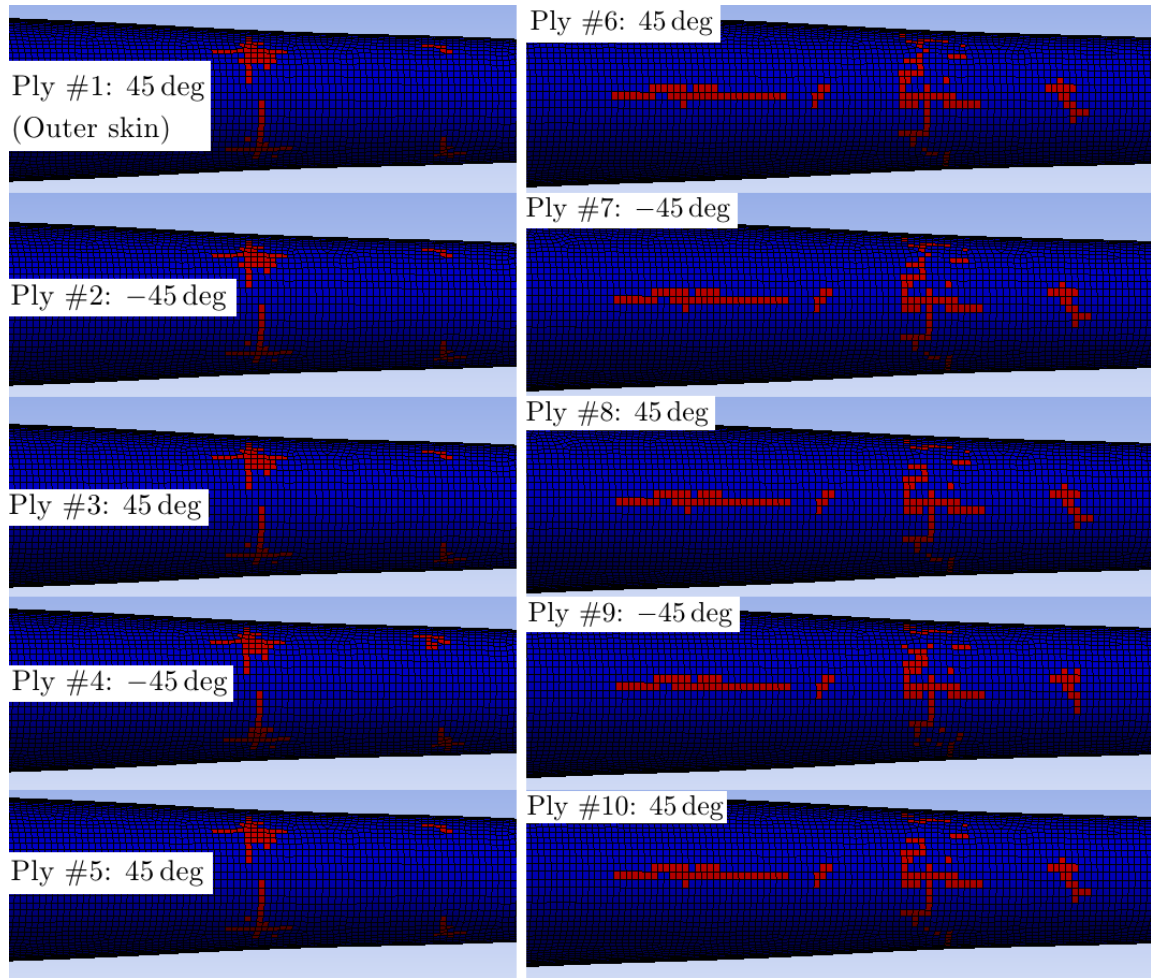


Figure F.7: *Sandwich Skin concept* 6 deg 2.5 [m/s] $t = 4$ [ms]

G Fuselage CAD Figures

This Appendix contains more figures depicting the Multiframe and Sandwich Skin concepts. All figures was created in the Catia V5R20 CAD environment. The skin, aft section, and, for the Multiframe concept, the belly reinforcement have been sliced in two for illustrative purposes. Although the wing surface is included in the figures, the models exported to FEA were limited to the fuselages only. Please note that the belly reinforcement was not included in the FE model, it was included in the CAD models to show possible alterations to the concept.

Multiframe Concept

Figures G.1 through G.4 depicts the Multiframe concept from different viewpoints.

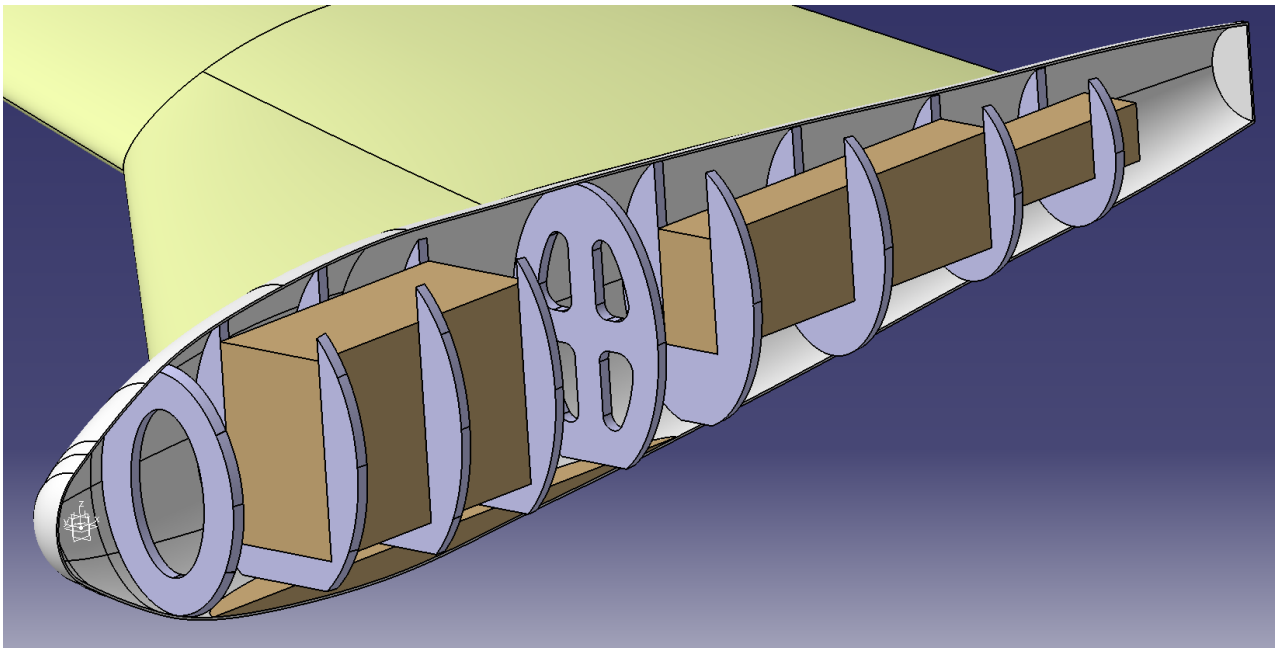


Figure G.1: *Multiframe concept, front 3D view*

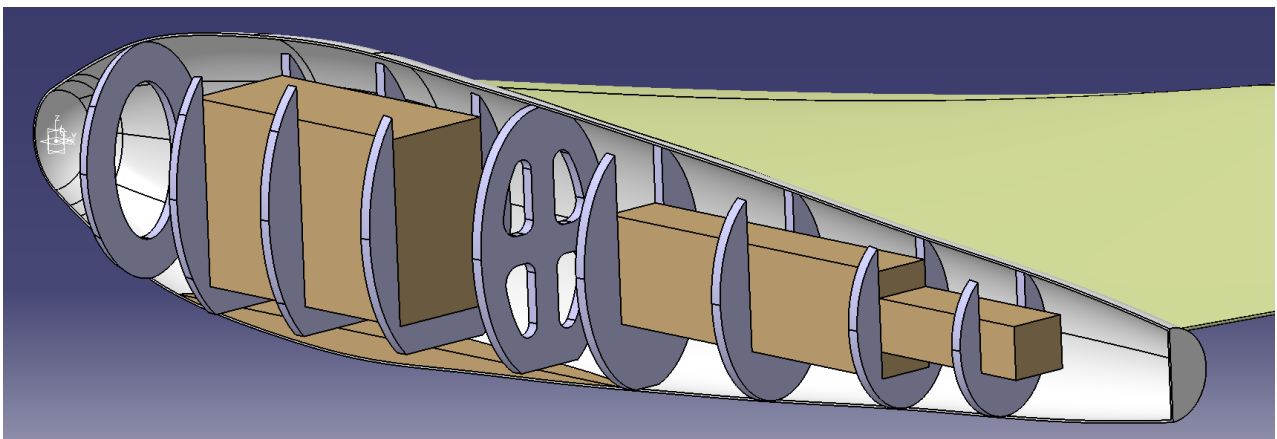


Figure G.2: *Multiframe concept, rear 3D view*

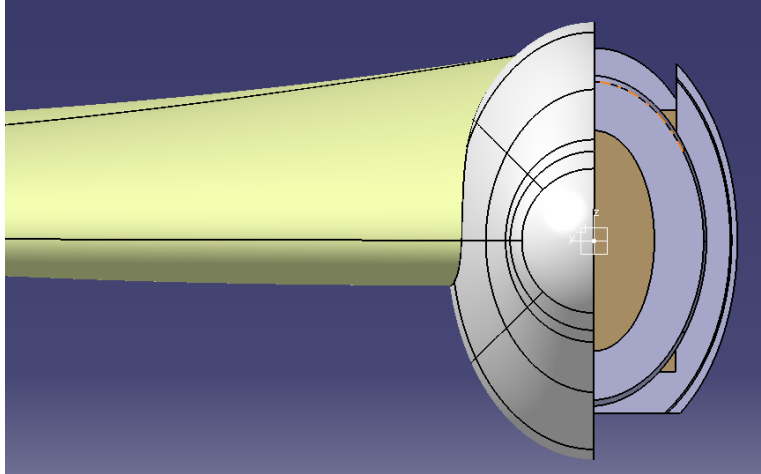


Figure G.3: *Multiframe concept, front view*

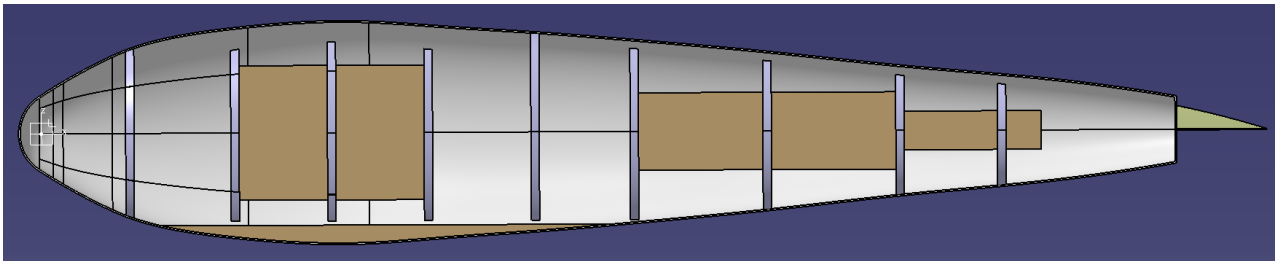


Figure G.4: *Multiframe concept, left view*

Sandwich Skin Concept

Figures G.5 through G.8 depicts the Sandwich Skin concept from different viewpoints.

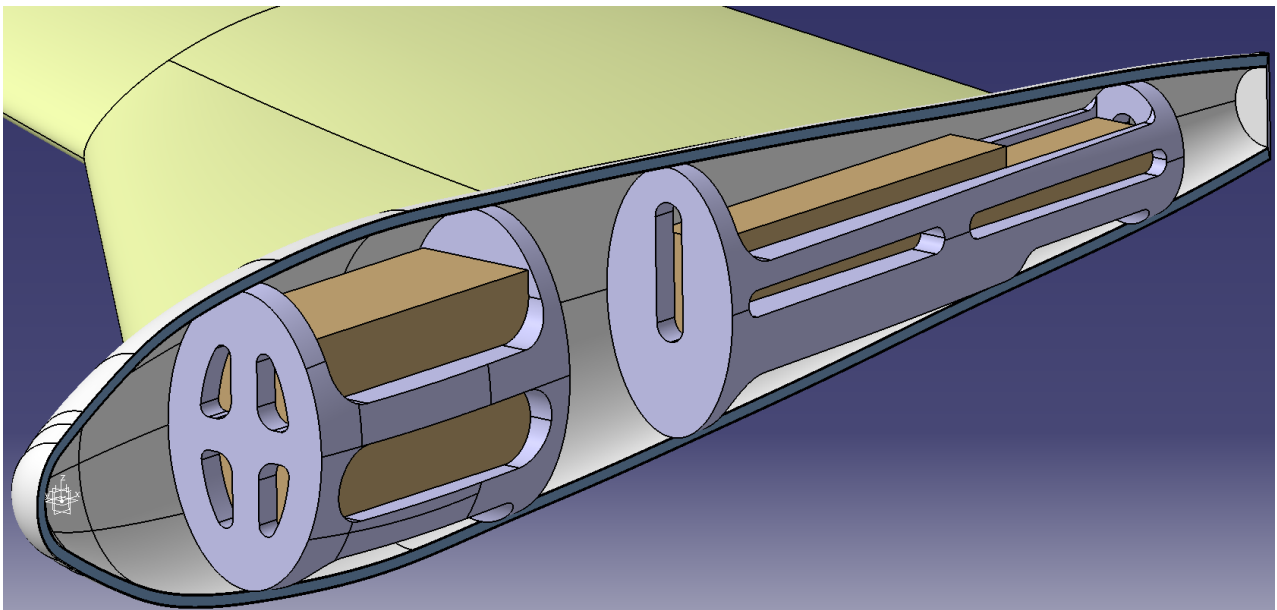


Figure G.5: *Sandwich Skin concept, front 3D view. Blue skin section illustrates the sandwich foam core*

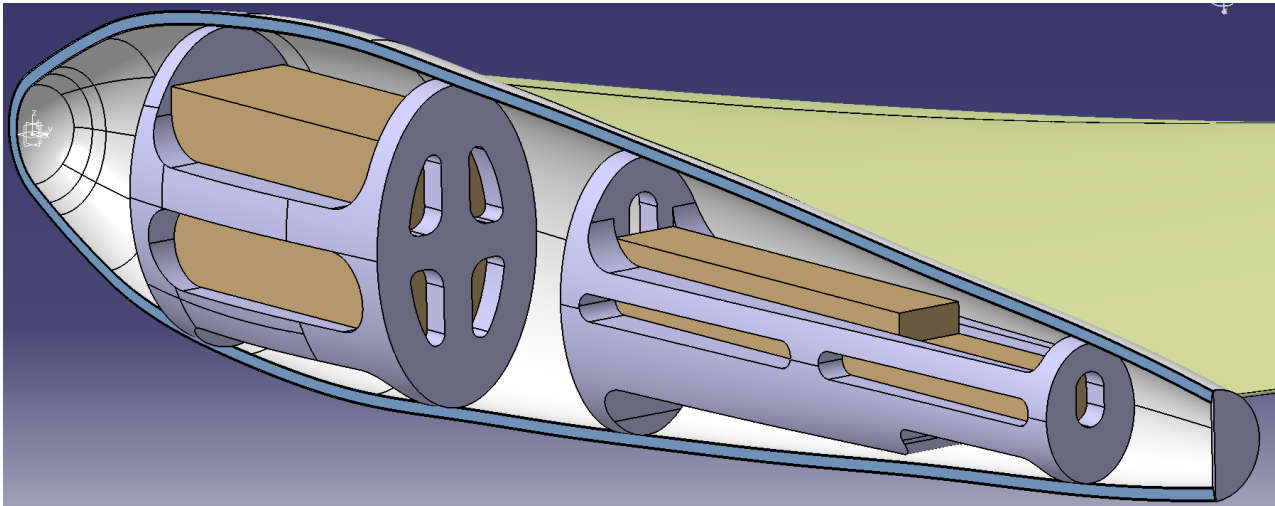


Figure G.6: *Sandwich Skin concept, rear 3D view*

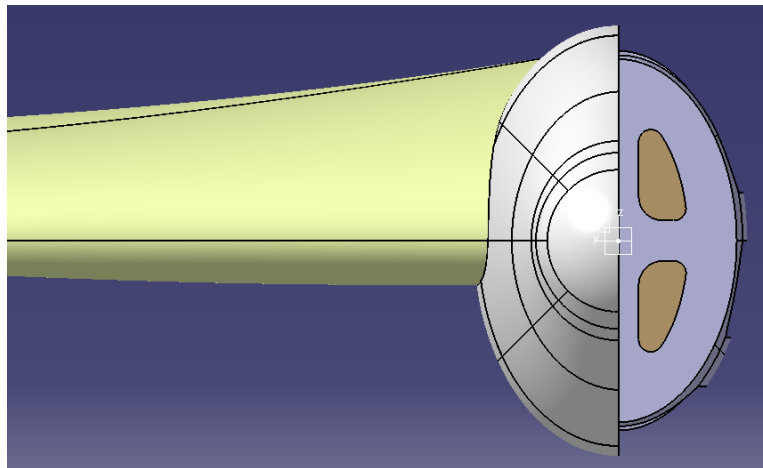


Figure G.7: *Sandwich Skin concept, front view*

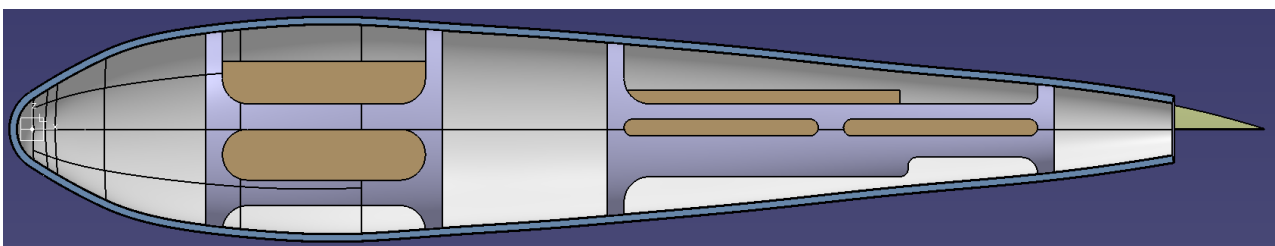


Figure G.8: *Sandwich Skin concept, left view*